Statistically calibrated parametric procedure for lateral-torsional buckling of steel bridge girders: comparison with EN 1993 and finite-element models developed in LUSAS©

Monosymmetric welded I-girders in twin-girder and three-girder composite decks during slab casting

Carlo Sigmund[a,1], Francesco Casaroli[b]

[a] *Civil and environmental engineer*
[b] *Structural engineer*

Abstract

Finite-element modelling of bridge girders using two-dimensional elements can capture both global buckling of the member and local buckling of the web and flange panels. This broad modal response may, however, make it difficult to identify the first critical mode attributable to global lateral-torsional buckling, because the lowest eigenvalues may correspond to local cross-sectional deformations. In this context, a preliminary and independent estimate of the order of magnitude of the global lateral-torsional resistance provides a useful reference for classifying the eigenmodes and interpreting the numerical results.
This paper therefore proposes a simplified, conservative parametric procedure for the preliminary assessment of lateral-torsional buckling in steel I-section bridge girders, with particular reference to monosymmetric welded girders used in twin-girder and three-girder steel–concrete composite decks during slab casting. During this stage, the slab does not yet act compositely and the steel girder must be checked under permanent and construction actions, accounting for the unrestrained length against lateral-torsional buckling, the load application level and cross-sectional monosymmetry.
The proposed formulation is calibrated against the complete EN 1993 procedure, based on the determination of the elastic critical moment M_{cr}, the lateral-torsional slenderness, the reduction factor χ_{LT} and the design buckling resistance moment $M_{b,Rd}$. The calibration is derived from a statistical parametric study of welded bridge-girder sections covering both usual and boundary geometric domains. It also includes Class 4 sections evaluated using effective properties, configurations with longitudinal stiffeners, Saint-Venant torsional and warping stiffnesses, and the position of the load relative to the shear centre.
The procedure does not replace a full code-based verification or advanced numerical modelling. Rather, it provides a rapid tool for preliminary design and checking, enabling the expected level of global lateral-torsional resistance to be estimated, potentially critical configurations to be identified, and local buckling modes to be distinguished from global ones. The paper also compares the EN 1993 formulation, linear elastic eigenvalue analyses performed with LTBeamN© and finite-element models developed in LUSAS©. These are treated as complementary tools for interpreting differences between the code-based approach, the global elastic model and the detailed numerical representation.

Keywords: Lateral-torsional buckling, steel girders, I-sections, elastic critical moment, Eurocode 3, simplified formulae, LTBeamN, LUSAS, GPI Ingegneria

Introduction

The lateral-torsional stability of steel bridge girders is particularly important during temporary construction stages, when the concrete slab has not yet developed composite stiffness and the steel girder behaves as an open-section member that is generally not continuously laterally restrained. In this configuration, the compression flange may not be adequately restrained out of plane, and the verification must account for the unrestrained length between torsional restraints, the bending-moment distribution, the load application level and cross-sectional monosymmetry.

This paper proposes an operational framework for the preliminary sizing and verification of welded steel I-section bridge girders, with particular reference to twin-girder and three-girder steel–concrete composite decks during slab casting. The formulation does not re-

Email addresses: sigmund@gpingegneria.com (Carlo Sigmund), casaroli@gpingegneria.com (Francesco Casaroli)
[1] https://orcid.org/0000-0002-4925-3469

place a full code-based verification, but aims to establish a concise relationship between compression-flange geometry, the unrestrained length against lateral-torsional buckling and the lateral-torsional resistance evaluated through the Eurocode 3 verification sequence.

The elastic critical moment for lateral-torsional buckling, denoted by M_{cr}, and the EC3 design resistance to lateral-torsional buckling, denoted by $M_{b,Rd}$, are explicitly distinguished throughout. This distinction is essential: the elastic critical moment is an elastic stability quantity, whereas the design verification requires the evaluation of the lateral-torsional slenderness, the reduction factor χ_{LT} and the partial resistance factor γ_{M1}.[2]

1. Derivation of the elastic critical moment for lateral-torsional buckling

Consider a prismatic steel beam with a thin-walled open cross-section, subjected to major-axis bending. The derivation is developed within the linear elastic theory of thin-walled members, assuming small displacements, small rotations, a homogeneous, isotropic material, no initial imperfections and a cross-section that remains undeformed in its own plane. Let s be the longitudinal coordinate of the beam, with:

$$0 \le s \le L$$

Let y and z be the principal centroidal axes of the cross-section, with y the major axis and z the minor axis. The primary bending occurs about the y-axis, while lateral-torsional buckling involves the lateral displacement associated with the stiffness EI_z and the torsional rotation of the cross-section. The kinematic functions are introduced as:

$$u = u(s)$$

$$\varphi = \varphi(s)$$

where $u(s)$ is the lateral displacement of the shear centre and $\varphi(s)$ is the torsional rotation of the cross-section about the longitudinal axis of the beam. The elastic cross-sectional properties involved in the problem are:

- I_z, second moment of area about the minor axis $[L^4]$;
- I_y, second moment of area about the major axis $[L^4]$;
- I_t, Saint-Venant torsion constant $[L^4]$;
- I_w, warping constant $[L^6]$;
- E, Young's modulus $[F/L^2]$;
- G, shear modulus $[F/L^2]$.

The quantity sought is the critical value of the bending moment, denoted by M_{cr}, at which the straight configuration loses stability and a non-trivial deformed configuration becomes possible:

$$u(s) \not\equiv 0, \qquad \varphi(s) \not\equiv 0$$

The problem is therefore an eigenvalue problem in which the eigenvalue is the critical bending moment.

1.1. Coupled elastic equations

For thin-walled open sections, the internal torque is the sum of the Saint-Venant uniform-torsion contribution and the non-uniform torsion contribution associated with warping. Hence:

$$M_t = GI_t \frac{\mathrm{d}\varphi}{\mathrm{d}s} - EI_w \frac{\mathrm{d}^3\varphi}{\mathrm{d}s^3}$$

The first term:

$$GI_t \frac{\mathrm{d}\varphi}{\mathrm{d}s}$$

represents Saint-Venant uniform torsion, whereas the second term:

$$-EI_w \frac{\mathrm{d}^3\varphi}{\mathrm{d}s^3}$$

represents the contribution due to non-uniform warping of the cross-section. The torsional rotation $\varphi(s)$ changes the local orientation of the cross-section and projects the primary bending moment onto the minor axis. Under small-displacement and small-rotation conditions, the destabilising component is proportional to the product of the bending moment and the torsional rotation. The lateral-bending equilibrium can be written as follows (first-order treatment with $\tan\varphi \approx \sin\varphi \approx \varphi$):

$$EI_z \frac{\mathrm{d}^2u}{\mathrm{d}s^2} + M(s)\varphi = 0$$

Torsional equilibrium in the perturbed configuration must also account for the contribution of lateral curvature to torsion. Linearisation gives:

$$EI_w \frac{\mathrm{d}^4\varphi}{\mathrm{d}s^4} - GI_t \frac{\mathrm{d}^2\varphi}{\mathrm{d}s^2} + M(s)\frac{\mathrm{d}^2u}{\mathrm{d}s^2} + \mathcal{G}_{z_g,z_j}[\varphi] = 0$$

The term $\mathcal{G}_{z_g,z_j}[\varphi]$ represents the geometric contribution associated with the load application level relative to the shear centre and with cross-sectional monosymmetry. It vanishes in the elementary case of a doubly symmetric section loaded through the shear centre.

1.2. Fundamental case with uniform moment and load applied at the shear centre

In the fundamental case, $M(s) = M$ is assumed and initially $\mathcal{G}_{z_g,z_j}[\varphi] = 0$. The lateral-bending equilibrium gives:

$$\frac{\mathrm{d}^2u}{\mathrm{d}s^2} = -\frac{M}{EI_z}\varphi$$

[2]This paper adopts $\gamma_{M1} = 1.10$ for the stability verification of steel bridge members, in accordance with the value recommended by UNI EN 1993-2:2007, *Eurocode 3 – Design of steel structures – Part 2: Steel bridges*, Section 6.1, for member resistance to buckling, unless otherwise specified by the applicable National Annex.

Substitution of this relation into the torsional equilibrium yields a single differential equation in $\varphi(s)$:

$$EI_w \frac{\mathrm{d}^4\varphi}{\mathrm{d}s^4} - GI_t \frac{\mathrm{d}^2\varphi}{\mathrm{d}s^2} - \frac{M^2}{EI_z}\varphi = 0$$

For fork supports at the ends, the first critical mode may be assumed as:

$$\varphi(s) = \varphi_0 \sin\left(\frac{\pi s}{L}\right)$$

Hence:

$$\frac{\mathrm{d}^2\varphi}{\mathrm{d}s^2} = -\left(\frac{\pi}{L}\right)^2 \varphi$$

$$\frac{\mathrm{d}^4\varphi}{\mathrm{d}s^4} = \left(\frac{\pi}{L}\right)^4 \varphi$$

Substitution into the preceding differential equation gives:

$$EI_w \left(\frac{\pi}{L}\right)^4 \varphi + GI_t \left(\frac{\pi}{L}\right)^2 \varphi - \frac{M^2}{EI_z}\varphi = 0$$

Since a non-trivial solution is sought, it must satisfy:

$$\varphi \neq 0$$

Therefore:

$$\frac{M^2}{EI_z} = EI_w \left(\frac{\pi}{L}\right)^4 + GI_t \left(\frac{\pi}{L}\right)^2$$

Multiplying by EI_z gives:

$$M^2 = EI_z \left[EI_w \left(\frac{\pi}{L}\right)^4 + GI_t \left(\frac{\pi}{L}\right)^2\right]$$

The elastic critical moment in the fundamental case is therefore:

$$M_{cr} = \frac{\pi}{L}\sqrt{EI_z GI_t + \frac{\pi^2 E^2 I_z I_w}{L^2}}$$

The same relationship may be rewritten as:

$$M_{cr} = \frac{\pi^2 EI_z}{L^2}\left[\frac{I_w}{I_z} + \frac{L^2 GI_t}{\pi^2 EI_z}\right]^{1/2}$$

This expression is the elastic core of lateral-torsional buckling theory for open-section beams: the first term under the square root represents the warping contribution, while the second represents the contribution from uniform torsion.

1.3. Introduction of effective lengths

In practical applications, the end-restraint conditions may differ from ideal fork supports. Two effective-length factors are therefore introduced:

- k, associated with the lateral buckling mode;
- k_w, associated with warping restraint at the member ends.

The effective lateral length is taken as:

$$L_b = kL$$

By contrast, the warping contribution is adjusted through the ratio:

$$\left(\frac{k}{k_w}\right)^2$$

The fundamental elastic expression therefore becomes:

$$M_{cr} = \frac{\pi^2 EI_z}{(kL)^2}\left[\left(\frac{k}{k_w}\right)^2 \frac{I_w}{I_z} + \frac{(kL)^2 GI_t}{\pi^2 EI_z}\right]^{1/2}$$

This relationship still refers to a load applied through the shear centre and to a section unaffected by monosymmetry.

1.4. Effect of load application level and monosymmetry

When the transverse load is not applied through the shear centre, its line of action introduces an additional geometric term. Define (Fig. 1):

$$z_g = z_a - z_s$$

the distance between the load application point and the shear centre, where z_a is the coordinate of the load application point and z_s is the coordinate of the shear centre. For monosymmetric sections, the asymmetric distribution of the cross-sectional properties introduces a further geometric term, denoted by z_j, associated with coupling between lateral bending and torsion. This quantity must be evaluated using the same sign convention adopted for z_g and for the parameter $\Delta = C_2 z_g - C_3 z_j$. In accordance with the convention used for the elastic critical moment, the z-axis is taken as positive towards the compression flange at the section of maximum moment (see Fig. 1). The monosymmetry parameter is defined generally as:

$$z_j = z_s - \frac{1}{2I_y}\int_A z\left(y^2 + z^2\right)\,\mathrm{d}A$$

where z_s is the coordinate of the shear centre relative to the cross-sectional centroid, evaluated using the sign convention shown in Fig. 1, and the integral extends over the entire cross-sectional area. For a doubly symmetric section, the shear centre coincides with the centroid and the integral contribution vanishes by symmetry; therefore:

$$z_j = 0.$$

For welded I-sections, neglecting the web contribution to the integral and concentrating the dominant contribution at the centroids of the two flanges leads to the approximate expression:

$$z_j \simeq z_s - \frac{1}{2I_y}\left(z_{f,\mathrm{sup}} I_{y,\mathrm{sup}} + z_{f,\mathrm{inf}} I_{y,\mathrm{inf}}\right),$$

where $z_{f,\mathrm{sup}}$ and $z_{f,\mathrm{inf}}$ are the signed coordinates of the centroids of the two flanges relative to the cross-sectional centroid, while $I_{y,\mathrm{sup}}$ and $I_{y,\mathrm{inf}}$ are the contributions of the respective flanges to the global second moment of area about the centroidal y–y axis of the complete section ($I_{y,f} = I_{y,f}^{(c)} + A_f z_f^2$):

$$I_{y,\mathrm{sup}} = \frac{b_{\mathrm{sup}} t_{\mathrm{sup}}^3}{12} + A_{\mathrm{sup}} z_{f,\mathrm{sup}}^2,$$
$$I_{y,\mathrm{inf}} = \frac{b_{\mathrm{inf}} t_{\mathrm{inf}}^3}{12} + A_{\mathrm{inf}} z_{f,\mathrm{inf}}^2.$$

where $I_{y,f}^{(c)}$ is the second moment of area of the individual flange about its own centroidal axis parallel to y–y. Therefore, $I_{y,\mathrm{sup}}$ and $I_{y,\mathrm{inf}}$ are not merely the centroidal second moments of area of the flanges, because they also include the corresponding parallel-axis terms. In this approximate expression, the coordinates $z_{f,\mathrm{sup}}$ and $z_{f,\mathrm{inf}}$ must likewise be defined with the z-axis positive towards the compression flange.

An alternative practical expression relates the monosymmetry parameter to the distance between the flange centroids and to the flange-distribution coefficient:

$$\beta_f = \frac{I_{z,\mathrm{sup}}}{I_{z,\mathrm{sup}} + I_{z,\mathrm{inf}}},$$

where $I_{z,\mathrm{sup}}$ and $I_{z,\mathrm{inf}}$ are the second moments of area of the upper and lower flanges alone about the minor z-axis. For a monosymmetric section, their parallel-axis terms vanish ($e_{y,f} = 0$):

$$I_{z,\mathrm{sup}} = \frac{t_{\mathrm{sup}}\, b_{\mathrm{sup}}^3}{12}, \quad I_{z,\mathrm{inf}} = \frac{t_{\mathrm{inf}}\, b_{\mathrm{inf}}^3}{12}.$$

Defining:

$$h_f = h - \frac{t_{f,\mathrm{sup}} + t_{f,\mathrm{inf}}}{2}$$

as the distance between the centroids of the two flanges, the following operational estimates may be used:

$$z_j \simeq 0.41\, h_f\,(2\beta_f - 1) \qquad ext for \beta_f > 0.5,$$

$$z_j \simeq 0.55\, h_f\,(2\beta_f - 1) \qquad ext for \beta_f < 0.5.$$

These relationships are intended solely as preliminary estimates and are not used in the computational engine developed in this study. Only the convention shown on the left-hand side of Fig. 1 is adopted hereafter: the z-axis is positive towards the upper compression flange and the parameter is calculated by integrating over the entire cross-section, $z_j = z_s - J_{\mathrm{int}}/(2I_y)$. Under this convention, a negative value of z_j increases $\Delta = C_2 z_g - C_3 z_j$ and produces a destabilising contribution, whereas a positive value reduces it.

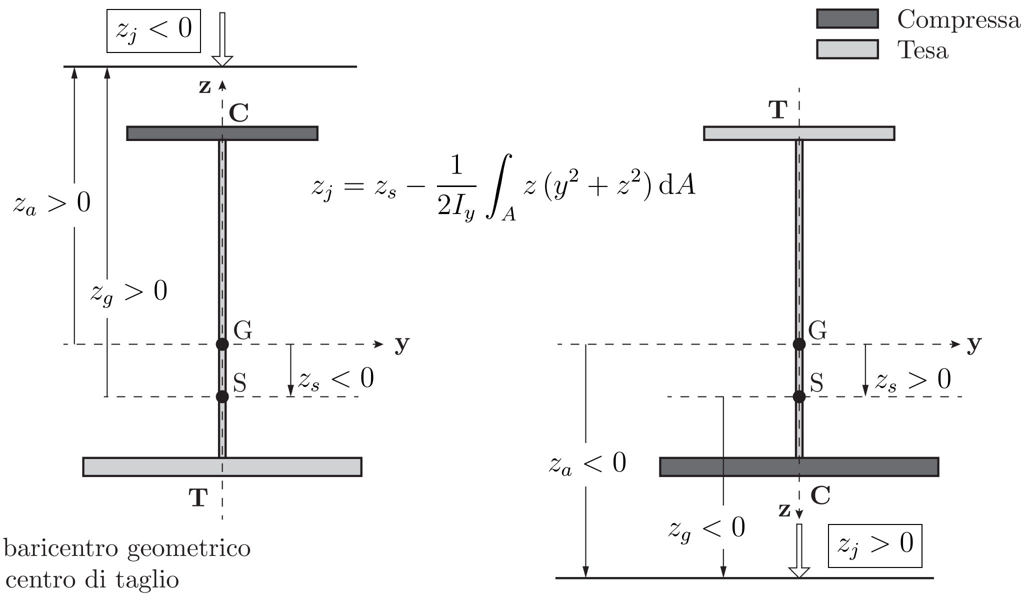

Figure 1. *Sign conventions for z_s (coordinate of the shear centre relative to the geometric centroid G), z_a (coordinate of the load application point relative to G) and $z_g = z_a - z_s$. Only the convention shown on the left is adopted in this paper: the local z-axis is positive towards the upper compression flange; the same orientation is used in the integral defining z_j. Figure adapted from [25]*

A compact formulation often used for monosymmetric I-sections is:

$$z_j \simeq 0.90\, h_s\,(2\beta_f - 1)\left(1 - \frac{I_z}{I_y}\right),$$

where h_s is the distance between the flange centroids. For slender I-girders, for which generally $I_z \ll I_y$, the term $(1 - I_z/I_y)$ is close to unity. Using the approximate relationship between shear-centre position and flange-inertia distribution, the same estimate can also be expressed as:

$$z_j \simeq 0.90\, z_s\left(\frac{1}{\beta_f}\right)\left(1 - \frac{I_z}{I_y}\right).$$

The preceding relationships are operational approximations and may be used only provided that consistency is maintained among the definition of β_f, the direction of the z-axis, the location of the compression flange and the convention adopted in evaluating z_g and Δ. The effects of load application level and monosymmetry are combined in the parameter:

$$\Delta = C_2 z_g - C_3 z_j$$

where C_2 and C_3 are coefficients that depend on the load distribution, the bending-moment diagram and the restraint conditions. The parameter Δ has dimensions of length. Positive values of Δ reduce the elastic critical moment because the term is subtracted in the final solution, whereas negative values have a stabilising effect.

1.5. Dimensionless form of the eigenvalue problem

The following auxiliary quantity is introduced:

$$\mu = \frac{M_{cr}}{\frac{\pi^2 E I_z}{(kL)^2}}$$

The following two parameters are also defined:

$$A = \left(\frac{k}{k_w}\right)^2 \frac{I_w}{I_z} + \frac{(kL)^2 G I_t}{\pi^2 E I_z}$$

$$\Delta = C_2 z_g - C_3 z_j$$

The parameter A collects the elastic contributions from warping and uniform torsion, while Δ collects the geometric effects associated with the load application level relative to the shear centre and with cross-sectional monosymmetry. Before introducing the coefficient C_1, the characteristic equation of the eigenvalue problem may be written in quadratic form:

$$\mu^2 + 2\Delta\mu - A = 0$$

The quadratic structure of the equation arises because the critical bending moment enters the problem both through lateral-bending–torsion coupling, which generates the quadratic eigenvalue term, and through the geometric contribution associated with z_g and z_j, which generates the linear term. The solutions of the characteristic equation are:

$$\mu = -\Delta \pm \sqrt{\Delta^2 + A}$$

The physically meaningful solution is the positive one:

$$\mu = \sqrt{A + \Delta^2} - \Delta$$

Returning to the dimensional quantity M_{cr} gives:

$$M_{cr} = \frac{\pi^2 E I_z}{(kL)^2} \left[\sqrt{A + \Delta^2} - \Delta\right]$$

Substitution of the explicit definitions of A and Δ into the preceding relationship gives:

$$M_{cr} = \frac{\pi^2 E I_z}{(kL)^2} \left[\left(\left(\frac{k}{k_w}\right)^2 \frac{I_w}{I_z} + \frac{(kL)^2 G I_t}{\pi^2 E I_z} + (C_2 z_g - C_3 z_j)^2\right)^{1/2} - (C_2 z_g - C_3 z_j)\right]$$

Note on the influence of the sign of Δ on M_{cr}

Returning to the dimensional quantity M_{cr} gives:

$$M_{cr} = \frac{\pi^2 E I_z}{(kL)^2} \left[\sqrt{A + \Delta^2} - \Delta\right].$$

Assuming $A > 0$ and keeping E, I_z, k and L constant, the dependence of the elastic critical moment on the parameter Δ can be examined from the sign of the partial derivative:

$$\frac{\partial M_{cr}}{\partial \Delta} = \frac{\pi^2 E I_z}{(kL)^2} \left(\frac{\Delta}{\sqrt{A + \Delta^2}} - 1\right).$$

Rationalising the expression in parentheses, the derivative may be rewritten as:

$$\frac{\partial M_{cr}}{\partial \Delta} = -\frac{\pi^2 E I_z}{(kL)^2} \frac{A}{\sqrt{A + \Delta^2}\left(\sqrt{A + \Delta^2} + \Delta\right)}.$$

Since, for $A > 0$,

$$\sqrt{A + \Delta^2} > |\Delta|,$$

all terms in the denominator are positive and therefore

$$\boxed{\frac{\partial M_{cr}}{\partial \Delta} < 0}.$$

The elastic critical moment M_{cr} is therefore a strictly decreasing function of Δ: an increase in Δ reduces M_{cr}, whereas a decrease in Δ increases M_{cr}. This conclusion remains valid for negative values of Δ, provided that $A > 0$.

1.6. Introduction of the moment-distribution coefficient

The preceding expressions were derived assuming a fundamental bending-moment distribution along the beam. In the general case, the actual moment distribution changes the critical eigenvalue. This effect is represented by the coefficient C_1, which depends on the bending-moment diagram and the restraint conditions. Hence:

$$M_{cr} = C_1 \frac{\pi^2 E I_z}{(kL)^2} \left[\sqrt{A + \Delta^2} - \Delta\right]$$

In fully expanded form:

$$M_{cr} = C_1 \frac{\pi^2 E I_z}{(kL)^2} \left[\left(\left(\frac{k}{k_w}\right)^2 \frac{I_w}{I_z} + \frac{(kL)^2 G I_t}{\pi^2 E I_z} + (C_2 z_g - C_3 z_j)^2\right)^{1/2} - (C_2 z_g - C_3 z_j)\right]$$

For sections for which the approximation $I_y \gg I_z$ is not valid, the general formulation introduces the factor:

$$g := \sqrt{1 - \frac{I_z}{I_y}}$$

For slender I-sections, or more generally for beams satisfying $I_y \gg I_z$, one has:

$$g \simeq 1$$

The general expression may therefore be written in compact form:

$$M_{cr} = C_1 \frac{\pi^2 E I_z}{(kL)^2 g} \left[\sqrt{A + \Delta^2} - \Delta \right]$$

or, in expanded form:

$$M_{cr} = C_1 \frac{\pi^2 E I_z}{(kL)^2 g} \left[\left(\left(\frac{k}{k_w} \right)^2 \frac{I_w}{I_z} + \frac{(kL)^2 G I_t}{\pi^2 E I_z} + (C_2 z_g - C_3 z_j)^2 \right)^{1/2} - (C_2 z_g - C_3 z_j) \right]$$

This is the general expression for the elastic critical moment for lateral-torsional buckling of a prismatic open-section beam, symmetric about the plane of bending or monosymmetric, explicitly including:

- the lateral-bending contribution EI_z $[FL^2]$;
- the uniform-torsion contribution GI_t $[FL^2]$;
- the warping contribution EI_w $[FL^4]$;
- the lateral restraint conditions through k $[-]$;
- the warping-restraint conditions through k_w $[-]$;
- the bending-moment distribution through C_1 $[-]$;
- the load application level through z_g $[L]$;
- cross-sectional monosymmetry through z_j $[L]$;
- the correction factor g, generally close to unity for slender I-sections $[-]$.

1.7. Special cases

For a doubly symmetric section:

$$z_j = 0$$

The formula becomes:

$$M_{cr} = C_1 \frac{\pi^2 E I_z}{(kL)^2 g} \left[\left(\left(\frac{k}{k_w} \right)^2 \frac{I_w}{I_z} + \frac{(kL)^2 G I_t}{\pi^2 E I_z} + (C_2 z_g)^2 \right)^{1/2} - C_2 z_g \right]$$

If, in addition, the load is applied through the shear centre:

$$z_g = 0$$

the formula simplifies to:

$$M_{cr} = C_1 \frac{\pi^2 E I_z}{(kL)^2 g} \left[\left(\frac{k}{k_w} \right)^2 \frac{I_w}{I_z} + \frac{(kL)^2 G I_t}{\pi^2 E I_z} \right]^{1/2}$$

For ideal fork supports at the ends:

$$k = 1$$

$$k_w = 1$$

and for a constant bending moment (over the full member length L being verified):

$$C_1 = 1$$

the fundamental relationship is recovered:

$$M_{cr} = \frac{\pi^2 E I_z}{L^2 g} \left[\frac{I_w}{I_z} + \frac{L^2 G I_t}{\pi^2 E I_z} \right]^{1/2}$$

Finally, if $I_y \gg I_z$, then $g \simeq 1$, and therefore:

$$M_{cr} = \frac{\pi^2 E I_z}{L^2} \left[\frac{I_w}{I_z} + \frac{L^2 G I_t}{\pi^2 E I_z} \right]^{1/2}$$

2. Simplified formulation for doubly symmetric members

2.1. Overview of the phenomenon and classical formulation

Lateral-torsional buckling occurs in members subjected to bending when the compression flange, which may be idealised as a strut under axial compression, tends to buckle. In this kinematic and structural configuration, the member not only deflects laterally about the minor z–z axis but also twists about its shear centre, thereby adopting a spatially displaced and rotated configuration relative to its initial position.

For the fundamental case of a simply supported beam subjected to a constant bending-moment diagram over an unrestrained length L_b between two consecutive torsional restraints, with fork supports at the ends (torsional rotations and transverse displacements restrained, but warping free), the classical elastic solution gives the critical moment M_{cr} as:

$$M_{cr} = \frac{\pi}{L_b} \sqrt{E I_z G I_t} \cdot \sqrt{1 + \frac{\pi^2 E I_w}{G I_t L_b^2}}$$

where E is Youngś modulus, G is the shear modulus, I_z is the second moment of area about the minor axis, I_t is the Saint-Venant torsion constant and I_w is the warping constant governing non-uniform torsion.

For rolled or welded I-girders of moderate or high slenderness, it may be acceptable, for analytical purposes, to neglect the warping contribution relative to the Saint-Venant torsional component ($I_w \approx 0$). This assumption, which is strictly conservative, leads to the well-known simplified expression:

$$M_{cr} \approx \frac{\pi}{L_b} \sqrt{E I_z G I_t}$$

2.2. Connection with the CNR-UNI 10011 procedure and the elastic formulation

As a first approximation, to avoid explicitly calculating the individual inertia terms $\sqrt{I_z I_t}$, a geometric approximation of adequate accuracy, at least for doubly symmetric I-sections, is introduced, relating the weak-axis flexural and torsional properties directly to the elastic section modulus $W_{el,y}$ about the major axis:

$$\sqrt{I_z I_t} \approx 0.3 \cdot \frac{b_c\, t_c}{h} \cdot W_{el,y}$$

where b_c and t_c denote the width and thickness, respectively, of the compression flange. Substituting the numerical values of the elastic constants of steel ($E = 210000$ MPa and $G = 80800$ MPa), expressing the geometric quantities in millimetres [mm] and the section modulus $W_{el,y}$ in mm^3, gives the practical expression for the basic critical moment (in N · mm):

$$M_{cr,0} \approx 122000\, \frac{b_c\, t_c}{L_b\, h}\, W_{el,y}$$

To incorporate this result into a rapid verification procedure, it is related to the approach adopted in the Italian standard **CNR 10011-85** (Appendix A), which accounted for the destabilising effect of loads applied to the upper surface of the top flange by means of a global amplification factor $\beta = 1.4$. The lateral-stability verification was expressed in the CNR procedure by introducing an equivalent bending moment M_{eq}, defined as the uniform action producing a destabilising effect equivalent to that of the actual load distribution:

$$M_{eq} \le \frac{M_{cr,0}}{\beta} \implies \beta M_{eq} L_b \le W_{el,y} \cdot \frac{b_c\, t_c}{h} \cdot 122000 \quad (1)$$

The following rules were prescribed to convert the actual moment diagram into the equivalent value M_{eq}:

- Simply supported or continuous beam: $M_{eq} = 1.3 M_m$ (with $0.75 M_{\max} < 1.3 M_m < M_{\max}$)
- Cantilever beam: $M_{eq} = M_m$ (with $0.5 M_{\max} < M_m < M_{\max}$)

where M_m is the mean bending moment and $M_{\max}$ is the maximum moment along the member.

For a cantilever of length L subjected to a load producing a triangular moment diagram with a maximum value $M_{\max}$ at the fixed end, the mean moment is $M_{eq} = M_m = 0.5 M_{\max}$. To transfer the problem to an equivalent simply supported beam model, a kinematic analogy was adopted, whereby the deformed shape of a cantilever corresponds to the mirror image of half a simply supported beam ($L_b = 2L$):

$$M_{eq} L_b = (0.5 M_{\max})\,(2L) = M_{\max} L$$

To simplify the equation further by eliminating the depth parameters, approximations for the flanged geometry were introduced, neglecting the web contribution to the major-axis second moment of area:

$$I_y \approx \frac{b_c t_c h^2}{2} \implies W_{el,y} = \frac{I_y}{h/2} \approx b_c t_c h$$

Substituting the relationship $W_{el,y} \approx b_c t_c h$ into the stability inequality (Eq. (1)), the depth factor h cancels out. By adopting, in accordance with CNR, the coefficient $\beta = 1.4$ for doubly symmetric sections only and consistently converting the units (in particular, kN · cm for moments and cm for lengths), the following direct preliminary-sizing expression for the compression flange can be derived (see, for example, [36]):

$$(b_c t_c)^2\,[\mathrm{mm}^4] \ge 1.2 M_{\max}\,[\mathrm{kNcm}]\, L\,[\mathrm{cm}] \quad (2)$$

3. Extension to monosymmetric sections (bridge girders and composite systems)

The simplified formulation proposed for doubly symmetric sections can be generalised to include monosymmetric sections (e.g. the main girders of twin-girder or three-girder steel–concrete composite decks during slab casting).

To preserve the algebraic structure and ease of practical application of the original method, a *generalised shape coefficient* $\mathtt{f}$ is introduced, redefining the elastic critical moment M_{cr} in the following generalised equivalent form:

$$M_{cr} = \mathtt{f}\left(122000\, \frac{b_c\, t_c}{L_f\, h}\, W_{el,y}\right)$$

where b_c and t_c denote, respectively, the width and thickness of the *compression flange*, whose behaviour governs the kinematics of lateral-torsional buckling.

3.1. Analytical derivation of the coefficient $\mathtt{f}$

Consider the general theoretical formulation for monosymmetric members loaded through the centroid. For slender members, conservatively neglecting the warping-stiffness contribution ($I_w \approx 0$), the elastic critical moment is expressed as:

$$M_{cr} = C_1 \frac{\pi^2 E I_z}{(kL)^2}\left[\left(\frac{(kL)^2 G I_t}{\pi^2 E I_z} + (C_2 z_g - C_3 z_j)^2\right)^{1/2} - (C_2 z_g - C_3 z_j)\right]$$

By isolating the primary torsional term $\sqrt{G I_t/(E I_z)}$ and introducing the dimensionless coupled-buckling parameter μ defined by:

$$\mu := \frac{\pi \cdot (C_2 z_g - C_3 z_j)}{kL}\sqrt{\frac{E I_z}{G I_t}}$$

the complete expression can be factorised and reduced to the required simplified form. The overall coefficient $\mathtt{f}$ is defined as the product of three distinct contributions:

$$\mathtt{f} := C_1 \cdot k_{geo} \cdot \psi \tag{3}$$

The term ψ is the *mechanical factor* associated with the load application level and monosymmetry (Wagner effect):

$$\psi := \sqrt{1 + \mu^2} - \mu \tag{4}$$

The term k_{geo} is the *geometric asymmetry factor*, introduced to calibrate the simplified relationship for the inertia product $\sqrt{I_z I_t}$ based on the elastic section modulus $W_{el,y}$ of the asymmetric section:

$$k_{geo} := \sqrt{2\rho_c}\left(\frac{y_c}{0.5\,h}\right) \tag{5}$$

where $\rho_c = I_{z,c}/I_z$ is the ratio between the minor-axis second moment of area of the compression flange alone and that of the complete section, and y_c is the distance from the geometric centroid of the entire section to the axis of the compression flange.

3.2. Convergence check for the doubly symmetric limiting case

To demonstrate the mathematical consistency of the proposed extension, consider the limiting case of a doubly symmetric I-girder loaded through the shear centre under a uniform bending-moment diagram. Under these conditions, the following geometric and kinematic identities apply:

1. **Vanishing eccentricities:** The load application point coincides with the shear centre ($z_g = 0$) and the Wagner asymmetry parameter vanishes ($z_j = 0$). Consequently, Eq. (4) gives $\mu = 0$, and the mechanical factor reduces to unity:

   $$\psi = \sqrt{1 + 0^2} - 0 = 1$$

2. **Geometric flange symmetry:** The flanges are identical, and the minor-axis second moment of area is therefore equally distributed ($\rho_c = 0.5$). The cross-sectional centroid lies exactly at mid-depth ($y_c = 0.5\,h$). Substitution into Eq. (5) gives:

   $$k_{geo} = \sqrt{2 \cdot 0.5} \cdot \left(\frac{0.5\,h}{0.5\,h}\right) = 1 \cdot 1 = 1$$

3. **Uniform moment:** For a uniform bending-moment diagram, the moment-diagram correction coefficient is unity ($C_1 = 1.0$).

Substitution of Eqs. (4) and (5), together with the value of C_1, into Eq. (3) formally gives:

$$\mathtt{f} = 1 \cdot 1 \cdot 1 = 1$$

This demonstrates that, for doubly symmetric sections under standard loading conditions, the generalised shape coefficient $\mathtt{f}$ is exactly equal to 1, and the extended formulation rigorously reduces to the original "basic" formulation.

3.3. Improving the approximation: inclusion of warping stiffness

To avoid excessive conservatism in the simplified formulation, which would be unduly penalising and of limited practical use in infrastructure design, the simplifying assumption of zero warping stiffness ($I_w \approx 0$) is removed. In monosymmetric bridge girders, when the unrestrained length L_b between torsional restraints is relatively short, warping stiffness provides a non-negligible stabilising contribution.

A *warping-stiffness factor* κ is therefore introduced into the expression for the overall shape coefficient $\mathtt{f}$, in the closed form:

$$\kappa := \sqrt{1 + \frac{\pi^2 E I_w}{G I_t L_b^2}}$$

For monosymmetric I-sections, the warping constant I_w can be determined analytically without numerical modelling by exploiting the kinematic decomposition of the individual flanges:

$$I_w = \rho_c(1 - \rho_c)\, I_z h^2 \tag{6}$$

where $\rho_c = I_{z,c}/I_z$ is the previously defined minor-axis inertia distribution coefficient. For direct calculation, the minor-axis properties of the welded monosymmetric section are expressed in closed form, neglecting weld-toe radii. The second moment of area $I_{z,c}$ of the compression flange alone is:

$$I_{z,c} = \frac{t_c b_c^3}{12}$$

while the total second moment of area I_z of the section is obtained by summing the contributions of the compression flange, tension flange and web:

$$I_z = \frac{t_c b_c^3}{12} + \frac{t_t b_t^3}{12} + \frac{h_w t_w^3}{12}$$

where b_t and t_t are the width and thickness of the tension flange, and h_w and t_w are the web dimensions. The distribution parameter ρ_c introduced in Eq. (6) therefore has the following analytical form:

$$\rho_c = \frac{I_{z,c}}{I_z} = \frac{t_c\, b_c^3}{t_c\, b_c^3 + t_t\, b_t^3 + h_w\, t_w^3}$$

3.4. Calibration framework in accordance with EN 1993

The operational formulation is reorganised by clearly distinguishing three levels of calculation:

1. exact or approximate estimation of the elastic critical moment M_{cr} (first-order theory);
2. conversion of M_{cr} into the lateral-torsional slenderness $\bar{\lambda}_{LT}$;
3. evaluation of the design resistance $M_{b,Rd}$ through the reduction factor χ_{LT}.

The elastic critical moment remains an elastic stability quantity; the design resistance to lateral-torsional buckling is obtained only after applying the buckling curve specified in Eurocode 3.

For each section and each segment between two consecutive torsional restraints, the following code-based sequence is adopted as the reference:

$$\bar{\lambda}_{LT} = \sqrt{\frac{W_y f_y}{M_{cr}}}$$

$$\Phi_{LT} = \frac{1}{2}\left[1 + \alpha_{LT}\left(\bar{\lambda}_{LT} - 0.20\right) + \bar{\lambda}_{LT}^2\right]$$

$$\chi_{LT} = \min\left\{1, \frac{1}{\Phi_{LT} + \sqrt{\Phi_{LT}^2 - \bar{\lambda}_{LT}^2}}\right\}$$

$$M_{b,Rd} = \chi_{LT}\frac{W_y f_y}{\gamma_{M1}}$$

where W_y is the section modulus consistent with the cross-section class: $W_{pl,y}$ for Class 1 or 2 sections, $W_{el,y}$ for Class 3 sections and $W_{eff,y}$ for Class 4 sections. The general method of EN 1993-1-1 is adopted to determine the lateral-torsional buckling reduction factor; in this method, the quadratic term has a unit coefficient and the additional limit $1/\bar{\lambda}_{LT}^2$, associated with the modified formulation, does not apply.

For welded bridge girders, which are generally monosymmetric and potentially slender, the cross-section must therefore first be classified and, where necessary, treated using effective-section properties.

The proposed formulation follows the provisions of the structural Eurocodes developed by CEN/TC 250 when converting M_{cr} into $M_{b,Rd}$.

3.5. Reference elastic critical moment

For the calibration of the simplified parametric method presented here, the reference value is the elastic critical moment obtained from the complete lateral-torsional buckling formulation, including the effects of warping, effective length, moment distribution, load application level and monosymmetry:

$$M_{cr,ref} = C_1\frac{\pi^2 EI_z}{L_b^2 g}\left[\left(\left(\frac{L_b}{L_w}\right)^2\frac{I_w}{I_z} + \frac{L_b^2 GI_t}{\pi^2 EI_z} + \Delta^2\right)^{1/2} - \Delta\right] \tag{7}$$

where:

$$\Delta = C_2 z_g - C_3 z_j$$

In Eq. (7), L_b is the unrestrained distance between two consecutive lateral-torsional restraints and L_w is the corresponding effective length for warping. For the common case of free warping at the ends of the segment, $L_w = L_b$ is adopted as a first approximation. The parameter g accounts for the ratio between the principal flexural stiffnesses; for slender I-girders, in which $I_y \gg I_z$, the approximation $g \simeq 1$ was adopted only after numerical verification.

For doubly symmetric sections, $z_j = 0$. For monosymmetric welded bridge-girder sections, however, z_j must be calculated and cannot be assumed to vanish. The load level z_g must be evaluated relative to the shear centre using the stated sign convention (see Fig. 1). In the parabolic branch, for which $C_2 > 0$, a load applied to the top surface of the upper flange introduces the usual destabilising contribution. In the locally uniform-moment branch adopted in this campaign, however, $C_2 = 0$, so z_g does not appear directly in the expression for M_{cr}.

In the present statistical campaign, the unrestrained segment is represented by two limiting models, without using the earlier reconstruction based on the root-mean-square moment diagram and an artificial curvature index. Defining:

$$\xi_b = \frac{L_b}{L},$$

for simplicity, the following operational rule was adopted (Fig. 2):

$$(C_1, C_2, C_3) = \begin{cases}(1.000, 0.000, 1.000), & \xi_b < 0.25,\\ (1.132, 0.459, 0.525), & \xi_b \geq 0.25.\end{cases} \tag{8}$$

The first branch represents a short segment assumed to be subjected to a locally uniform bending moment; the second represents the parabolic moment diagram of a simply supported beam. The threshold $\xi_b = 0.25$ belongs to the second branch. This threshold is an operational discretisation adopted for the present campaign and must not be interpreted as a general EN 1993 requirement; the values in the two branches remain those associated with the corresponding limiting models.

The three identifiers `SS_UDL_CENTER`, `SS_UDL_LEFT` and `SS_UDL_RIGHT` are retained in the audit files but, in the calibrated version presented here, do not alter the coefficients. The adopted trend is shown in Fig. 2.

3.6. Classification of geometric families in the REV3 domain

Hereafter, the terms *frequent/usual* and *less frequent/boundary* do not denote the probability with which a given section occurs in practice. They identify only the position of its geometric ratios within the parametric domain adopted for REV3 calibration. The operational classification is summarised in Table 1.

The term *less frequent* must therefore be interpreted as identifying a geometry that is less representative of the parametric population used for calibration, rather than as a measure of its actual frequency of use in design practice.

3.7. Proposed simplified parametric formulation for preliminary sizing of welded sections

The simplified formulation is not obtained by imposing an approximate value of χ_{LT}, nor by directly regressing

Table 1. *Classification of the geometric families adopted in the REV3 parametric campaign.*

Family	Geometric criteria	Operational interpretation
Frequent/usual	The section simultaneously satisfies: $10\,\mathrm{mm} \le t_w \le 25\,\mathrm{mm}$, $3.65 \le h/b_c \le 4.90$, $110 \le h_w/t_w \le 150$, $1.30 \le b_t/b_c \le 2.30$, $1.80 \le t_t/t_c \le 2.70$.	Geometry within the central and most representative part of the calibration domain. For this family, $k_D = 1$ is adopted.
Less frequent/boundary	The section lies entirely within the extended domain: $10\,\mathrm{mm} \le t_w \le 25\,\mathrm{mm}$, $3.50 \le h/b_c \le 5.20$, $100 \le h_w/t_w \le 300$, but at least one geometric ratio does not $1.10 \le b_t/b_c \le 2.60$, $1.60 \le t_t/t_c \le 3.00$, satisfy the limits of the frequent/usual family.	Peripheral geometry, less representative of the statistical population or close to the boundaries of its support. The domain correction factor k_D is applied to this family.
Out of range	At least one geometric quantity lies outside the extended less frequent/boundary domain.	The approximate procedure cannot be used as a stand-alone method. The complete EN 1993 verification and, where appropriate, a dedicated numerical analysis are required.

Note. The geometric family is independent of the unrestrained length against lateral-torsional buckling L_b, the number n_{long} of longitudinal-stiffener levels and the choice of the uniform or parabolic branch. These quantities enter the subsequent steps of the procedure but do not determine whether the section belongs to the "frequent/usual" or "less frequent/boundary" family.

the elastic critical moment. The basic geometric quantity is the compression-flange area:

$$A_c = b_c t_c.$$

The preliminary verification retains the following form (based on the fundamental formulation in Eq. 2 on page 7):

$$A_c^2 \ge \widehat{\alpha}_{LT} M_{eq} L_b \tag{9}$$

where M_{eq} is the equivalent moment over the unrestrained segment L_b. In REV3 calibration[3], the approximate parameter is expressed through the compact model $M3_{\mathrm{domain}}$:

$$\begin{aligned} \widehat{\alpha}_{LT} &= \alpha_0\, k_L\, B_s\, C_f\, k_f\, k_C\, k_n\, k_\tau\, k_D, \\ \alpha_0 &= \frac{A_c^2}{M_{y,Rk} L_b}, \qquad M_{y,Rk} := W_y f_y. \end{aligned} \tag{10}$$

The moment-distribution coefficients C_1, C_2 and C_3, which enter the *torsional proxy*[4] defined below, are selected using the two-branch rule in Eq. (8). Their dependence on the ratio L_b/L is shown in Fig. 2; the figure is placed immediately below to make the transition between the short-segment and parabolic branches explicit. In the statistical analysis, the effect of unrestrained length is represented by the positive multiplicative factor k_L, calibrated in logarithmic space through a quadratic response surface:

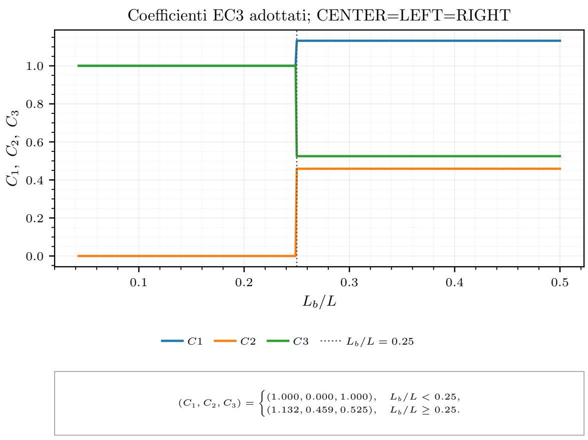

Figure 2. *Adopted coefficients C_1, C_2, C_3 as functions of L_b/L; the threshold $L_b/L = 0.25$ separates the locally uniform-moment branch from the parabolic branch. The initial green segment overlaps the blue segment.*

$$\begin{aligned} k_L &= \exp\left(c_0 + c_1 x_L + c_2 x_L^2\right), \\ x_L &= \ln\left[\frac{(L_b/L)}{0.10}\right], \\ c_0 &= 0, \quad c_1 = 0.1744, \quad c_2 = 0.0043. \end{aligned} \tag{11}$$

The variable x_L is a logarithmic coordinate centred on the reference value $L_b/L = 0.10$. Therefore, for $L_b/L = 0.10$, $x_L = 0$ and, because $c_0 = 0$ was imposed,

[3] The designation *REV3* denotes the third revision of the statistical calibration procedure developed in this study. This revision includes the final parametric population, the adoption of $\gamma_{M1} = 1.10$, the constrained calibration of the compact model $M3_{\mathrm{domain}}$, the definition of the dimensionless design charts and their pointwise validation within the geometric and mechanical domains considered.

[4] The *torsional proxy* is a synthetic dimensionless quantity that approximately represents the influence of torsional and warping stiffness on the lateral-torsional behaviour of the girder cross-section.

$k_L = 1$. The exponential transformation also ensures that the length factor is always positive. The following dimensionless explanatory variables, also expressed as centred logarithmic coordinates, are introduced to describe the geometric effects of the monosymmetric section:

$$\begin{aligned} x_h &= \ln\left[\frac{(h/b_c)}{4}\right], \quad x_w = \ln\left[\frac{(h_w/t_w)}{180}\right], \\ x_b &= \ln\left[\frac{(b_t/b_c)}{1.20}\right], \quad x_t = \ln\left[\frac{(t_t/t_c)}{2}\right]. \end{aligned} \tag{12}$$

The quantities x_h, x_w, x_b and x_t are the *normalised explanatory variables* of the statistical model. The denominators 4, 180, 1.20 and 2 define the reference geometry, for which all coordinates are zero. The logarithmic transformation converts multiplicative effects of the geometric ratios into additive contributions in the regression model. The coordinates x_h and x_w measure the effects of the depth ratio h/b_c and web slenderness h_w/t_w, respectively; their influence on the statistical formula and torsional component is illustrated in Figs. 3 and 4. The coordinates x_b and x_t describe the effects of the flange-asymmetry ratios b_t/b_c and t_t/t_c, shown in Figs. 5 and 6. The discrete effect of longitudinal stiffeners is introduced through the indicator, or *dummy*, variables N_1 and N_2:

$$N_1 = \begin{cases} 1, & n_{\text{long}} = 1, \\ 0, & n_{\text{long}} \neq 1, \end{cases} \qquad N_2 = \begin{cases} 1, & n_{\text{long}} = 2, \\ 0, & n_{\text{long}} \neq 2. \end{cases} \tag{13}$$

The cross-section without longitudinal stiffeners, $n_{\text{long}} = 0$, is the reference category, for which $N_1 = N_2 = 0$. The coefficients associated with N_1 and N_2 therefore represent the statistical deviation from this basic configuration. The geometric exponents q_h, q_w, q_b and q_t are response variables estimated by the model. They are represented by first-order linear response surfaces, in which the constant term is the intercept, while the coefficients associated with x_L, N_1 and N_2 represent the main effects of the corresponding explanatory variables:

$$\begin{aligned} q_h &= 0.3081 + 0.0144x_L - 0.0043N_1 + 0.0004N_2, \\ q_w &= -0.0554 + 0.0133x_L - 0.0250N_1 - 0.0203N_2, \\ q_b &= -0.3515 + 0.1002x_L + 0.0397N_1 + 0.0424N_2, \\ q_t &= -0.1342 + 0.0247x_L + 0.0312N_1 + 0.0409N_2. \end{aligned} \tag{14}$$

The numerical values in these relationships are the regression coefficients calibrated against the REV3 statistical population. In particular, the exponents q_h, q_w, q_b and q_t vary with relative length and stiffener configuration rather than being assumed constant throughout the domain. The corresponding multiplicative geometric factors are finally defined as:

$$B_s = \exp(q_h x_h + q_w x_w), \qquad C_f = \exp(q_b x_b + q_t x_t). \tag{15}$$

The factor B_s combines the effects associated with section depth and web slenderness, whereas C_f represents the effects of flange asymmetry. The exponential form ensures $B_s > 0$ and $C_f > 0$ and converts the calibrated linear combinations into multiplicative factors applicable to the compact model. Figs. 3–6 explicitly show the role of the four coordinates in Eq. (12) in the factors B_s and C_f of Eq. (15). The figures below allow direct comparison between web and flange parameters. The multiplicative factors associated with steel strength, the coefficient C_1 and the number of stiffeners are expressed in general form as:

$$\begin{aligned} x_f &= \ln\left(\frac{f_y}{355}\right), & k_f &= \exp(a_f x_f), \\ x_C &= \ln\left(\frac{C_1}{C_{1,\text{ref}}}\right), & k_C &= \exp(a_C x_C), \\ k_n &= \exp(a_{N_1} N_1 + a_{N_2} N_2). \end{aligned} \tag{16}$$

The constraints $C_{1,\text{ref}} = 1$ and $a_f = a_C = a_{N_1} = a_{N_2} = 0$ were imposed during calibration of the statistical model, which directly yields $k_f = k_C = k_n = 1$. This choice removes independent multiplicative contributions associated with these quantities; within the calibration domain, their effects on the response are therefore embedded in the cross-sectional properties, geometric exponents and variables defining the *torsional proxy*.

The torsional factor is then defined as:

$$k_\tau = \exp(P_\tau), \tag{17}$$

with the general polynomial:

$$\begin{aligned} P_\tau = 0.1100 &+ 0.7082q_\tau + 0.2481u_\tau + \\ &+ 0.1710q_\tau^2 - 0.0276u_\tau^2 + 0.3661q_\tau u_\tau. \end{aligned} \tag{18}$$

All the terms shown are retained in the REV3 calibration. The proxy variables are defined as:

$$\begin{aligned} S_\tau &= \frac{I_w}{I_z} + \frac{L_b^2 G I_t}{\pi^2 E I_z}, & \Delta &= C_2 z_g - C_3 z_j, \\ M_\tau &= C_1 \frac{\pi^2 E I_z}{L_b^2}\sqrt{S_\tau}, & u_\tau &= \frac{\Delta}{\sqrt{S_\tau}}, \\ \lambda_\tau &= \sqrt{\frac{M_{y,Rk}}{M_\tau}}, & q_\tau &= \max(0, \lambda_\tau - 0.25). \end{aligned} \tag{19}$$

The moment M_τ is a torsional proxy constructed specifically for this procedure; it does not coincide with M_{cr} and does not introduce M_{cr}, $\overline{\lambda}_{LT}$ or χ_{LT} into the application sequence. Denoting the “frequent/usual” domain by $D = F$ and the “less frequent/boundary” domain by $D = B$, the domain factor is defined as:

$$\begin{aligned} p_D(x_L, x_w) = 0.0205 &- 0.0448x_L \\ &+ 0.0420x_L^2 + 0.0213x_w + 0.0159x_w x_L, \\ \ln k_D &= \begin{cases} 0, & D = F, \\ p_D(x_L, x_w), & D = B. \end{cases} \end{aligned} \tag{20}$$

The demand associated with the approximate procedure may be expressed through the quantity:

$$R_{app} := \widehat{\alpha}_{LT} M_{eq} L_b, \qquad A_c^2 \geq R_{app}, \tag{21}$$

while the equivalent resistance moment is:

$$M_{b,Rd}^{app} = \frac{A_c^2}{\widehat{\alpha}_{LT} L_b}. \tag{22}$$

The geometry, longitudinal stiffeners, steel strength and coefficients C_1, C_2, C_3 therefore act through the cross-sectional properties, the variables q_τ, u_τ, x_L, and the geometric factors B_s and C_f.

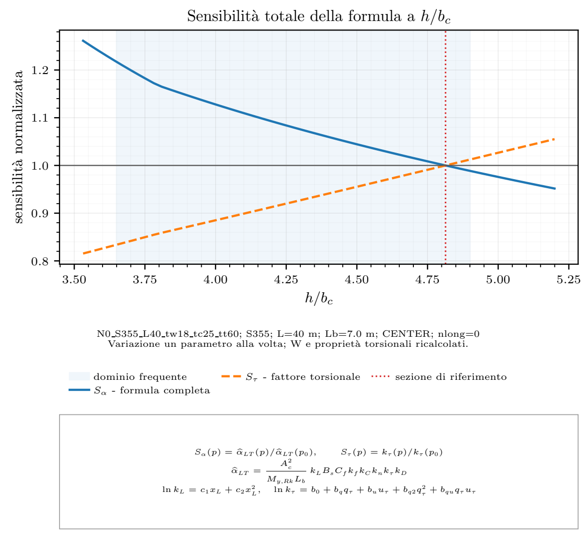

Figure 3. *Sensitivity of the final formula to the ratio h/b_c, associated with the coordinate x_h in Eq. (12).*

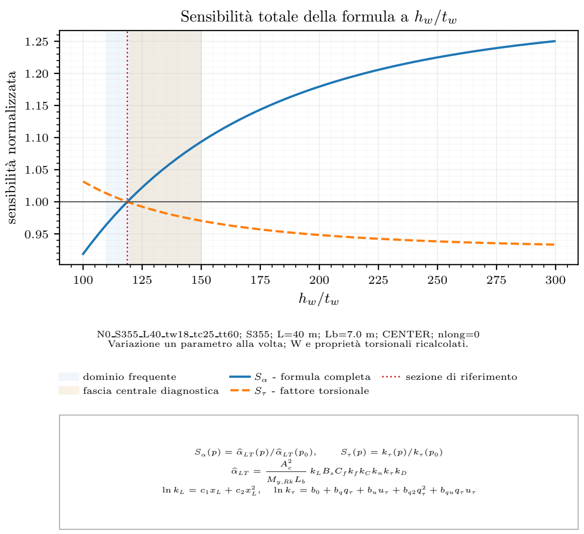

Figure 4. *Sensitivity of the final formula to web slenderness h_w/t_w, associated with the coordinate x_w in Eq. (12).*

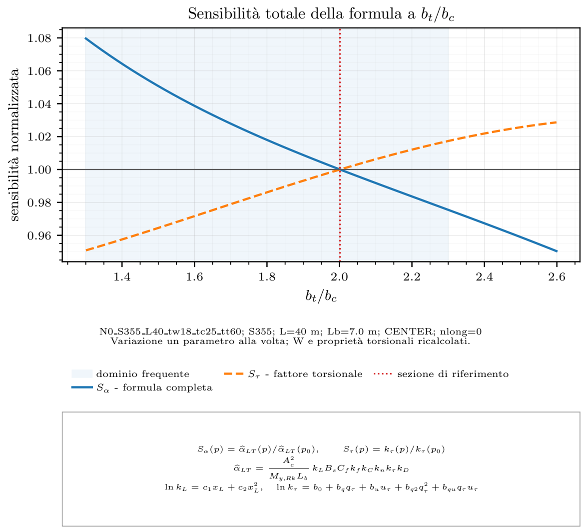

Figure 5. *Sensitivity of the final formula to the ratio b_t/b_c, associated with the coordinate x_b in Eq. (12).*

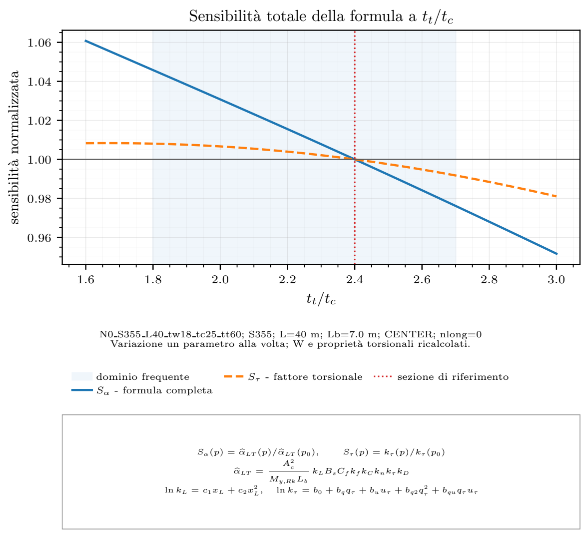

Figure 6. *Sensitivity of the final formula to the ratio t_t/t_c, associated with the coordinate x_t in Eq. (12).*

3.8. Definition of the EC3 calibration parameter

For each case in the parametric population, the complete EN 1993 resistance, denoted by $M_{b,Rd,i}^{EC3}$, is calculated. It is used solely as the calibration reference and does not enter the operational sequence of the simplified formula. The pointwise code parameter is:

$$\alpha_{LT,i}^{EC3} = \frac{A_{c,i}^2}{M_{b,Rd,i}^{EC3} L_{b,i}}.$$

The numerical values of α_{LT}^{EC3}, α_0 and $\widehat{\alpha}_{LT}$ refer to the operational unit convention adopted throughout the calibration: A_c in mm^2, moments in $\mathrm{kN\,cm}$, and L_b in centimetres. The ratio ρ_i, by contrast, is dimensionless. This convention was applied consistently throughout, without mixing units. The quality and conservatism of the prediction are controlled through the calibration ratio, or multiplicative residual,

$$\rho_i = \frac{\widehat{\alpha}_{LT,i}}{\alpha^{EC3}_{LT,i}}.$$

The value $\rho_i = 1$ denotes exact agreement with the EC3 reference, whereas $\rho_i > 1$ indicates a conservative prediction and $\rho_i < 1$ a non-conservative underestimate. The calibration is pointwise: population means or percentiles are not sufficient. The following domain-specific control limits were imposed for every row:

$$1.000 \le \rho_i \le 1.150 \qquad \text{“frequent/usual”},$$

$$1.000 \le \rho_i \le 1.2075 \quad \text{“less frequent/boundary”}.$$

The value $k_B = 1.05$ defines only the upper statistical tolerance for the boundary domain, namely $1.15k_B = 1.2075$, and is not a coefficient to be multiplied in the operational verification. By contrast, the calibrated factor k_D, which is distinct from k_B, is defined by Eq. (20): it is equal to one in the frequent domain and follows the stated polynomial law in the boundary domain. The training/test split is performed by `geometry_id`, so that all combinations associated with the same geometry remain in a single subset and no leakage occurs between calibration and validation.

3.9. REV3 database and traceability

The population was regenerated in full using specific relationships reported by De Miranda ([16, pp. 125–133]). For each of the three configurations with $n_{\text{long}} = 0, 1, 2$, 21592 configurations were assessed, for a total of 64776 cross-sectional verifications according to EN 1993. Regeneration produced neither errors nor numerical rejections, and the thirteen basic CSV files match the certified REV3 population byte-for-byte.

Application of the formal geometric limits selects 3296 sections for each stiffener configuration, giving a total of 9888 statistical sections. The distribution is:

$$N_F = 2103, \qquad N_B = 7785, \qquad N_{\text{tot}} = 9888,$$

where the subscripts F and B denote the “frequent/usual” and “less frequent/boundary” domains, respectively. The remaining 54888 sectional configurations are retained in the audit as “outside the support” and were excluded from calibration. For each section, the 61 values of L_b between $3.00\,\text{m}$ and $15.00\,\text{m}$, at increments of $0.20\,\text{m}$, were applied. This gives $9888 \times 61 = 603168$ physical section–unrestrained-length combinations, and therefore the same number of EN 1993 cross-sectional verifications. The three identifiers `SS_UDL_CENTER`, `SS_UDL_LEFT` and `SS_UDL_RIGHT` are retained for compatibility and audit purposes, but use the same two-branch rule for the coefficients C_1, C_2, C_3 (Fig. 2). The complete statistical population therefore contains $603168 \times 3 = 1809504$ records. The training/test split is grouped by `split_group_id`; to ensure a statistically valid analysis, no geometry appears in both subsets.

4. Statistical calibration analysis of the REV3 parametric model

4.1. Selected model

The final calibration adopts the model $M3_{\text{domain}}$, defined by Eqs. (10)–(20). The exponents directly associated with f_y, C_1 and the number of stiffeners were subject to fixed calibration constraints requiring them to be zero:

$$a_f = a_C = a_{N_1} = a_{N_2} = 0, \qquad k_f = k_C = k_n = 1.$$

The effects of material and stiffeners are not removed: they enter through the adopted section modulus, the properties I_z, I_t, I_w, z_g, z_j, the torsional variables, and the geometric exponents. The factor k_D is equal to one in the frequent domain and varies in the boundary domain; it is not the same as $k_B = 1.05$, which remains solely the upper statistical acceptance tolerance imposed as a calibration constraint. Reconstruction of the intermediate variables over the full population gives:

$$\max|\Delta\lambda_\tau|, \max|\Delta q_\tau|, \max|\Delta u_\tau| \le 5.01 \times 10^{-13},$$

well below the prescribed tolerance of 10^{-9}.

4.2. Pointwise validation

The conservatism ratio is defined as:

$$\rho_i := \frac{\widehat{\alpha}_{LT,i}}{\alpha^{EC3}_{LT,i}}. \tag{23}$$

Calibration and validation are accepted only if every row satisfies its applicable interval. The final results are reported in Table 2. No cases with $\rho_i < 1$ or exceedances of the limits 1.150 and 1.2075, imposed as calibration “accuracy” limits, were found. Acceptance decisions, monotonicity audits and row-by-row predictions are retained in files M00–M18 of the package.

4.3. Unrestrained-segment coefficients and sensitivity

The two-branch rule for the coefficients C_1, C_2, C_3 is shown in Fig. 2, placed directly in Section 3.7 next to the definition of the compact model. One-at-a-time variations of the ratios h/b_c, h_w/t_w, b_t/b_c and t_t/t_c are shown, in the same order in which the parameters are introduced, in Figs. 3–6.

For every point in the parametric population, the cross-section class, section modulus, torsional properties and the value returned by the implemented statistical formula are recalculated directly. The results are therefore not altered by corrective interpolation or graphical *smoothing*.

Table 2. *Pointwise validation of the $M3_{\mathrm{domain}}$ model.*

Dataset	Domain	N	$\rho_{\min}$	ρ_{50}	ρ_{95}	$\rho_{\max}$
Training	Frequent/usual	287676	1.007666	1.051520	1.080860	1.106750
Test	Frequent/usual	97173	1.006219	1.050878	1.081126	1.101360
Training	Less frequent/boundary	1063413	1.007744	1.065644	1.115324	1.177869
Test	Less frequent/boundary	361242	1.007847	1.065044	1.112846	1.172562

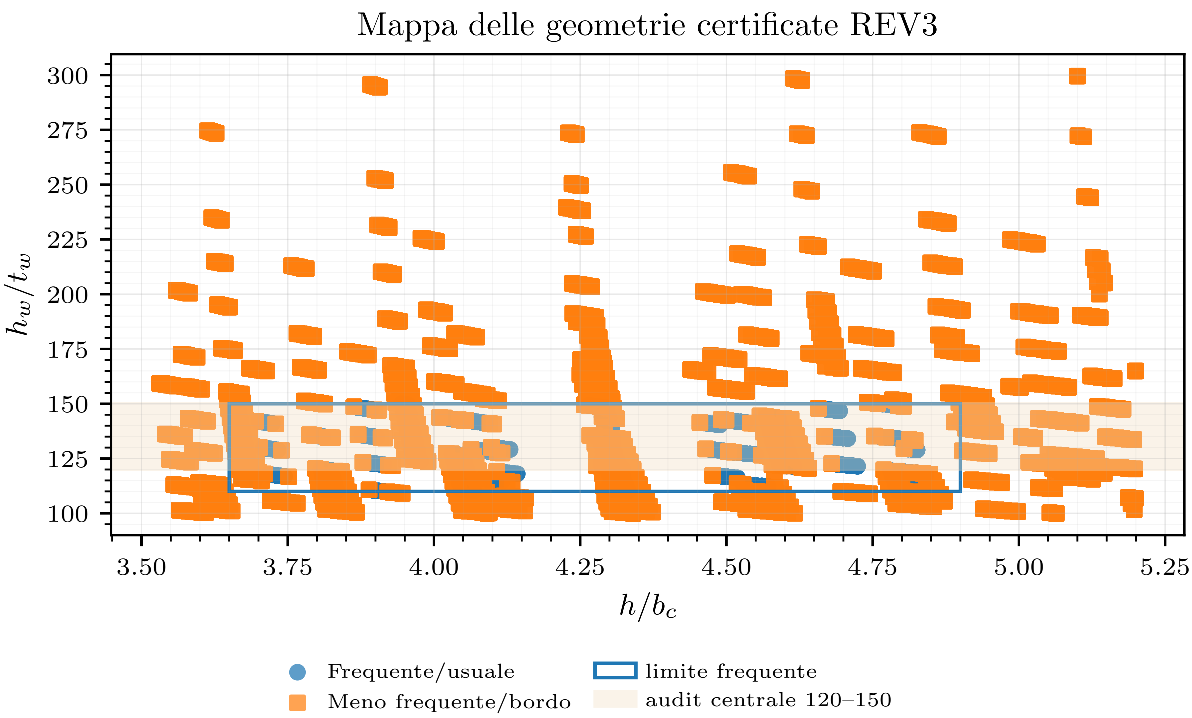

$$\mathcal{D}_F: \; 3.65 \le h/b_c \le 4.90, \;\; 110 \le h_w/t_w \le 150$$
$$\mathcal{D}_B = \mathcal{D}_{\mathrm{estesa}} \setminus \mathcal{D}_F$$

Figure 7. *Map of the* 9888 *certified REV3 statistical sections in the "frequent/usual" and "less frequent/boundary" domains.*

5. Operational dimensionless design charts

5.1. Construction and support

The design charts do not directly regress q_τ and u_τ. Their inputs consist solely of dimensionless ratios derived from nominal dimensions, normalised strength f_y/E, the number of longitudinal-stiffener levels and the branch of the C_i coefficients. The following input parameters are introduced:

$$\beta_c = \frac{b_c}{h}, \quad \tau_c = \frac{t_c}{h}, \quad \beta_t = \frac{b_t}{h}, \quad \tau_t = \frac{t_t}{h}, \\ \tau_w = \frac{t_w}{h}, \quad \gamma_A = \frac{b_t t_t}{b_c t_c}, \quad \beta_s = \frac{b_s}{h}, \quad \tau_s = \frac{t_s}{h}. \tag{24}$$

The input vector of the graphical model consists of the logarithms of the ratios in Eq. (24), supplemented by the ratios h/b_c, h_w/t_w, b_t/b_c, t_t/t_c, and, in the Ξ_λ model, by f_y/E:

$$\begin{aligned} \boldsymbol{\xi}^{(n)} = \big[&\ln \beta_c, \ln \tau_c, \ln \beta_t, \ln \tau_t, \ln \tau_w, \\ &\ln \gamma_A, \ln(h/b_c), \ln(h_w/t_w), \\ &\ln(b_t/b_c), \ln(t_t/t_c), \\ &\ln \beta_{s,1}, \ln \tau_{s,1}, \ldots, \\ &\ln \beta_{s,n}, \ln \tau_{s,n}, \ln(f_y/E) \big]^{\mathsf{T}}. \end{aligned} \tag{25}$$

The three synthetic coordinates are obtained from the polynomial maps published in the supplementary file `ABACUS_dimensionless_coefficients.json`:

$$\begin{aligned} \ln \widehat{\kappa}_\psi &= \mathcal{P}_\psi^{(n)}(\boldsymbol{\xi}^{(n)}), \\ \ln \Xi_{u,0} &= \mathcal{P}_u^{(n,C)}(\boldsymbol{\xi}^{(n)}), \\ \ln \Xi_\lambda &= \mathcal{P}_\lambda^{(n)}(\boldsymbol{\xi}^{(n)}). \end{aligned} \tag{26}$$

The polynomial maps were developed so that no preliminary calculation of I_t, I_w, z_g, z_j or M_{cr} is required.

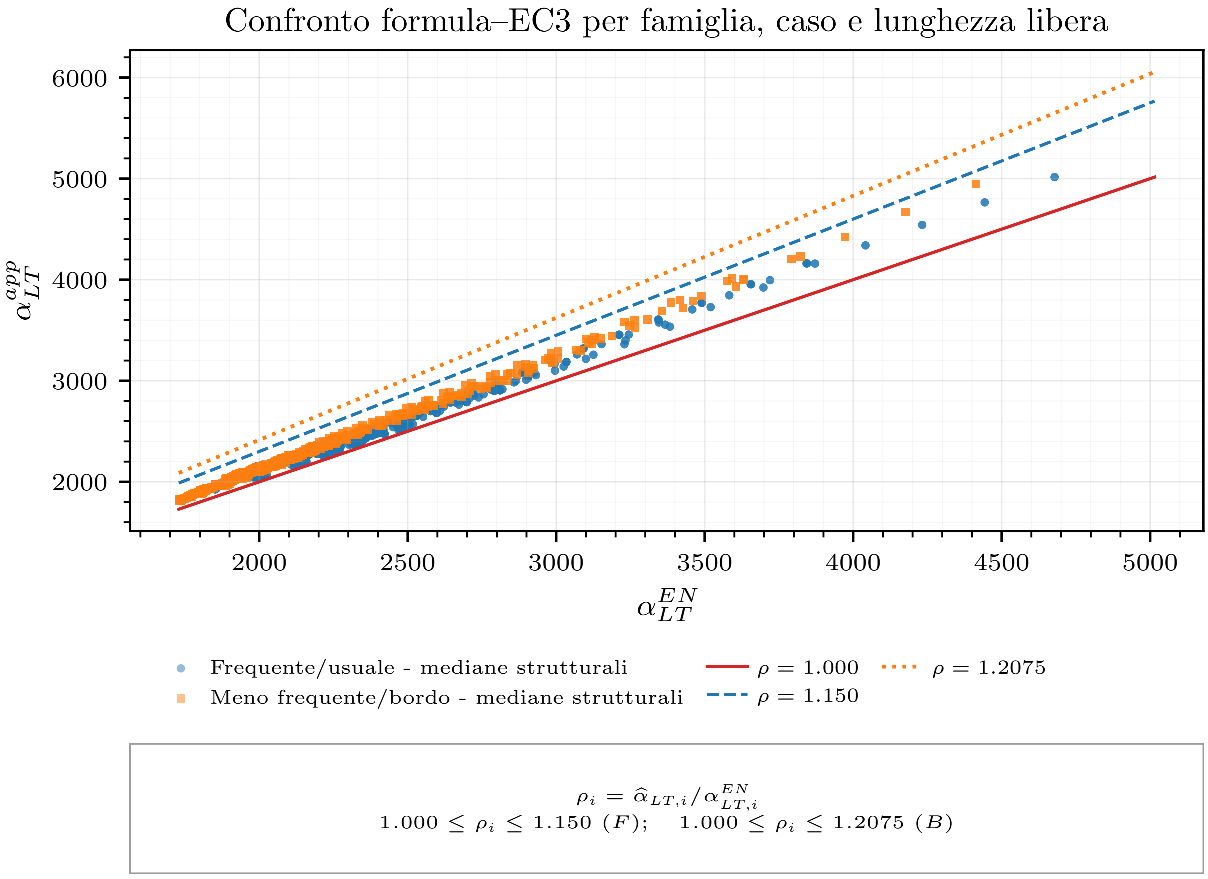

Figure 8. *Comparison between the EN 1993 parameter and the final prediction, including the conservatism lines and the upper domain limits.*

Dependence on the dimensionless length $\ell_b = L_b/h$ is then reconstructed through the parameters:

$$\psi_\tau = \widehat{\kappa}_\psi \ell_b, \qquad \widehat{u}_\tau = \frac{\Xi_{u,0}}{\sqrt{1+\psi_\tau^2}}, \tag{27}$$

$$\widehat{\lambda}_\tau = \frac{\Xi_\lambda}{\sqrt{C_1}} \frac{\ell_b}{(1+\psi_\tau^2)^{1/4}}, \qquad \widehat{q}_\tau = \max(0, \widehat{\lambda}_\tau - 0.250). \tag{28}$$

To preserve pointwise conservatism after graphical interpolation, the final parameter obtained from the charts also includes the local coefficient k_A (Table 6 on page 26), selected according to the domain, n_{long}, the C branch and the interval of ℓ_b:

$$\widehat{\alpha}_{LT}^{\mathrm{abaco}} = k_A\, \alpha_0 k_L B_s C_f k_f k_C k_n k_\tau(\widehat{q}_\tau, \widehat{u}_\tau) k_D. \tag{29}$$

The coefficient k_A is neither a code coefficient nor a statistical tolerance: it is the certified local realignment of the graphical procedure relative to the equations of the statistical model. The auxiliary campaign contains 5112 sectional configurations and 347616 exact targets. Fitting is grouped, and the specific P1 section is excluded from calibration. The chart error is propagated directly to $\widehat{\alpha}_{LT}$ and ρ over the entire physical population of 603168 rows.

The propagation results are:

$$\min\left(\frac{\widehat{\alpha}_{LT}^{\text{design chart}}}{\widehat{\alpha}_{LT}^{\text{equations}}}\right) = 1.0004.$$

$$1.0098 \le \rho^{\text{design chart}} \le 1.2045.$$

No underestimates, sign errors in u_τ, or violations of the upper limits were found. Ten independent official geometries belonging exclusively to the test subset were also verified.

5.2. Accuracy of the design charts

For u_τ, the median relative error is 0.1330%, the 95th percentile is 0.4074%, and the maximum is 1.4223%. For λ_τ, the corresponding values are 0.1996%, 0.7633%, and 2.8738%. For q_τ, the absolute error is considered primarily, because the relative error is not meaningful near the zero threshold: median 6.667×10^{-4}, 95th percentile 4.237×10^{-3}, maximum 2.199×10^{-2}. The external P1 benchmark, excluded from fitting, is developed in full in Section 6, where the complete EN 1993 procedure is compared with manual reading of the charts.

6. Comparative worked example for the P1 test section

6.1. Load analysis during slab casting

The geometric assumptions and characteristic loads adopted for the casting stage are summarised in Table 3. During casting, the slab is not yet composite and

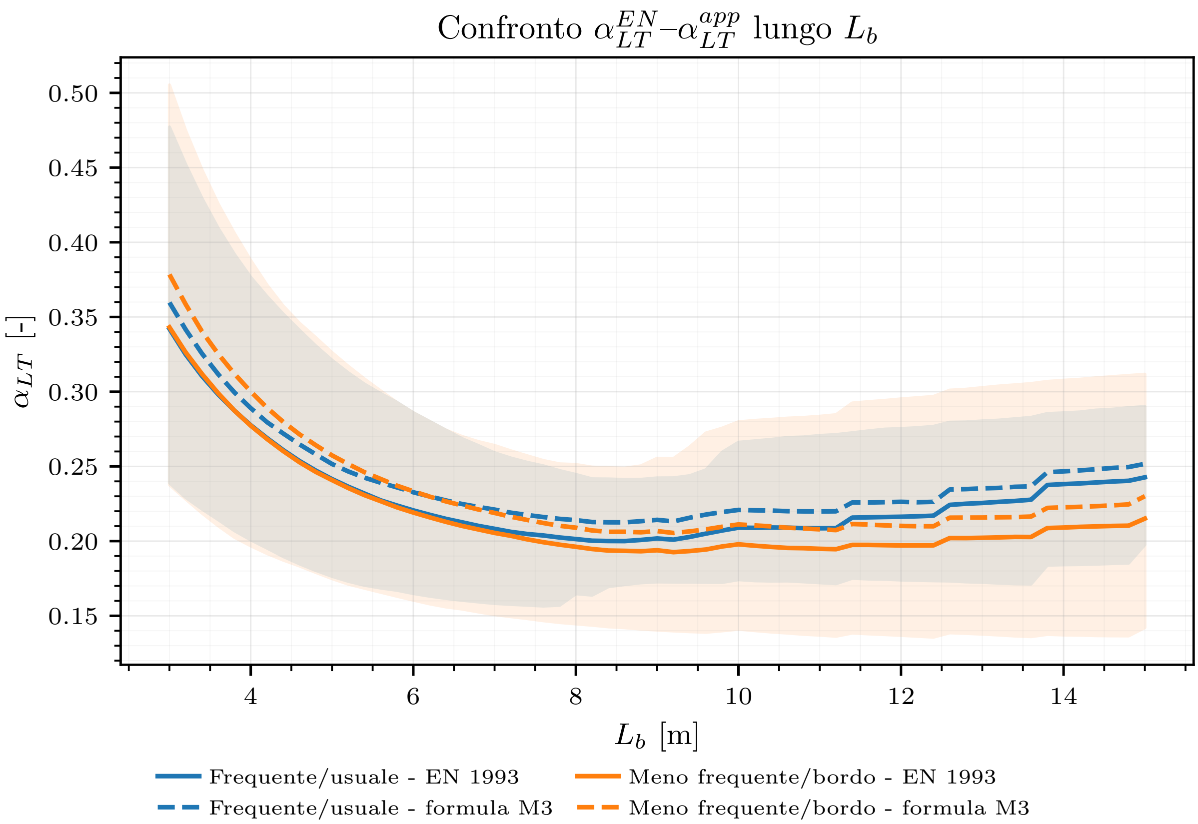

$$\widehat{\alpha}_{LT} = \frac{A_c^2}{M_{y,Rk} L_b} k_L B_s C_f k_f k_C k_n k_\tau k_D$$

$$\ln k_L = c_1 x_L + c_2 x_L^2, \quad \ln k_\tau = b_0 + b_q q_\tau + b_u u_\tau + b_{q2} q_\tau^2 + b_{qu} q_\tau u_\tau$$

Figure 9. *Quantiles of α_{LT}^{EN} and $\widehat{\alpha}_{LT}$ over the 61 values of L_b.*

the resulting actions are resisted by the steelwork alone. For each main girder, the tributary width given in the table is considered; the local working-area load is applied over a loaded length of 3.00 m, centred at midspan. The characteristic line load due to fresh concrete is:

$$\begin{aligned} Q_{cf} &= \gamma_c s_c b_{\text{trib}} \\ &= 26.00\,\text{kN/m}^3 \cdot 0.25\,\text{m} \cdot 5.00\,\text{m} \\ &= 32.50\,\text{kN/m}. \end{aligned}$$

The characteristic line load due to formwork and supporting elements is:

$$\begin{aligned} Q_{cc} &= q_{cc} b_{\text{trib}} \\ &= 2.00\,\text{kN/m}^2 \cdot 5.00\,\text{m} = 10.00\,\text{kN/m}. \end{aligned}$$

The uniformly distributed component of the transient ULS combination is:

$$\begin{aligned} q_{Ed} &= \gamma_G G_{st} + \gamma_Q \left(Q_{cf} + Q_{cc}\right) \\ &= 76.70\,\text{kN/m}. \end{aligned}$$

For the working area, the loaded width assigned to one girder is $b_{Qca} = 3.00\,\text{m}$; the corresponding design line load is:

$$\begin{aligned} q_{Qca,Ed} &= \gamma_Q q_{ca} b_{Qca} \\ &= 1.50 \cdot 1.50\,\text{kN/m}^2 \cdot 3.00\,\text{m} = 6.75\,\text{kN/m}. \end{aligned}$$

Since the loaded length $l_{Qca} = 3.00\,\text{m}$ is centred at midspan, its contribution to the maximum moment is:

$$\begin{aligned} M_{Qca} &= q_{Qca,Ed} l_{Qca} \left(\frac{L}{4} - \frac{l_{Qca}}{8}\right) \\ &= 6.75\,\text{kN/m} \cdot 3.00\,\text{m} \left(\frac{48.00\,\text{m}}{4} - \frac{3.00\,\text{m}}{8}\right) \\ &= 235.41\,\text{kNm}. \end{aligned}$$

The moment due to the uniformly distributed component is:

$$\begin{aligned} M_{q,Ed} &= \frac{q_{Ed} L^2}{8} \\ &= \frac{76.70\,\text{kN/m} \cdot (48.00\,\text{m})^2}{8} \\ &= 22089.59\,\text{kNm}. \end{aligned}$$

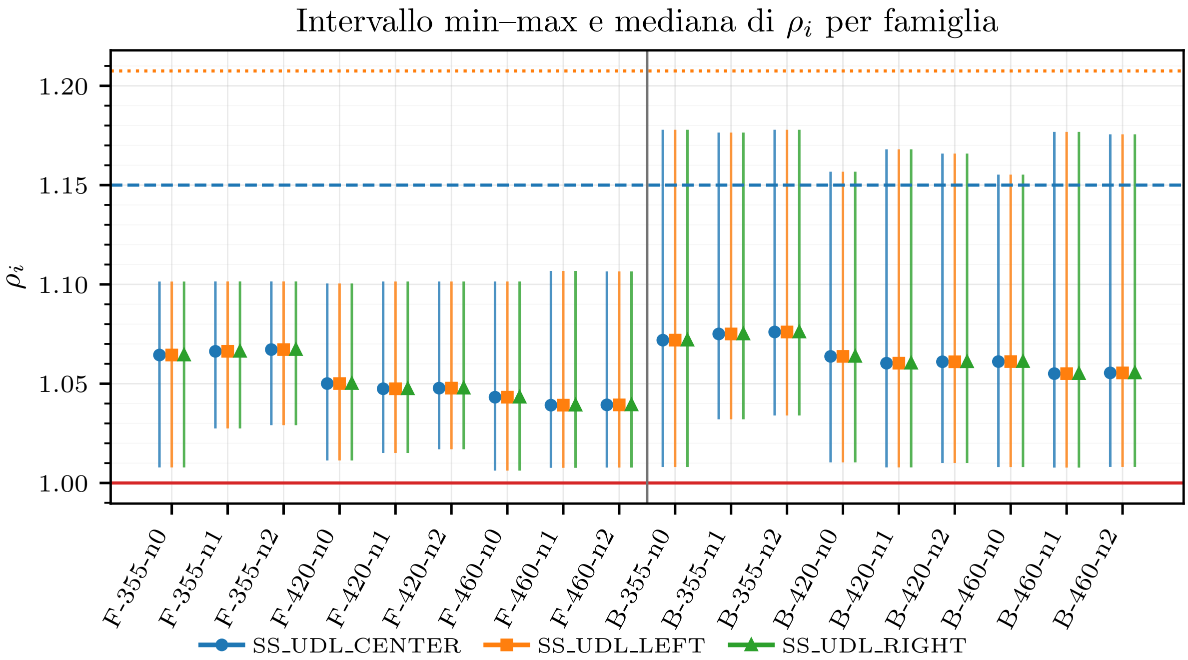

$$\rho_i = \widehat{\alpha}_{LT,i}/\alpha^{EN}_{LT,i}$$
$$\rho_{\max,F} = 1.150, \qquad \rho_{\max,B} = 1.150\,k_B = 1.2075$$

Figure 10. *Minimum, median and maximum values of the ratio ρ, grouped by domain, steel grade, stiffener configuration and load identifier.*

The maximum design moment during casting is therefore:

$$\begin{aligned} M_{Ed} &= M_{q,Ed} + M_{Qca} \\ &= 22089.59\,\mathrm{kNm} + 235.41\,\mathrm{kNm} \\ &= \boxed{22325.00\,\mathrm{kNm}}. \end{aligned}$$

To ensure a consistent comparison between analytical formulations and numerical models, the same maximum moment may be reproduced by the equivalent fictitious uniformly distributed load:

$$\begin{aligned} p^* &= \frac{8M_{Ed}}{L^2} \\ &= \frac{8 \cdot 22325.00\,\mathrm{kNm}}{(48.00\,\mathrm{m})^2} \\ &= 77.52\,\mathrm{kN/m}. \end{aligned}$$

The example compares the complete EN 1993 procedure and the REV3 approximate procedure based on the design charts for the same P1 section. Consistent with the package calibration, $\gamma_{M1} = 1.10$ is adopted. The design moment used for comparison is $M_{Ed} = 22325.00\,\mathrm{kNm}$.

6.2. Complete calculation according to EN 1993

The P1 section has two levels of longitudinal stiffeners, each formed by a pair of plates symmetrically arranged on both sides of the web at levels $h_w/3$ and $2h_w/3$ above the lower edge of the web. The girder is made of S355 steel, for which $f_y = 335\,\mathrm{MPa}$, $E = 210000\,\mathrm{MPa}$, $\nu = 0.30$ and $G = E/[2(1+\nu)] \approx 81000\,\mathrm{MPa}$ are adopted.

The P1 configuration was not used to estimate the model coefficients, construct the design charts or locally realign the approximate procedure. It therefore constitutes an independent application case used to assess the ability of the proposed method to generalise to a geometry not directly involved in its development, thereby avoiding a circular comparison with calibration data.

When defining lateral-torsional slenderness through the elastic critical moment M_{cr}, EN 1993-1-1 requires the latter to account for the gross cross-sectional properties, actual restraint conditions, bending-moment distribution and load application position. The standard does not, however, provide a general closed-form expression for longitudinally stiffened sections with arbitrary layouts or arrangements that are asymmetric with respect to the web plane.

For stiffeners fitted on one side only, geometries producing flexural–torsional coupling that cannot be represented by an equivalent monosymmetric section, or cases involving significant cross-sectional distortion, M_{cr} should therefore be determined by an elastic eigenvalue analysis or a specifically validated numerical model.

For P1, by contrast, the stiffeners are arranged symmetrically with respect to the web plane and can be

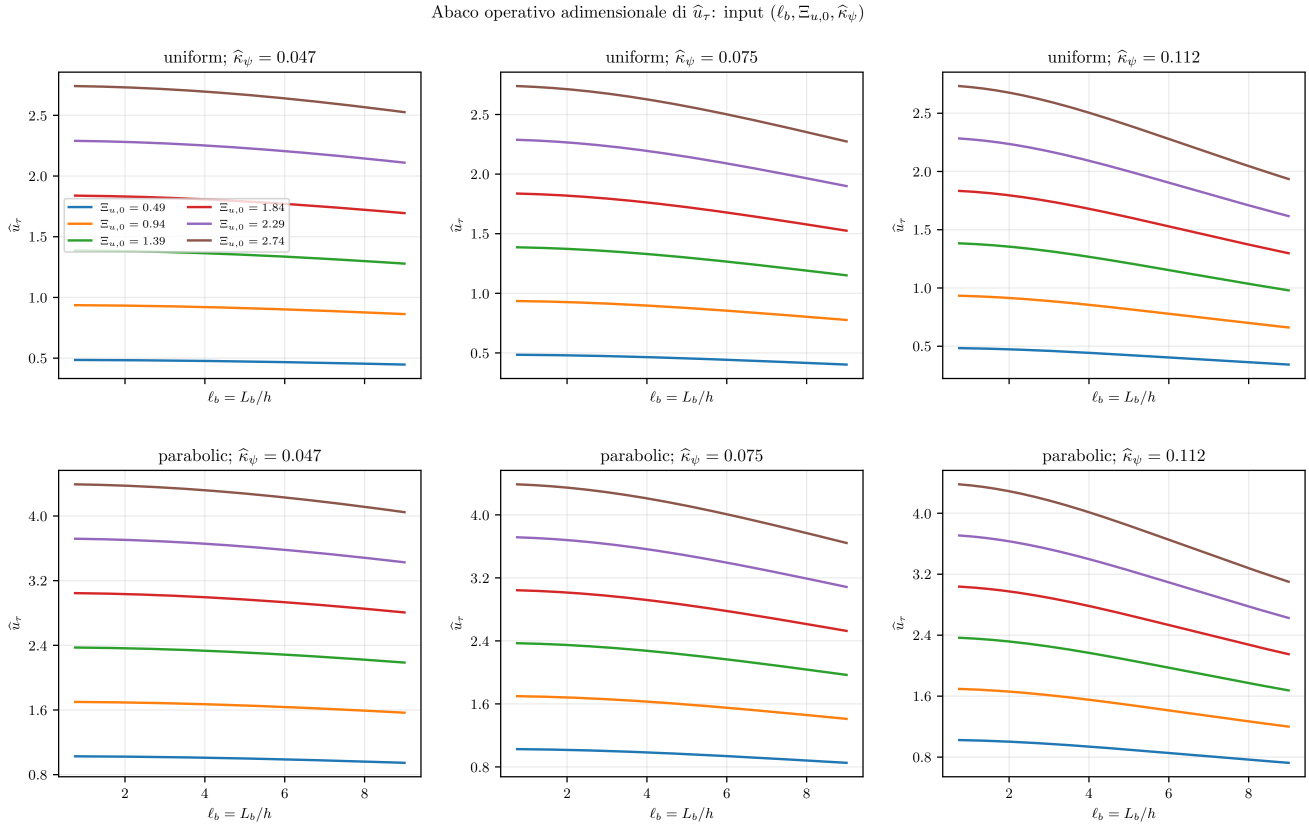

Figure 11. *Operational dimensionless chart for* $\widehat{u}_\tau$.

included in the gross-section elastic properties without introducing additional lateral asymmetry.

Monosymmetry about the plane of bending nevertheless remains because the upper and lower flanges have different dimensions. This requires evaluation of the shear centre, the warping constant and the monosymmetry parameter z_j.

For historical context, an explicit formulation of the elastic critical moment for symmetric and monosymmetric open sections was provided in ENV 1993-1-1:1992, Appendix F.[5] Tables F.1.1 and F.1.2 of the same appendix also provided the coefficients C_1, C_2 and C_3 associated with restraint conditions and the principal bending-moment diagrams.

These expressions remain useful analytical references, but their use should not be extended automatically to asymmetric stiffened configurations outside the assumptions of the model.

Before applying the simplified method, the characteristic geometric ratios of the section are compared with the ranges covered by the parametric campaign to establish its position within the validity domain and identify any conditions close to its boundaries.

The complete EN 1993 calculation is taken as the reference and considers the properties of the section strengthened by longitudinal stiffeners (and, naturally, by transverse stiffeners, which are not considered in this specific treatment), its classification and, where required, the corresponding effective properties. The geometric and mechanical data of the section are:

$$\begin{aligned} b_c &= 550\,\text{mm}, & t_c &= 35\,\text{mm}, \\ b_t &= 650\,\text{mm}, & t_t &= 68\,\text{mm}, \\ h_w &= 2702\,\text{mm}, & t_w &= 12\,\text{mm}, \\ b_s &= 150\,\text{mm}, & t_s &= 10\,\text{mm}. \end{aligned} \tag{30}$$

where b_s and t_s are the width and thickness, respectively, of an individual stiffener plate. At each level, two identical plates are arranged symmetrically on both sides of the web; therefore, the total stiffener area at each level is $2b_st_s$, while the total area of the four plates at the two levels is $4b_st_s$.

From the geometry in Eq. (30), the overall depth and gross area are:

$$\begin{aligned} h &= t_t + h_w + t_c = 2805.00\,\text{mm}, \\ A &= b_tt_t + t_wh_w + b_ct_c + 4b_st_s = 101874.00\,\text{mm}^2. \end{aligned} \tag{31}$$

[5] ENV 1993-1-1:1992 was issued as an experimental European prestandard and was formally superseded by EN 1993-1-1:2005, approved by CEN on 16 April 2004 and published in May 2005. In Italy, UNI EN 1993-1-1:2005, ratified on 19 July 2005 and published in August 2005, together with UNI EN 1993-1-8:2005, UNI EN 1993-1-9:2005 and UNI EN 1993-1-10:2005, replaced UNI ENV 1993-1-1:2004.

The foreword to the EN also set November 2005 as the deadline for national implementation and March 2010 as the final deadline for withdrawal of conflicting national standards. Accordingly, the reference to Appendix F of the ENV in this paper is solely historical and informative.

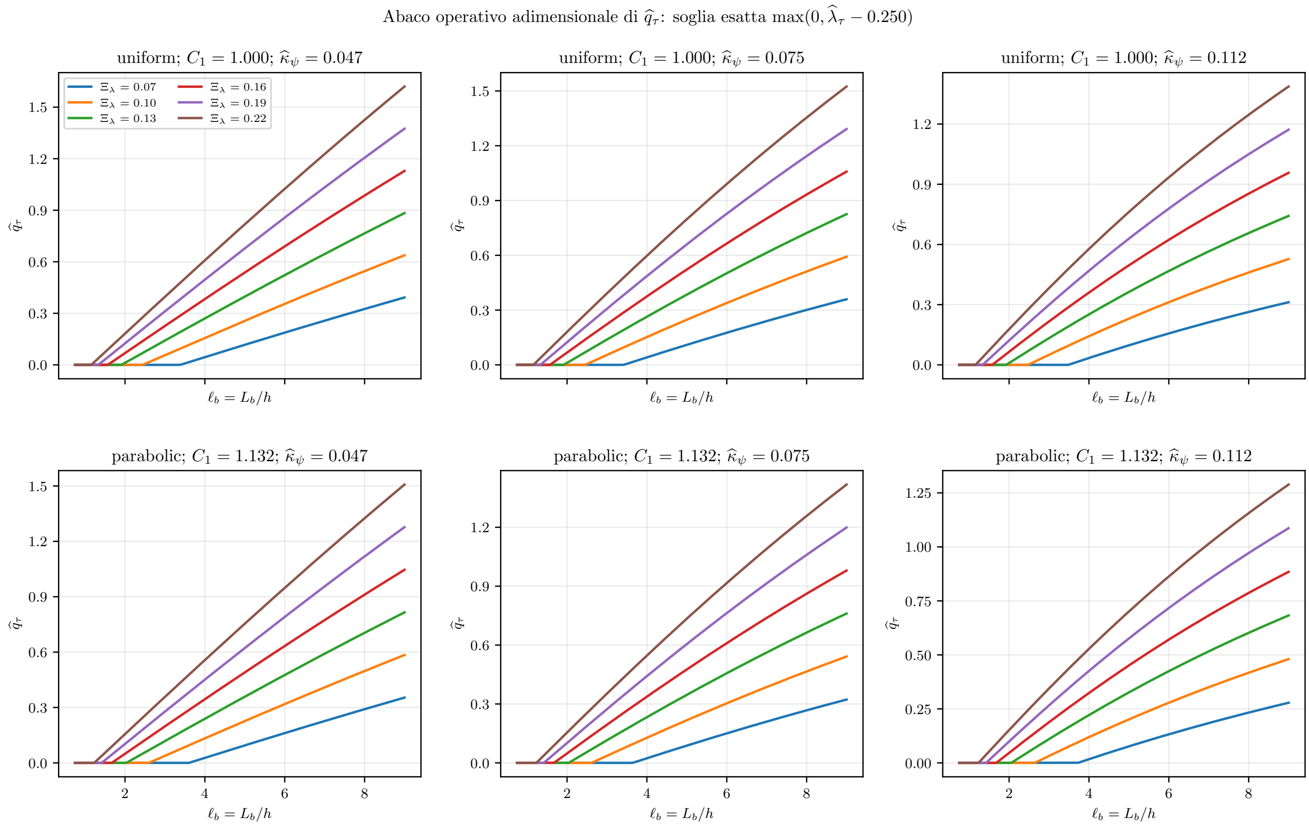

Figure 12. *Operational dimensionless chart for $\widehat{q}_\tau$, with the exact threshold at $\widehat{\lambda}_\tau = 0.250$.*

The centroid and the second moment of area about the major axis, evaluated from the rectangular decomposition, are:

$$\begin{aligned} y_G &= \frac{\sum_i A_i y_i}{\sum_i A_i} = 1076.681\,\text{mm}, \\ I_y &= \sum_i \left[I_{y,i}^{(0)} + A_i (y_i - y_G)^2 \right] \\ &= 1.299 \times 10^{11}\,\text{mm}^4. \end{aligned} \tag{32}$$

The minor-axis second moment of area is:

$$\begin{aligned} I_z &= \sum_i I_{z,i}^{(0)} \\ &= 2.092 \times 10^{9}\,\text{mm}^4. \end{aligned} \tag{33}$$

The calculation of I_z includes the contributions of the two flanges, the web and the four longitudinal stiffener plates. For each stiffener, both the centroidal second moment of area and the parallel-axis term relative to the global minor z–z axis are included, accounting for the symmetric arrangement on both sides of the web. The web contribution is practically negligible, approximately 0.019% of I_z; the value of I_z is therefore governed by the flanges, with a secondary contribution from the four longitudinal stiffeners.

The torsion constant of each rectangle was calculated using the CTICM–Villette formulation:[6]

$$\begin{aligned} d_{\text{max}} &= \max(d_1, d_2), \\ d_{\text{min}} &= \min(d_1, d_2), \\ \rho &= \frac{d_{\text{min}}}{d_{\text{max}}} \le 1, \\ \kappa_V(\rho) &= 1 - \rho\left(0.633 - 0.055\rho^3\right), \\ I_{t,V}(d_1, d_2) &= \frac{d_{\text{max}} d_{\text{min}}^3}{3}\, \kappa_V(\rho) \\ &= \frac{d_{\text{max}} d_{\text{min}}^3}{3} \\ &\quad \times \left[1 - \rho\left(0.633 - 0.055\rho^3\right)\right] \\ &= \frac{d_{\text{max}} d_{\text{min}}^3}{3} \left[1 - \frac{d_{\text{min}}}{d_{\text{max}}}\left(0.633 - 0.055\frac{d_{\text{min}}^3}{d_{\text{max}}^3}\right)\right], \\ \lim_{\rho\to 0} \kappa_V(\rho) &= 1, \\ \lim_{\rho\to 0} I_{t,V} &= \frac{d_{\text{max}} d_{\text{min}}^3}{3}. \end{aligned}$$

Summing the contributions of the web, the flanges and

[6]The CTICM–Villette formulation provides a closed-form approximation of the Saint-Venant torsion constant of a solid rectangle, correcting the limiting value $bt^3/3$ as a function of the ratio t/b, with $b \ge t$. It assumes a prismatic, homogeneous and isotropic member under linear-elastic uniform torsion; it does not include warping restraint or local effects associated with welds, fillets or geometric discontinuities.

Quantity	Symbol	Value	Definition
Girder span	L	$48.00\,\mathrm{m}$	Simply supported scheme
Distance between torsional restraints	L_b	$4.80\,\mathrm{m}$	Spacing of the girder torsional restraints
Tributary width	b_{trib}	$5.00\,\mathrm{m}$	Tributary width assigned to one girder
Slab thickness	s_c	$0.25\,\mathrm{m}$	Non-composite fresh concrete
Unit weight of fresh concrete	γ_c	$26.00\,\mathrm{kN/m^3}$	Value adopted during casting
Formwork surface load	q_{cc}	$2.00\,\mathrm{kN/m^2}$	Formwork and supporting elements
Steelwork self-weight	G_{st}	$9.59\,\mathrm{kN/m}$	Characteristic value for one girder
Local working area	A_{Qca}	$3.00\,\mathrm{m} \times 3.00\,\mathrm{m}$	Area centred at midspan
Working-area load	q_{ca}	$1.50\,\mathrm{kN/m^2}$	Variable construction action
Permanent-action factor	γ_G	1.35	Transient ULS combination
Variable-action factor	γ_Q	1.50	Transient ULS combination

Table 3. *Data adopted for the load analysis during slab casting.*

the two pairs of longitudinal stiffeners gives:

$$\begin{aligned} I_t &= I_{t,V}(h,t_w) + I_{t,V}(b_c,t_c) - \left(\frac{t_w}{b_c}\right)^2 I_{t,V}(t_w,t_c) \\ &+ I_{t,V}(b_t,t_t) - \left(\frac{t_w}{b_t}\right)^2 I_{t,V}(t_w,t_t) \\ &+ 2I_{t,V}(2b_s+t_w,t_s) - 2\left(\frac{t_w}{2b_s+t_w}\right)^2 I_{t,V}(t_w,t_s) \\ &= 7.297\times10^7\,\mathrm{mm}^4. \end{aligned} \tag{34}$$

For warping, the levels of the two flanges and of the two stiffener pairs are considered. The shear centre is obtained as the weighted average using the minor-axis second moments of area of the levels:

$$y_S = \frac{\sum_r I_{z,r} y_r}{\sum_r I_{z,r}} = 706.18\,\mathrm{mm}. \tag{35}$$

The warping constant is therefore:

$$I_w = \sum_r I_{z,r}(y_r - y_S)^2 = 2.841\times10^{15}\,\mathrm{mm}^6. \tag{36}$$

Taking the z-axis as positive towards the upper compression flange, the shear-centre coordinate relative to the centroid is (see Fig. 1 on page 4):

$$z_s = y_S - y_G = -370.50\,\mathrm{mm}. \tag{37}$$

The Wagner integral and the monosymmetry parameter are:

$$\begin{aligned} J_{\mathrm{int}} &= \int_A z(y^2+z^2)\,\mathrm{d}A = 6.85\times10^{13}\,\mathrm{mm}^5, \\ z_j &= z_s - \frac{J_{\mathrm{int}}}{2I_y} = -634.31\,\mathrm{mm}. \end{aligned} \tag{38}$$

Because the load is implicitly assumed to act on the top surface of the compression flange, its level relative to the shear centre is:

$$z_g = h - y_S = 2098.82\,\mathrm{mm} > 0. \tag{39}$$

The cross-section is Class 4. For $f_y = 335\,\mathrm{MPa}$:

$$\varepsilon = \sqrt{\frac{235}{f_y}} = 0.838. \tag{40}$$

The EN 1993-1-5 effective-section iteration converges to:

$$\begin{aligned} A_{\mathrm{eff}} &= 94527.42\,\mathrm{mm}^2, \\ y_{G,\mathrm{eff}} &= 1008.16\,\mathrm{mm}, \\ I_{y,\mathrm{eff}} &= 1.22\times10^{11}\,\mathrm{mm}^4, \\ W_{y,\mathrm{eff}} &= \frac{I_{y,\mathrm{eff}}}{h - y_{G,\mathrm{eff}}} = 67955139.14\,\mathrm{mm}^3. \end{aligned} \tag{41}$$

The characteristic bending resistance moment of the effective section is:

$$M_{y,Rk} = W_{y,\mathrm{eff}} f_y = 22764.97\,\mathrm{kNm}. \tag{42}$$

For $L = 48.00\,\mathrm{m}$ and $L_b = 4.80\,\mathrm{m}$, $L_b/L = 0.100 < 0.250$. Equation (8) and Fig. 2 give:

$$C_1 = 1.000, \qquad C_2 = 0.000, \qquad C_3 = 1.000. \tag{43}$$

With $k_z = k_w = 1.000$, the geometric term and the factor g are:

$$\begin{aligned} \Delta &= C_2 z_g - C_3 z_j = 634.31\,\mathrm{mm}, \\ g &= \sqrt{1 - \frac{I_z}{I_y}} = 0.992. \end{aligned} \tag{44}$$

Adopting $E = 210000\,\mathrm{MPa}$, $\nu = 0.300$ and $G = E/[2(1+\nu)] \approx 81000\,\mathrm{MPa}$, the contributions under the square root in Eq. (7) are:

$$\begin{aligned} \frac{I_w}{I_z} &= 1357825.83\,\mathrm{mm}^2, \\ \frac{L_b^2 G I_t}{\pi^2 E I_z} &= 31312.81\,\mathrm{mm}^2, \\ \mathcal{S}_{cr} &= \frac{I_w}{I_z} + \frac{L_b^2 G I_t}{\pi^2 E I_z} = 1389138.64\,\mathrm{mm}^2. \end{aligned} \tag{45}$$

Therefore:

$$\begin{aligned} \sqrt{\mathcal{S}_{cr} + \Delta^2} - \Delta &= 704.15\,\mathrm{mm}, \\ C_1 \frac{\pi^2 E I_z}{L_b^2 g} &= 189.77\,\mathrm{kNm/mm}, \\ M_{cr} &= C_1 \frac{\pi^2 E I_z}{L_b^2 g}\left(\sqrt{\mathcal{S}_{cr}+\Delta^2} - \Delta\right) \\ &= 133626.09\,\mathrm{kNm}. \end{aligned} \tag{46}$$

The elastic critical multiplier relative to the applied moment and the lateral-torsional slenderness are:

$$\lambda_{cr}^{(\mathrm{EC3})} = \frac{M_{cr}}{M_{Ed}} = 5.985, \tag{47}$$

$$\overline{\lambda}_{LT} = \sqrt{\frac{M_{y,Rk}}{M_{cr}}} = 0.413. \tag{48}$$

For the welded section, with $h/b_t = 4.315 > 2.000$, buckling curve d is adopted and hence $\alpha_{LT} = 0.760$. The general method of EN 1993-1-1, Sec. 6.3.2.2, gives:

$$\begin{aligned} \Phi_{LT} &= \frac{1}{2}\left[1 + \alpha_{LT}(\overline{\lambda}_{LT} - 0.200) + \overline{\lambda}_{LT}^2\right] = 0.666, \\ \chi_{LT} &= \min\left\{1, \frac{1}{\Phi_{LT} + \sqrt{\Phi_{LT}^2 - \overline{\lambda}_{LT}^2}}\right\} = 0.841. \end{aligned} \tag{49}$$

With the partial factor adopted in the REV3 release, $\gamma_{M1} = 1.10$, the design resistance is:

$$M_{b,Rd}^{EC3} = \chi_{LT}\frac{M_{y,Rk}}{\gamma_{M1}} = 17409.55\,\mathrm{kNm}. \tag{50}$$

The utilisation ratio is:

$$\eta_{EC3} = \frac{M_{Ed}}{M_{b,Rd}^{EC3}} = 1.282 > 1.000 \text{ (not verified)}. \tag{51}$$

The reference parameter, using the unit convention of the approximate parametric procedure, is:

$$\begin{aligned} A_c &= b_c t_c = 19250.00\,\mathrm{mm}^2, \\ \alpha_{LT}^{EC3} &= \frac{A_c^2}{M_{b,Rd}^{EC3} L_b} = 0.443. \end{aligned} \tag{52}$$

with $M_{b,Rd}^{EC3}$ expressed in $\mathrm{kN\,cm}$ and L_b in centimetres.

6.3. Calculation using the approximate parametric procedure and design charts

The graphical procedure does not use the torsional properties in Eqs. (33)–(39) and does not require calculation of M_{cr}, $\overline{\lambda}_{LT}$ or χ_{LT}. Only nominal dimensionless ratios are used for the torsional block.

The final resistance still requires A_c and $M_{y,Rk} = W_y f_y$, which are already available from the cross-section classification. From the data in Eq. (30):

$$\begin{aligned} &\frac{h}{b_c} = 5.100, && \frac{h_w}{t_w} = 225.167, \\ &\frac{b_t}{b_c} = 1.182, && \frac{t_t}{t_c} = 1.943, \\ &\frac{t_c}{h} = 0.0125, && \ell_b = \frac{L_b}{h} = 1.711, \\ r_L = &\frac{L_b}{L} = 0.100, && \frac{b_s}{h} = 0.0535, \\ &\frac{t_s}{h} = 0.0036. \end{aligned} \tag{53}$$

The ratios in Eq. (53) lie within the declared support of the design charts. The section belongs to the "less frequent/boundary" domain, mainly because $h/b_c = 5.100$, $h_w/t_w = 225.17$, and $b_t/b_c = 1.18$. From $r_L = 0.100$, Eq. (8) and Fig. 2 select the uniform branch of Eq. (43). For P1, the components of the dimensionless vector in Eq. (25) are (rounded to three decimal places):

$$\begin{aligned} \ln\beta_c &= -1.629, & \ln\tau_c &= -4.382, \\ \ln\beta_t &= -1.462, & \ln\tau_t &= -3.718, \\ \ln\tau_w &= -5.452, & \ln\gamma_A &= 0.831, \\ \ln(h/b_c) &= 1.629, & \ln(h_w/t_w) &= 5.417, \\ \ln(b_t/b_c) &= 0.167, & \ln(t_t/t_c) &= 0.664, \\ \ln(b_s/h) &= -2.928, & \ln(t_s/h) &= -5.627, \\ \ln(f_y/E) &= -6.438. \end{aligned} \tag{54}$$

6.4. Tables for estimating $\widehat{\kappa}_\psi$ and $\Xi_{u,0}$

For each variable, the contribution at points between the five tabulated values is obtained by linear interpolation. For the configuration $n_{\mathrm{long}} = n$:

$$\begin{aligned} \widehat{\kappa}_\psi &= \exp\left(b_\psi^{(n)} + \frac{\sum_j P_{\psi,j}}{100}\right), \\ \Xi_{u,0}^{(C)} &= \exp\left(b_{u,C}^{(n)} + \frac{\sum_j P_{u,C,j}}{100}\right). \end{aligned}$$

Branch C is selected according to the bending-moment distribution over the unrestrained segment L_b: uniform for $C_1 = 1.000$ and parabolic for $C_1 = 1.132$. Only nominal dimensionless ratios are required.

Table 4. *Tabulated contributions for the manual calculation of $\widehat{\kappa}_\psi$ and $\Xi_{u,0}$, distinguished by the number $n = n_{\mathrm{long}}$ of longitudinal-stiffener levels.*

Variable	Input values	P_ψ	$P_{u,U}$	$P_{u,P}$
$n_{\mathrm{long}} = 0$: $b_\psi = -2.610008$, $b_{u,U} = 0.365980$, $b_{u,P} = 0.881069$				
t_c/h	0.00375; 0.00720; 0.00900; 0.01059; 0.01491	-66.4; -13.3; 3.9; 16.2; 42.4	-2.9; -0.5; 0.2; 0.6; 2.0	-1.1; -0.2; 0.0; 0.3; 0.9
h_w/t_w	100.0; 123.3; 150.8; 194.1; 300.0	3.4; 3.0; 1.3; -2.2; -12.4	-1.5; -0.8; -0.2; 0.7; 2.3	-0.4; -0.3; -0.1; 0.2; 0.7
t_w/t_c	0.24300; 0.68000; 0.76000; 0.86140; 1.438	25.8; 0.2; -1.9; -3.3; -10.2	0.0; 0.0; 0.0; 0.0; 0.0	0.0; 0.0; 0.0; 0.0; 0.0
t_t/t_c	1.600; 1.922; 2.244; 2.600; 3.000	-28.9; -12.4; 0.7; 14.2; 28.0	-9.9; -4.7; -0.1; 4.9; 10.3	-9.1; -4.1; 0.1; 4.4; 8.6
$\gamma_A = A_t/A_c$	1.896; 3.436; 4.016; 4.787; 7.601	-20.3; -5.8; -0.8; 5.3; 25.4	-33.6; -2.3; 1.5; 4.7; 13.2	-21.3; -3.2; 0.5; 4.4; 14.7

Table 4 – continued.

Variable	Input values	P_ψ	$P_{u,U}$	$P_{u,P}$
$n_{\text{long}} = 0$ – *continued*				
h/b_c	3.512; 3.948; 4.312; 4.801; 5.200	-22.4; -9.8; -0.0; 9.6; 17.4	-0.1; -0.0; 0.0; 0.0; 0.0	-0.2; -0.0; 0.0; 0.0; 0.0
A_c/h^2	0.00080; 0.00166; 0.00204; 0.00241; 0.00406	15.8; 1.5; -0.6; -1.9; -7.9	0.0; 0.0; 0.0; 0.0; 0.0	0.0; 0.0; 0.0; 0.0; 0.0
A_w/h^2	0.00318; 0.00489; 0.00627; 0.00761; 0.00949	-10.0; -4.8; -0.3; 4.9; 11.7	0.0; 0.0; 0.0; 0.0; 0.0	0.0; 0.0; 0.0; 0.0; 0.0
b_t/b_c	1.100; 1.529; 1.807; 2.140; 2.600	0.0; 0.0; 0.0; 0.0; 0.0	-88.8; -23.0; 2.8; 26.7; 54.0	-69.8; -21.3; 1.3; 23.6; 49.0

Table 4 – continued.

Variable	Input values	P_ψ	$P_{u,U}$	$P_{u,P}$
$n_{\text{long}} = 1$: $b_\psi = -2.609970$, $b_{u,U} = 0.361674$, $b_{u,P} = 0.878843$				
t_c/h	0.00375; 0.00720; 0.00900; 0.01059; 0.01491	-66.0; -13.4; 3.9; 16.3; 42.5	-2.3; -0.5; 0.2; 0.5; 1.3	-0.9; -0.2; 0.1; 0.2; 0.5
h_w/t_w	100.0; 123.3; 150.8; 194.1; 300.0	3.4; 3.0; 1.2; -2.1; -12.6	-1.2; -0.6; -0.2; 0.6; 2.0	-0.5; -0.2; -0.1; 0.2; 0.6
t_w/t_c	0.24300; 0.68000; 0.76000; 0.86140; 1.438	25.8; 0.3; -1.8; -3.2; -10.6	0.0; 0.0; 0.0; 0.0; 0.0	0.0; 0.0; 0.0; 0.0; 0.0
t_t/t_c	1.600; 1.922; 2.244; 2.600; 3.000	-28.9; -12.2; 0.8; 14.2; 28.0	-10.0; -4.9; -0.5; 5.2; 10.7	-9.1; -4.1; -0.1; 4.5; 8.8
$\gamma_A = A_t/A_c$	1.896; 3.436; 4.016; 4.787; 7.601	-19.9; -5.7; -0.8; 5.3; 25.4	-34.2; -2.1; 1.5; 4.8; 12.9	-21.2; -3.0; 0.6; 4.5; 14.5

Table 4 – continued.

Variable	Input values	P_ψ	$P_{u,U}$	$P_{u,P}$
$n_{\text{long}} = 1$ – *continued*				
h/b_c	3.512; 3.948; 4.312; 4.801; 5.200	-22.4; -9.7; 0.0; 9.5; 17.1	-1.0; -0.1; 0.0; 0.0; 0.3	-0.8; -0.0; 0.0; 0.0; 0.1
A_c/h^2	0.00080; 0.00166; 0.00204; 0.00241; 0.00406	15.8; 1.4; -0.6; -1.8; -7.6	0.0; 0.0; 0.0; 0.0; 0.0	0.0; 0.0; 0.0; 0.0; 0.0
A_w/h^2	0.00318; 0.00489; 0.00627; 0.00761; 0.00949	-9.6; -4.7; -0.4; 4.8; 11.4	0.0; 0.0; 0.0; 0.0; 0.0	0.0; 0.0; 0.0; 0.0; 0.0
b_t/b_c	1.100; 1.529; 1.807; 2.140; 2.600	0.0; 0.0; 0.0; 0.0; 0.0	-89.7; -23.2; 2.7; 26.8; 53.9	-69.9; -21.3; 1.3; 23.6; 48.9

Table 4 – continued.

Variable	Input values	P_ψ	$P_{u,U}$	$P_{u,P}$
$n_{\text{long}} = 2$: $b_\psi = -2.609007$, $b_{u,U} = 0.361353$, $b_{u,P} = 0.878716$				
t_c/h	0.00375; 0.00720; 0.00900; 0.01059; 0.01491	-66.1; -13.3; 3.9; 16.3; 42.6	-2.1; -0.4; 0.2; 0.4; 1.1	-0.8; -0.2; 0.1; 0.2; 0.4
h_w/t_w	100.0; 123.3; 150.8; 194.1; 300.0	3.4; 3.0; 1.2; -2.2; -12.6	-1.2; -0.6; -0.2; 0.5; 1.9	-0.5; -0.2; -0.1; 0.1; 0.6
t_w/t_c	0.24300; 0.68000; 0.76000; 0.86140; 1.438	25.6; 0.3; -1.8; -3.1; -10.6	0.0; 0.0; 0.0; 0.0; 0.0	0.0; 0.0; 0.0; 0.0; 0.0
t_t/t_c	1.600; 1.922; 2.244; 2.600; 3.000	-28.8; -12.2; 0.7; 14.2; 28.0	-9.9; -4.9; -0.5; 5.2; 10.7	-9.0; -4.1; -0.2; 4.5; 8.8
$\gamma_A = A_t/A_c$	1.896; 3.436; 4.016; 4.787; 7.601	-19.7; -5.7; -0.8; 5.3; 25.4	-33.7; -2.0; 1.5; 4.8; 13.0	-20.9; -3.0; 0.6; 4.5; 14.6

Table 4 – continued.

Variable	Input values	P_ψ	$P_{u,U}$	$P_{u,P}$
$n_{\text{long}} = 2$ – *continued*				
h/b_c	3.512; 3.948; 4.312; 4.801; 5.200	-22.1; -9.6; 0.1; 9.5; 17.1	-1.1; -0.1; 0.1; 0.1; 0.3	-0.9; -0.0; 0.0; 0.0; 0.1
A_c/h^2	0.00080; 0.00166; 0.00204; 0.00241; 0.00406	15.9; 1.4; -0.5; -1.8; -7.5	0.0; 0.0; 0.0; 0.0; 0.0	0.0; 0.0; 0.0; 0.0; 0.0
A_w/h^2	0.00318; 0.00489; 0.00627; 0.00761; 0.00949	-9.6; -4.7; -0.4; 4.8; 11.3	0.0; 0.0; 0.0; 0.0; 0.0	0.0; 0.0; 0.0; 0.0; 0.0
b_t/b_c	1.100; 1.529; 1.807; 2.140; 2.600	0.0; 0.0; 0.0; 0.0; 0.0	-89.3; -23.2; 2.7; 26.8; 53.7	-69.6; -21.3; 1.3; 23.5; 48.8

6.4.1. *Application to numerical case P1*

For P1, $n_{\text{long}} = 2$ and the uniform branch U are adopted. The dimensionless input quantities required for interpolation are:

$$\frac{t_c}{h} = \frac{35}{2805} = 0.0125,$$
$$\frac{h_w}{t_w} = \frac{2702}{12} = 225.167,$$
$$\frac{t_w}{t_c} = \frac{12}{35} = 0.343,$$
$$\frac{t_t}{t_c} = \frac{68}{35} = 1.943,$$
$$\gamma_A = \frac{A_t}{A_c} = \frac{650 \cdot 68}{550 \cdot 35} = 2.296,$$
$$\frac{h}{b_c} = \frac{2805}{550} = 5.100,$$
$$\frac{A_c}{h^2} = \frac{550 \cdot 35}{2805^2} = 0.0024,$$
$$\frac{A_w}{h^2} = \frac{2702 \cdot 12}{2805^2} = 0.0041,$$
$$\frac{b_t}{b_c} = \frac{650}{550} = 1.182.$$

For a generic quantity x between two tabulated abscissae x_a and x_b, the contribution is obtained by linear interpolation:

$$P(x) = P_a + \frac{x - x_a}{x_b - x_a}\left(P_b - P_a\right).$$

For example, for $t_c/h = 0.0125$, lying between 0.01059 and 0.01491, one obtains:

$$P_{\psi,t_c/h} = 16.3 + \frac{0.0125 - 0.01059}{0.01491 - 0.01059}(42.6 - 16.3)$$
$$= 27.928,$$
$$P_{u,U,t_c/h} = 0.4 + \frac{0.0125 - 0.01059}{0.01491 - 0.01059}(1.1 - 0.4)$$
$$= 0.709.$$

Applying the same interpolation to every row of the $n_{\text{long}} = 2$ block gives the following contributions:

Variable and P1 value	Interval	$P_{\psi,j}$	$P_{u,U,j}$
$t_c/h = 0.0125$	0.01059–0.01491	27.928	0.709
$h_w/t_w = 225.167$	194.1–300.0	-5.251	0.911
$t_w/t_c = 0.343$	0.243–0.680	19.811	0.000
$t_t/t_c = 1.943$	1.922–2.244	-11.359	-4.613
$\gamma_A = 2.296$	1.896–3.436	-16.064	-25.466
$h/b_c = 5.100$	4.801–5.200	15.195	0.250
$A_c/h^2 = 0.0024$	0.00204–0.00241	-1.765	0.000
$A_w/h^2 = 0.0041$	0.00318–0.00489	-6.964	0.000
$b_t/b_c = 1.182$	1.100–1.529	0.000	-76.666

The sums of the contributions are:

$$\sum_j P_{\psi,j} = 27.928 - 5.251 + 19.811 - 11.359 - 16.064$$
$$+ 15.195 - 1.765 - 6.964 = 21.531,$$
$$\sum_j P_{u,U,j} = 0.709 + 0.911 - 4.613 - 25.466$$
$$+ 0.250 - 76.666 = -104.875.$$

With $b_\psi^{(2)} = -2.609007$ and $b_{u,U}^{(2)} = 0.361353$, the final values are:

$$\ln \widehat{\kappa}_\psi = -2.609007 + \frac{21.531}{100} = -2.394,$$
$$\widehat{\kappa}_\psi^{\text{tab}} = \exp(-2.394) = 0.0913,$$
$$\ln \Xi_{u,0} = 0.361353 - \frac{104.875}{100} = -0.687,$$
$$\Xi_{u,0}^{\text{tab}} = \exp(-0.687) = 0.503.$$

6.5. Manual table for Ξ_λ

For each variable, the contribution at points between the five tabulated values is obtained by linear interpolation. For the configuration $n_{\text{long}} = n$:

$$\Xi_\lambda = \exp\left(b_\lambda^{(n)} + \frac{\sum_j P_{\lambda,j}}{100}\right).$$

The table uses only nominal dimensionless ratios and f_y/E; it does not require prior calculation of I_t, I_w, z_j or M_{cr}.

Table 5. *Tabulated contributions for the manual calculation of Ξ_λ, distinguished by the number $n = n_{\text{long}}$ of longitudinal-stiffener levels.*

Variable	Input values	P_λ
$n_{\text{long}} = 0$: $b_\lambda = -2.105917$		
b_t/b_c	1.100; 1.529; 1.807; 2.140; 2.600	36.7; 12.0; -0.2; -13.4; -28.5
h/b_c	3.512; 3.948; 4.312; 4.801; 5.200	-26.5; -12.0; 0.0; 13.3; 23.8
h_w/t_w	100.0; 123.3; 150.8; 194.1; 300.0	17.7; 9.3; 1.4; -8.8; -26.9
t_w/t_c	0.24300; 0.68000; 0.76000; 0.86140; 1.438	24.4; -0.2; -1.6; -2.6; -2.7
b_c/t_c	13.50; 21.30; 26.80; 33.00; 71.80	2.4; 2.4; 1.4; -1.3; -13.7

Table 5 – continued.

Variable	Input values	P_λ
$n_{\text{long}} = 0$ – *continued*		
t_c/h	0.00375; 0.00720; 0.00900; 0.01059; 0.01491	12.0; 2.6; -0.2; -2.6; -14.7
f_y/E	0.00160; 0.00169; 0.00200; 0.00219; 0.00219	-9.8; -5.0; 0.9; 4.0; 4.0
t_t/t_c	1.600; 1.922; 2.244; 2.600; 3.000	8.4; 3.9; -0.1; -3.9; -7.6

Table 5 – continued.

Variable	Input values	P_λ
$n_{\text{long}} = 1$: $b_\lambda = -1.991286$		
b_t/b_c	1.100; 1.529; 1.807; 2.140; 2.600	35.7; 11.6; -0.3; -13.0; -27.6
h/b_c	3.512; 3.948; 4.312; 4.801; 5.200	-27.8; -12.3; -0.2; 13.7; 24.6
h_w/t_w	100.0; 123.3; 150.8; 194.1; 300.0	16.3; 10.0; 2.0; -8.5; -28.5
t_w/t_c	0.24300; 0.68000; 0.76000; 0.86140; 1.438	23.0; -0.3; -1.1; -2.1; -2.1
b_c/t_c	13.50; 21.30; 26.80; 33.00; 71.80	1.3; 1.3; 1.0; -0.7; -9.5

Table 5 – continued.

Variable	Input values	P_λ
$n_{\text{long}} = 1$ – *continued*		
t_c/h	0.00375; 0.00720; 0.00900; 0.01059; 0.01491	15.4; 3.2; -0.3; -3.1; -17.6
f_y/E	0.00160; 0.00169; 0.00200; 0.00219; 0.00219	-9.2; -5.0; 0.9; 4.1; 4.1
t_t/t_c	1.600; 1.922; 2.244; 2.600; 3.000	7.8; 3.5; -0.2; -3.5; -7.0
t_s/h	0.00250; 0.00359; 0.00430; 0.00524; 0.00756	-1.1; -0.9; -0.3; 0.7; 3.0

Table 5 – continued.

Variable	Input values	P_λ
$n_{\text{long}} = 2$: $b_\lambda = -1.987457$		
b_t/b_c	1.100; 1.529; 1.807; 2.140; 2.600	34.9; 11.4; -0.3; -12.7; -26.9
h/b_c	3.512; 3.948; 4.312; 4.801; 5.200	-27.7; -12.2; -0.2; 13.5; 24.4
h_w/t_w	100.0; 123.3; 150.8; 194.1; 300.0	15.9; 9.5; 1.9; -8.1; -27.5
t_w/t_c	0.24300; 0.68000; 0.76000; 0.86140; 1.438	21.7; -0.3; -0.9; -1.9; -1.9
b_c/t_c	13.50; 21.30; 26.80; 33.00; 71.80	1.2; 1.2; 0.9; -0.6; -8.7

Table 5 – continued.

Variable	Input values	P_λ
$n_{\text{long}} = 2$ – *continued*		
t_c/h	0.00375; 0.00720; 0.00900; 0.01059; 0.01491	14.9; 3.2; -0.3; -3.1; -16.4
f_y/E	0.00160; 0.00169; 0.00200; 0.00219; 0.00219	-9.6; -5.1; 0.9; 4.2; 4.2
t_t/t_c	1.600; 1.922; 2.244; 2.600; 3.000	7.2; 3.4; -0.2; -3.3; -6.4
t_s/h	0.00250; 0.00359; 0.00430; 0.00524; 0.00756	-1.1; -0.9; -0.3; 0.6; 2.8

6.5.1. Application to numerical case P1

For P1, the $n_{\text{long}} = 2$ block is used, with $b_\lambda^{(2)} = -1.987457$. The additional quantities required by this table are:

$$\frac{b_c}{t_c} = \frac{550}{35} = 15.714,$$
$$\frac{f_y}{E} = \frac{335}{210000} = 0.0016,$$
$$\frac{t_s}{h} = \frac{10}{2805} = 0.0036.$$

The remaining quantities coincide with those already determined for the preceding table. As an illustrative example, for $b_t/b_c = 1.182$, between 1.100 and 1.529:

$$P_{\lambda,b_t/b_c} = 34.9 + \frac{1.182 - 1.100}{1.529 - 1.100}(11.4 - 34.9) = 30.408.$$

The interpolated contributions for all variables are:

Variable and P1 value	Interval	$P_{\lambda,j}$
$b_t/b_c = 1.182$	1.100–1.529	30.408
$h/b_c = 5.100$	4.801–5.200	21.668
$h_w/t_w = 225.167$	194.1–300.0	-13.791
$t_w/t_c = 0.343$	0.243–0.680	16.666
$b_c/t_c = 15.714$	13.50–21.30	1.200
$t_c/h = 0.0125$	0.01059–0.01491	-8.980
$f_y/E = 0.0016$	0.00160–0.00169	-9.600
$t_t/t_c = 1.943$	1.922–2.244	3.165
$t_s/h = 0.0036$	0.00359–0.00430	-0.892

Therefore:

$$\sum_j P_{\lambda,j} = 30.408 + 21.668 - 13.791 + 16.666 + 1.200 - 8.980 - 9.600 + 3.165 - 0.892 = 39.844,$$
$$\ln \Xi_\lambda = -1.987457 + \frac{39.844}{100} = -1.589,$$
$$\Xi_\lambda^{\text{tab}} = \exp(-1.589) = 0.204.$$

Note. The values $\widehat{\kappa}_\psi^{\text{tab}}$, $\Xi_{u,0}^{\text{tab}}$ and Ξ_λ^{tab} are those obtained from the tabular reduction using linear interpolation between the stated abscissae. They must not be confused with the values obtained directly from the complete polynomial maps, which may differ.

Applying the maps in Eq. (26), with $n_{\text{long}} = 2$ and the uniform branch ($C_1 = 1.000$), gives the three coordinates required to read the charts:

$$\widehat{\kappa}_\psi = 0.0913, \qquad \Xi_{u,0} = 0.503, \qquad \Xi_\lambda = 0.204. \tag{55}$$

For Fig. 11, the upper row corresponding to the uniform branch is used. The value $\widehat{\kappa}_\psi = 0.0913$ lies between the 0.075 and 0.112 panels, while $\Xi_{u,0} = 0.503$ lies between the 0.49 and 0.94 curves. Interpolation at $\ell_b = 1.711$, or application of Eq. (27), gives:

$$\psi_\tau = \widehat{\kappa}_\psi \ell_b = 0.156, \qquad \boxed{\widehat{u}_\tau = 0.497}. \tag{56}$$

Figure 12 again requires the uniform-branch row. The value $\Xi_\lambda = 0.204$ is close to the 0.19 curve; interpolation between the $\widehat{\kappa}_\psi$ panels at $\ell_b = 1.711$, or application of Eq. (28), gives:

$$\widehat{\lambda}_\tau = 0.347, \qquad \boxed{\widehat{q}_\tau = 0.0970}. \tag{57}$$

Equations (56) and (57) show that the torsional block is obtained from the charts without determining I_t, I_w, z_g, z_j or M_{cr}. The exact proxy values, used only for audit purposes, are $u_\tau = 0.496973$ and $q_\tau = 0.096946$.

The basic parameter in Eq. (10) is:

$$\alpha_0 = \frac{A_c^2}{M_{y,Rk} L_b} = \frac{(19250.00)^2}{(22764.97 \cdot 100)(480.00)} = 0.339. \tag{58}$$

Because $x_L = \ln[(L_b/L)/0.10] = 0$, Eq. (11) gives:

$$k_L = 1.0000. \tag{59}$$

The geometric variables in Eq. (12) are:

$$x_h = 0.243, \qquad x_w = 0.224, \qquad x_b = -0.0151, \qquad x_t = -0.0289. \tag{60}$$

With $N_1 = 0$ and $N_2 = 1$, Eq. (14) gives:

$$q_h = 0.309, \qquad q_w = -0.0757, \qquad q_b = -0.309, \qquad q_t = -0.0933. \tag{61}$$

Therefore, from Eq. (15):

$$B_s = 1.0599, \qquad C_f = 1.0074. \tag{62}$$

The direct factors in Eq. (16) are equal to one. Substituting the readings from Eqs. (56) and (57) into the polynomial in Eq. (18) gives:

$$P_\tau = 0.314, \qquad k_\tau = \exp(P_\tau) = 1.369. \tag{63}$$

For the boundary domain, Eq. (20) gives:

$$k_D = 1.0256. \tag{64}$$

The P1 case lies in the cell $n_{\text{long}} = 2$, uniform branch, $1.6 \le \ell_b < 2.2$; the local realignment in Eq. (29) is (or, equivalently, from Table 6):

$$k_A = 1.0335. \tag{65}$$

Substituting the factors in Eqs. (58)–(65) into Eq. (29)

Table 6. *Values of the local realignment coefficient k_A as functions of the domain, model branch, dimensionless length $\ell_b = L_b/h$ and number $n = n_{\text{long}}$ of stiffener configurations considered.*

$\ell_{b,\min}$	$\ell_{b,\max}$	$n=0$	$n=1$	$n=2$
Frequent/usual; uniform branch $C_1 = 1.000$				
0.9	1.2	1.0190	1.0211	1.0205
1.2	1.6	1.0206	1.0221	1.0227
1.6	2.2	1.0243	1.0259	1.0268
2.2	3.0	1.0292	1.0308	1.0322
3.0	4.0	1.0348	1.0363	1.0386
4.0	5.5	1.0373	1.0387	1.0414
Frequent/usual; parabolic branch $C_1 = 1.132$				
4.0	5.5	1.0316	1.0285	1.0323
5.5	7.0	1.0273	1.0302	1.0278
7.0	10.0	1.0306	1.0349	1.0320
Less frequent/boundary; uniform branch $C_1 = 1.000$				
0.0	0.9	1.0188	1.0212	1.0206
0.9	1.2	1.0191	1.0235	1.0232
1.2	1.6	1.0228	1.0280	1.0276
1.6	2.2	1.0283	1.0338	1.0335
2.2	3.0	1.0349	1.0429	1.0411
3.0	4.0	1.0424	1.0535	1.0512
4.0	5.5	1.0468	1.0594	1.0568
Less frequent/boundary; parabolic branch $C_1 = 1.132$				
4.0	5.5	1.0426	1.0575	1.0536
5.5	7.0	1.0490	1.0621	1.0577
7.0	10.0	1.0420	1.0553	1.0493

gives:

$$\begin{aligned}\widehat{\alpha}_{LT}^{\text{abaco}} &= (0.339)(1.0000)(1.0599)(1.0074)\\ &\quad\times (1.369)(1.0256)(1.0335)\\ &= 0.525.\end{aligned} \tag{66}$$

The corresponding equivalent resistance moment and utilisation ratio are:

$$\begin{aligned} M_{b,Rd}^{\text{app,abaco}} &= \frac{A_c^2}{\widehat{\alpha}_{LT}^{\text{abaco}} L_b} = 14704.86\,\text{kNm},\\ \eta_{\text{app,abaco}} &= \frac{M_{Ed}}{M_{b,Rd}^{\text{app,abaco}}} = 1.517 > 1.000.\end{aligned} \tag{67}$$

The graphical prediction is conservative relative to the complete EN 1993 procedure. Using the unrounded value of α_{LT}^{EC3} from Eq. (52) gives:

$$\rho_{P1}^{\text{abaco}} = \frac{\widehat{\alpha}_{LT}^{\text{abaco}}}{\alpha_{LT}^{EC3}} = 1.185 > 1.000. \tag{68}$$

The approximate procedure therefore also fails the verification, in agreement with EN 1993, while providing a lower resistance and a more severe utilisation ratio. The complete comparison is summarised in Table 7.

7. Operational conclusions on the REV3 statistical parametric procedure

The REV3 campaign confirms a conservative formulation for all 1809504 statistical rows. The independent test subset contains no cases with $\rho < 1$ and no exceedances of the limits 1.150 and 1.2075. The dimensionless design charts preserve the conservatism of the complete formula after propagation over all 603168 physical combinations.

The procedure is limited to the declared support and to the simply supported beam model using the coefficient rule in Eq. (8). Outside this support, or for structural schemes, loads or restraints not represented in the campaign, the complete EN 1993 verification must be applied, where appropriate supplemented by numerical modelling. The release package retains the populations, coefficients, scripts, audits, figures and application under the same version identifier `REV3_FIXED_THIRDS_A09_gammaM1_1.10_M3_DOMAIN`.

8. Finite-element models and comparison with EN 1993

8.1. Modelling framework

The comparison among the EN 1993 formulation, LTBeamN analyses and the subsequent finite-element models developed in LUSAS must be interpreted in light of the differing purposes of the three approaches. EN 1993 is a design procedure: it does not end with the determination of the elastic critical moment M_{cr}, but proceeds to the evaluation of the lateral-torsional slenderness, reduction factor and design resistance moment:

$$M_{cr} \longrightarrow \overline{\lambda}_{LT} \longrightarrow \chi_{LT} \longrightarrow M_{b,Rd}$$

Within this sequence, the effects of geometric imperfections, residual stresses, cross-section classification and any effective reduction of slender parts are not represented by a single explicit geometric model; rather, they are introduced through buckling curves, imperfection factors, classification rules and the resistance formulations prescribed by the standard [7, 8, 9].

Consequently, a direct comparison between a linear FEM eigenvalue result and an EN 1993 design resistance must be made with caution. A linear elastic bifurcation analysis provides a critical load multiplier and a mode shape for the idealised system, generally assuming perfect geometry, linear elastic material behaviour and no initial imperfections. As a first approximation, this result may be compared with an elastic critical moment M_{cr}, but it does not directly coincide with the design resistance moment $M_{b,Rd}$. In concise form:

$$M_{cr}^{FEM,\text{lin}} \neq M_{b,Rd}^{EN}$$

Procedure	α_{LT}	$M_{b,Rd}$ [kNm]	η	Outcome
Complete EN 1993, $\gamma_{M1} = 1.10$	0.44	17409.55	1.28	Not verified.
Parametric procedure (REV3 statistical model)	0.53	14704.86	1.52	Not verified; conservative prediction.

Table 7. *Comparison between the complete EN 1993 verification and the REV3 approximate procedure using manual design-chart readings for section P1. Values are calculated at full precision and rounded only for presentation: maximum deviation of 18% for a section in the "less frequent/boundary" domain.*

By contrast, a more direct comparison between a numerical model and a design resistance requires geometrically nonlinear and, where necessary, materially nonlinear analyses including initial imperfections, by means of GNIA or GMNIA. In such analyses, the selected shape and amplitude of the initial imperfection play a decisive role, as also highlighted by the specialist literature on lateral-torsional buckling of steel beams [38, 39, 17].

A first source of discrepancy is therefore the quantity being compared. The closed-form expressions used within EN 1993/NCCI determine the elastic critical moment through equivalent coefficients that condense the bending-moment distribution, the load application level and the effects of monosymmetry. In particular, coefficients C_1, C_2 and C_3 reduce real cases, characterised by bending-moment diagrams and distributed loads, to a closed-form expression for M_{cr} [1]. By contrast, an FEM model can represent the geometry, load distribution, restraint positions and global critical mode directly, and therefore does not necessarily reproduce the same condensation embodied in the equivalent coefficients.

A second aspect concerns the actual load position. In closed-form expressions, the stabilising or destabilising effect of a vertical load is represented by assigning a level relative to the shear centre, often taken at the top surface of the upper flange when the load is applied through fresh concrete or temporary works. In a more detailed FEM model, however, the self-weight of the steel girder is not physically applied at the top surface of the upper flange; it arises from the mass distribution and its resultant passes through the cross-section centroid. Conversely, the weight of fresh concrete and other construction loads may be applied closer to the top surface. This distinction changes the effective value of z_g, and hence the stabilising or destabilising load contribution in the lateral-torsional buckling problem.

A third source of difference concerns restraint modelling. In the EN 1993 procedure, the unrestrained segment is often idealised by a length L_b between perfect restraints, assuming that the restraints effectively prevent lateral displacement and torsional rotation of the cross-section. In an FEM model, restraints may instead have finite stiffness, eccentricity relative to the shear centre, local constraints applied to flanges or cross-girders, non-rigid connections and interactions with the transverse system. These details may alter the critical mode shape and the associated elastic multiplier.

A fourth aspect concerns local cross-section deformability. EN 1993 verifications distinguish cross-sectional resistance through classification and, for slender elements, through effective properties. A linear FEM eigenvalue model based on one-dimensional *beam/frame* elements does not represent local flange buckling, web distortion or local shear buckling of the panels. Even a three-dimensional shell model, when purely linear, returns an elastic critical load rather than an ultimate resistance including yielding, imperfections and residual stresses. These effects can be assessed more consistently only through appropriately calibrated nonlinear analyses incorporating initial imperfections [38, 39].

For these reasons, values of M_{cr} obtained from linear FEM analyses that exceed those calculated using closed-form EN 1993/NCCI expressions should not automatically be regarded as anomalous. Rather, they indicate that the elastic numerical model and the closed-form expression adopt different idealisations of loads, restraints, load application levels, moment distribution and cross-section representation. Reductions associated with imperfections, residual stresses, classification and the actual resistance of the girder enter at the subsequent stage, namely in the transition from M_{cr} to $M_{b,Rd}$. The most appropriate comparisons are therefore:

$$M_{cr}^{EN} \leftrightarrow M_{cr}^{FEM,\text{lin}}, \quad M_{b,Rd}^{EN} \leftrightarrow M_{b,Rd}^{FEM,\text{nonlin}}$$

where the second comparison requires a nonlinear model with appropriate geometric imperfections, material constitutive law, any residual stresses and collapse criteria consistent with the ultimate limit state. From this perspective, the preliminary use of LTBeamN and the subsequent LUSAS modelling are not intended to replace the EN 1993 procedure, but to complement it through progressively more detailed numerical representations. LTBeamN provides a preliminary global elastic eigenvalue check using one-dimensional *beam/frame* elements; LUSAS allows a more detailed finite-element model to be developed that can represent the actual geometry, stiffeners, restraints, load distribution and local deformability and can, where required, support nonlinear analyses incorporating imperfections. Differences among the results of the various approaches should therefore be regarded as expected and, when consistent with the adopted assumptions, provide useful insight into the margin between the code formulation, the global elastic model and the subsequent detailed FEM analysis.

8.2. Software used

The analyses were performed using LTBeamN and LUSAS. In particular, LTBeamN v. 2.0.2, developed by CTICM for the analysis of lateral-torsional buckling of structural members using a one-dimensional *beam-element* idealisation, was employed. The three-dimensional *shell*-element model was developed in LUSAS, kit version 23.0-2c4, using LUSAS Modeller v. 23.0.1636.56115 and LUSAS Solver v. 23.0.1634.8440. The use of both software packages makes it possible to compare the global response predicted by the one-dimensional model with that obtained from an explicit representation of the flanges, web and stiffeners. In both cases, the comparison refers to a linear elastic eigenvalue analysis, with load, restraint and lateral-torsional unrestrained-length conditions matched as closely as practicable. LTBeamN describes the global girder behaviour through equivalent cross-sectional properties and does not directly represent local plate buckling or distortional deformation of the cross-section. By contrast, the LUSAS model can exhibit local, distortional and global modes, making it necessary to examine a sufficiently broad set of eigenvalues to identify the lateral-torsional mode of interest. The comparison between the two software packages must therefore consider jointly the critical multiplier, the number and location of half-waves, and the global kinematics of the compression flange. The amplitudes of the mode shapes are not directly comparable because they depend on the arbitrary normalisation of the eigenvectors adopted by the respective solvers and on any graphical amplification factor applied during post-processing. The displayed displacements therefore do not represent physical deformations attained by the structure; they serve only to make the shape of the eigenmode associated with the relevant eigenvalue recognisable. The comparison must be based on the geometry of the mode shape, considering the number and position of half-waves, modal nodes, maximum lateral displacements and sign reversals along the compression flange. A consistent torsional rotation of the cross-section and any superposition of local or distortional components are also relevant; these are visible in the *shell*-element model but cannot be reproduced by the one-dimensional model. Only by imposing the same normalisation with respect to a selected degree of freedom would a quantitative comparison of relative modal amplitudes be possible, without attributing to them the significance of actual displacements.

8.3. Geometry and applied loads

8.3.1. Geometric data of the reference cross-section

As a case study, a cross-section comparable with that used in the two central quarters of the span of the steel–concrete composite Noce Expressway viaduct near Lagonegro, Basilicata, was selected (details in [16]). The viaduct has 10 mm-thick web plates, vertical stiffeners $\neq 250 \cdot 10$ at 2415 mm spacing, and one internal pair of longitudinal stiffeners $\neq 150 \cdot 10$, positioned 700 mm and 1700 mm below the underside of the upper flange. In the two central quarters, the upper flange consists of a single plate $\neq 500 \cdot 35$, whereas the lower flange is assembled from two centred superimposed plates

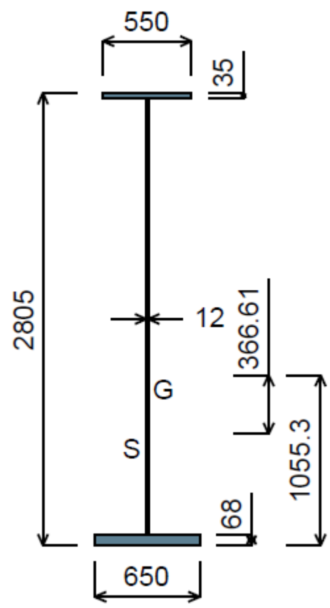

Figure 13. *Cross-section analysed. G and S denote, respectively, the positions of the geometric centroid and shear centre, measured from the underside of the lower flange. Screenshot from LTBeamN.*

$\neq 650 \cdot 30$ and $\neq 600 \cdot 38$, connected by continuous longitudinal 7×7 fillet welds along the lateral offsets of the upper plate. The overall girder depth in the span sections reaches 2803 mm.

8.3.2. Geometric data of the analysed cross-section

The analysed cross-section was selected as a similar configuration, but with the web-panel thickness increased to 12 mm and lower- and upper-flange thicknesses of 68 mm and 35 mm, respectively. The resulting web depth is 2702 mm, with an overall depth of 2805 mm. The following data were adopted for the cross-section:

- steel material properties: $E = 210000\,\mathrm{MPa}$, $G = 80769\,\mathrm{MPa}$, $\nu = 0.3$, $\rho = 7850\,\mathrm{kg/m^3}$;
- design span between supports: $L = 48.00\,\mathrm{m}$;[7]
- distance of geometric centroid G from the underside of the lower flange: $z_G = 1055.3\,\mathrm{mm}$;
- distance of shear centre S from geometric centroid G: $z_S = -366.61\,\mathrm{mm}$ (negative because it lies below centroid G);
- second moment of area about the major y–y axis: $I_y = 1.279 \times 10^7\,\mathrm{cm}^4$;
- second moment of area about the minor z–z axis: $I_z = 204186\,\mathrm{cm}^4$;
- torsion constant: $I_t = 7277.1\,\mathrm{cm}^4$ (ArcelorMittal);

[7]The support restraint sections were deliberately imposed at the geometric end sections so that the results of the manual code calculations could be correlated with those of the numerical FEM models. For the reference structure (the steel–concrete composite Noce Expressway viaduct near Lagonegro, Basilicata), the end sections of the steel girders are located 1000 mm from the bearing centre-lines [16].

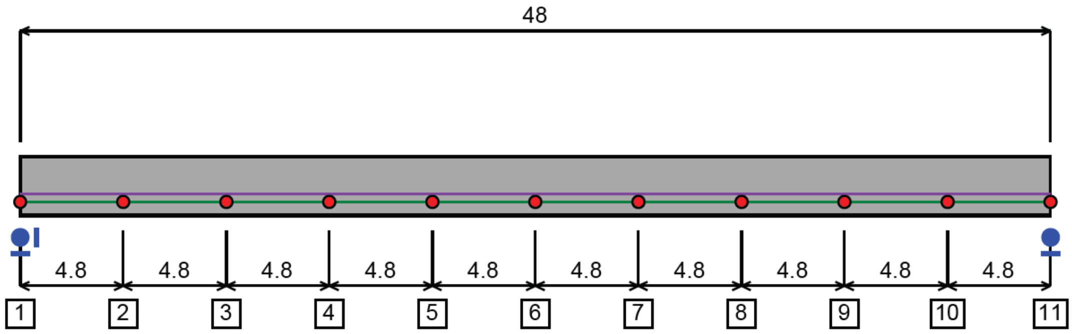

Figure 14. *Longitudinal girder layout showing the end supports and torsional-restraint sections. Figure extracted from LTBeamN. Torsional restraint conditions imposed at the ends of the segments $L_b = 4.80\,\mathrm{m}$: v and θ fixed; $v\prime$ and $\theta\prime$ free. Conditions imposed at the supported ends: u and w fixed; $w\prime$ free. Reference axes: U (longitudinal direction), V (transverse direction, into the plane of the page), and W (vertically upwards).*

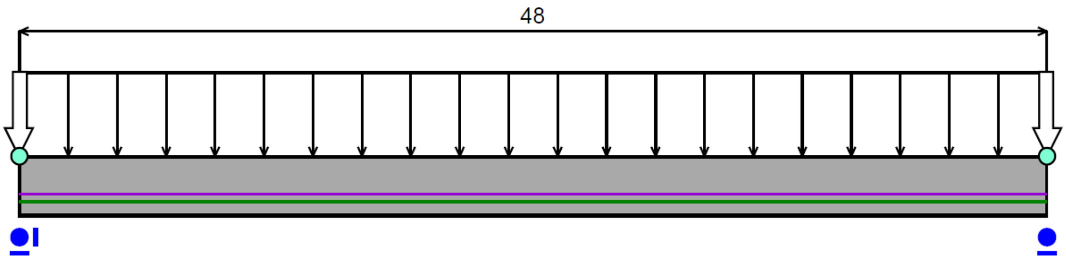

Figure 15. *Equivalent uniformly distributed load applied at the top surface of the upper flange. Figure extracted from LTBeamN.*

- warping constant: $I_w = 2.805 \times 10^9\,\mathrm{cm}^6$;
- cross-sectional area: $A = 958.74\,\mathrm{cm}^2$;
- effective shear area along the principal y–y axis (parallel to the flanges): $A_{v,y} = 634.5\,\mathrm{cm}^2$;
- effective shear area along the principal z–z axis (parallel to the web): $A_{v,z} = 330.42\,\mathrm{cm}^2$;
- elastic section modulus at the upper fibre (bending about the major y–y axis): $W_{el,y,\mathrm{sup}} = 73095\,\mathrm{cm}^3$;
- elastic section modulus at the lower fibre (bending about the major y–y axis): $W_{el,y,\mathrm{inf}} = 121200\,\mathrm{cm}^3$;
- plastic section modulus (bending about the major y–y axis): $W_{pl,y} = 96494\,\mathrm{cm}^3$;
- elastic section modulus at the extreme fibres (bending about the minor z–z axis): $W_{el,z} = 6282.6\,\mathrm{cm}^3$;
- plastic section modulus (bending about the minor z–z axis): $W_{pl,z} = 9926.6\,\mathrm{cm}^3$.

8.3.3. Equivalent load data

The complete load analysis for the casting stage is given in Section 6.1. The maximum design moment adopted in the analytical and numerical comparisons is:

$$M_{Ed} = 22325.00\,\mathrm{kNm}.$$

To impose the same action level in the different models, this moment is reproduced by a fictitious uniformly distributed load applied at the top surface of the upper flange:

$$p^* = \frac{8M_{Ed}}{L^2} = \frac{8 \cdot 22325.00\,\mathrm{kNm}}{(48.00\,\mathrm{m})^2} = 77.52\,\mathrm{kN/m}.$$

8.4. Analysis using LTBeamN v.2.0.1 and EN 1993 guidance

As an additional check of the proposed procedure, a preliminary numerical lateral-torsional buckling analysis was carried out using LTBeamN v.2.0.1, developed by CTICM. The software should not be regarded as a detailed three-dimensional FEM model of the girder, but as an eigenvalue model based on one-dimensional beam/frame finite elements, hereafter also referred to as *beam/frame* elements. From this perspective, LTBeamN provides an intermediate level of verification between the EN 1993 analytical/code formulation and the subsequent three-dimensional FEM modelling performed using LUSAS.

Before presenting the numerical comparison, it should be clarified that in this subsection the expression "gross steel cross-section" denotes the steel girder alone, without any contribution from the composite slab, longitudinal stiffeners or Class 4 effective-section reductions. The elastic properties used in the comparison, including I_z, I_t, I_w and β_z, are therefore those of the gross cross-section adopted in the LTBeamN model. The critical moment denoted below by $M_{cr}^{EN,\text{gross section}}$ is consequently the elastic critical moment obtained from the EN 1993/ENV–NCCI closed-form expression applied to the same gross elastic cross-section used in LTBeamN.

It is important to state the limitations of the approach from the outset. LTBeamN determines the global out-of-plane elastic bifurcation of the girder, associated with lateral displacement, torsion and lateral-torsional buckling, but does not perform code resistance checks. The software output is therefore not a design resistance moment, but a global elastic critical moment. The software does not classify the cross-section according to EN 1993, determine effective sections, calculate the reduction factor χ_{LT} directly, or check local plate buckling. In particular, cross-sections are assumed to remain undeformed in their own plane; local buckling of the flanges or web, cross-section distortion, local shear buckling of web panels and local mechanisms governed by stiffeners are therefore not modelled. Any shear contribution to the energy balance of the global elastic problem must not be interpreted as a web shear-buckling verification.

The LTBeamN model can therefore be used to check the global elastic critical moment M_{cr} and the corresponding mode shape, but it replaces neither the EN 1993 verification nor a detailed FEM model. In this study, it precedes the LUSAS analysis, providing a progressive transition from the code-based closed-form expression to a more advanced numerical representation and anticipating possible discrepancies arising from the differing levels of idealisation.

The software determines the elastic critical multiplier of the system through an eigenvalue formulation for the restrained girder, using lateral displacement, torsional rotation, lateral bending rotation and warping deformation as out-of-plane degrees of freedom. In concise form, the problem solved by the software may be written as:

$$[K_L - \mu_{cr} K_G]\,\mathbf{X} = \mathbf{0}$$

from which the maximum elastic critical moment is obtained as:

$$M_{cr}^{LTB} = \mu_{cr} M_{\max}$$

The resulting value is therefore not a design resistance, but the global elastic critical moment of the numerical model, which may be used as input or as a comparison value in the subsequent EN 1993 stability verification.

In the model considered, lateral-torsional restraints were placed at the transverse members, with the adopted spacing:

$$L_b = 4.80\,\mathrm{m}$$

The restraints were applied at the shear centre of the cross-section, preventing lateral displacement and torsional rotation while leaving lateral bending rotation and warping deformation free. In kinematic terms, the adopted condition is:

$$v = 0 \qquad \theta = 0 \qquad v' \text{ free} \qquad \theta' \text{ free}$$

This configuration is consistent with the effective lateral-torsional restraint assumed in the EN 1993 procedure, in which the unrestrained segment is taken as the distance between consecutive restraints capable of preventing lateral displacement and torsional rotation of the cross-section.

The vertical load was applied at the top surface of the upper flange so that the numerical model includes the destabilising effect of the load application level relative to the shear centre. For the same structural scheme, LTBeamN therefore provides the global elastic critical moment of the restrained girder, whereas the EN 1993/NCCI procedure used in this study calculates the elastic critical moment through a closed-form expression of the following type:

$$M_{cr}^{EC3} = C_1 \frac{\pi^2 E I_z}{(kL_b)^2\, g}\left[\left(\left(\frac{k}{k_w}\right)^2 \frac{I_w}{I_z} + \frac{(kL_b)^2 G I_t}{\pi^2 E I_z} + (C_2 z_g - C_3 z_j)^2\right)^{1/2} - (C_2 z_g - C_3 z_j)\right]$$

A particularly sensitive aspect of the formulation is the sign convention for the monosymmetry term z_j. In this study, the term is defined as:

$$z_j = z_s - \frac{1}{2I_y}\int_A z\left(y^2 + z^2\right)\,\mathrm{d}A$$

where z_s is the elevation of the shear centre relative to the cross-section centroid, using the sign convention adopted in the cross-section geometry.

Introducing the Wagner vertical asymmetry coefficient:

$$\beta_z = \frac{1}{2I_y}\int_A z\left(y^2 + z^2\right)\,\mathrm{d}A - z_s$$

gives:

$$z_j = -\beta_z$$

With the convention adopted for the cross-section considered:

$$z_g > 0 \qquad z_j < 0$$

Therefore, in the combination appearing in the elastic critical-moment formulation:

$$\Delta = C_2 z_g - C_3 z_j$$

the monosymmetry contribution has an additive sign:

$$-C_3 z_j = +C_3\,|z_j|$$

and hence:

$$\Delta = C_2 z_g + C_3\,|z_j|$$

This increases the equivalent term Δ, and its sign is retained in the closed-form expression. The overall numerical outcome also depends on C_1, torsional stiffness and warping stiffness; the relative order of M_{cr}^{EC3} and the LTBeamN value therefore cannot be inferred a priori from the sign of z_j alone.

To clarify the difference between the two approaches, a direct comparison was made between the elastic critical moment returned by LTBeamN and that obtained from the EN 1993/ENV–NCCI closed-form expression.

The comparison assumed the gross steel cross-section, namely the steel section without the contribution of the composite slab, longitudinal stiffeners or any effective-section reductions. For this specific comparative check, the EN 1993/ENV–NCCI calculation used the same elastic cross-sectional properties as the LTBeamN model. In other words, I_z, I_t, I_w and β_z were not recalculated using the parametric engine with stiffeners, but were taken directly from the gross-section geometric data reported by the software. The principal elastic properties adopted are:

$$\begin{aligned} A_{v,z} &= 330.42\,\mathrm{cm}^2 \\ I_y &= 1.279 \cdot 10^7\,\mathrm{cm}^4 \\ I_z &= 204186\,\mathrm{cm}^4 \\ I_t &= 7277.1\,\mathrm{cm}^4 \\ I_w &= 2.805 \cdot 10^9\,\mathrm{cm}^6 \\ \beta_z &= 66.09\,\mathrm{cm} \end{aligned}$$

With this arrangement, the comparison is unaffected by possible differences in the reconstruction of the cross-sectional properties: LTBeamN and the EN 1993/ENV–NCCI expression use the same underlying elastic cross-section. The difference between the results therefore depends solely on the different formulation of the elastic buckling problem, and not on different assumptions for I_z, I_t or I_w.

The elastic and plastic section moduli reported by the software are:

$$\begin{aligned} W_{el,y,\mathrm{sup}} &= 73095\,\mathrm{cm}^3 \\ W_{el,y,\mathrm{inf}} &= 121200\,\mathrm{cm}^3 \\ W_{el,z} &= 6282.6\,\mathrm{cm}^3 \\ W_{pl,y} &= 96494\,\mathrm{cm}^3 \\ W_{pl,z} &= 9926.6\,\mathrm{cm}^3 \end{aligned}$$

These moduli are reported only as a geometric check of the gross cross-section without longitudinal stiffeners. They do not enter the elastic calculation of M_{cr} and must not be confused with the section moduli used in the code resistance verification, which depend on the cross-section class. The distance between the vertical load application point, located at the top surface of the upper flange, and the shear centre is:

$$z_g \simeq 211.63\,\mathrm{cm} = 2116.3\,\mathrm{mm}$$

whereas, with the adopted convention:

$$z_j = -\beta_z \simeq -66.09\,\mathrm{cm} = -660.9\,\mathrm{mm}$$

For comparison with the LTBeamN model, the actual lateral-torsional unrestrained length of the segment between two consecutive restraints must be used, namely $L_b = 4.80\,\mathrm{m}$. Since $L_b/L = 0.10 < 0.25$, the rule in Eq. (8) assigns the locally uniform-moment model to the short segment:

$$C_1 = 1.000, \qquad C_2 = 0.000, \qquad C_3 = 1.000.$$

The load remains applied above the upper flange, but z_g does not appear directly in this branch because $C_2 = 0$. The equivalent term is (LTBeamN follows the convention in Fig. 1 on page 4):

$$\begin{aligned} \Delta &= C_2 z_g - C_3 z_j \\ &= 0 - 1 \cdot (-660.9\,\mathrm{mm}) \\ &= 660.9\,\mathrm{mm}. \end{aligned}$$

Using the same elastic cross-sectional properties as in the LTBeamN model, the corrected EN 1993 core gives:[8]

$$M_{cr}^{EN,\mathrm{sez.lorda}} = 128966.96\,\mathrm{kNm}.$$

For the same gross cross-section, restraint arrangement and load applied above the upper flange, the LTBeamN model gives (fig. 16):

$$M_{cr,1}^{LTB} = 146022\,\mathrm{kNm}.$$

The ratio is therefore:

$$\frac{M_{cr,1}^{LTB}}{M_{cr}^{EN,\mathrm{sez.lorda}}} = \frac{146022}{128967} = 1.132.$$

The closed-form expression therefore gives a critical moment approximately 13.2% lower than that obtained from the LTBeamN model. In general, the difference cannot be attributed to the longitudinal stiffeners, which are absent from both models in this particular comparison, nor to different values of I_z, I_t or I_w; it arises from the different level of idealisation of the global problem and from the condensation of the effects in the analytical segment model.

LTBeamN directly solves the global elastic bifurcation problem of the complete girder through an eigenvalue analysis based on one-dimensional beam/frame finite elements, explicitly representing the lateral-torsional restraint system, the load position relative to the shear centre and the global critical mode of the restrained girder. This representation nevertheless assumes an undeformable cross-section and does not include local or distortional modes of the component plates. By contrast, the EN 1993/ENV–NCCI formulation reduces the problem to an equivalent segment of length L_b, in which the effects of moment distribution, load application level and cross-sectional monosymmetry are condensed into C_1, C_2, C_3, z_g and z_j.

For the case considered, using the same elastic cross-sectional properties and the coefficient rule adopted in the REV3 calibration, the global elastic eigenvalue analysis therefore gives an M_{cr} value higher than that obtained from the EN 1993/ENV–NCCI closed-form expression. This is not anomalous, but reflects the different levels of idealisation of the two approaches: the LTBeamN numerical model describes the global out-of-plane behaviour of the restrained girder as a whole, whereas the code closed-form expression adopts an equivalent and necessarily condensed representation

[8] Detailed calculations are omitted for reasons of space.

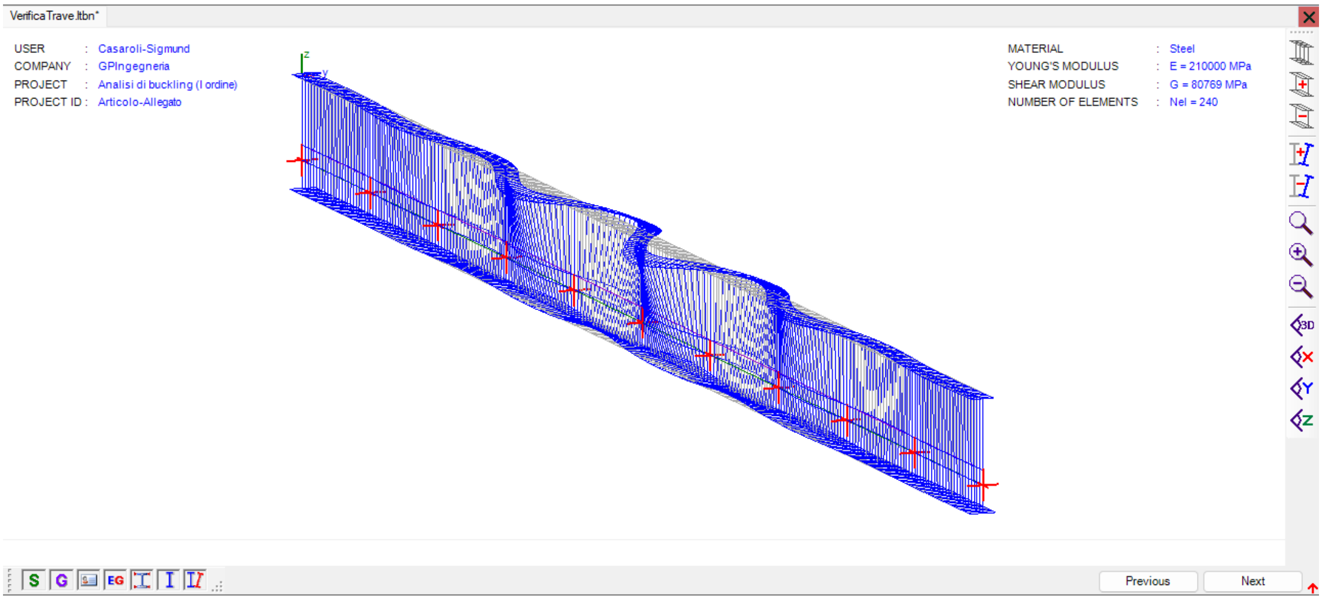

Figure 16. *Mode shape associated with the first elastic lateral-torsional buckling mode obtained using LTBeamN v.2.0.1. The intermediate restraints are modelled as point restraints applied at the shear centre, preventing lateral displacement v and torsional rotation θ of the cross-section. The lateral bending rotation $v\prime$ and warping deformation $\theta\prime$ remain free; the adopted restraint is therefore equivalent to a fork-type restraint with free warping. For the first buckling mode, the software gives an elastic critical multiplier of approximately $\mu_{cr,1} = 6.541$, corresponding to $M_{cr,1}^{LTB} = 146022\,\mathrm{kNm}$ for the load applied above the upper flange.*

of the problem. The comparison should therefore be read as a preliminary global elastic check, not as validation of the girder resistance or as exclusion of possible local criticalities.

The coefficients C_1, C_2 and C_3 must therefore be selected for the actual lateral-torsional unrestrained segment being verified. Intermediate restraints do not alter the global vertical static scheme, which remains a simply supported girder under distributed load, but they do change the length available to the lateral-torsional mode. The coefficients are therefore assigned as functions of L_b/L through the two-branch rule in Eq. (8), applied to the segment being checked.

The comparison between LTBeamN and the EN 1993/ENV–NCCI procedure must therefore be interpreted as a comparison between two different levels of modelling. The former is a global numerical eigenvalue model based on one-dimensional beam/frame finite elements and restricted to global elastic out-of-plane modes; the latter is a closed-form code procedure based on equivalent coefficients. The observed differences between M_{cr}^{LTB} and M_{cr}^{EC3} are mainly attributable to the different representation of the global critical mode, the condensation of the destabilising load into $C_2 z_g - C_3 z_j$, and the representation of monosymmetry by z_j in the EN 1993/ENV–NCCI expression. Once the elastic critical moment has been determined according to EN 1993/ENV–NCCI, the rigorous verification proceeds through evaluation of the lateral-torsional slenderness, reduction factor and design resistance moment:

$$M_{cr}^{EC3} \longrightarrow \overline{\lambda}_{LT} \longrightarrow \chi_{LT} \longrightarrow M_{b,Rd}^{EC3}$$

For Class 4 cross-sections, this sequence also requires determination of the effective cross-sectional properties, because bending resistance cannot be evaluated using gross section moduli alone.

The approximate procedure proposed in this study is positioned at the final stage of this framework. It is not calibrated to reproduce on a pointwise basis the M_{cr}^{LTB} value provided by LTBeamN, but to provide an operational estimate of the equivalent resistance moment that is consistent with, and conservative relative to, the EN 1993 procedure. In this form, the verification is expressed as:

$$A_c^2 \geq \widehat{\alpha}_{LT}\,(\boldsymbol{p})\,M_{eq} L_b$$

or, in terms of the equivalent resistance moment:

$$M_{b,Rd}^{\mathrm{app}} = \frac{A_c^2}{\widehat{\alpha}_{LT}\,(\boldsymbol{p})\,L_b}$$

The relationship among the three calculation levels must therefore be read in the following logical order: LTBeamN provides a preliminary numerical check of the global elastic critical moment; the EN 1993/ENV–NCCI procedure provides the code reference for determining $M_{b,Rd}^{EC3}$; and the proposed approximate procedure provides a simplified, conservative estimate of $M_{b,Rd}$ calibrated against the EN 1993 procedure rather than directly against the eigenvalue model.

From this perspective, any differences between M_{cr}^{LTB} and M_{cr}^{EC3} do not invalidate the approximate procedure, but highlight the different levels of idealisation of the global numerical model and the code closed-form expression. The proposed procedure should therefore be understood as an operational tool for preliminary sizing and verification, to be used within the declared calibration domain and with the formula derived from the statistical analysis and the stated domain limits. For cases close to those limits, or where the torsional effectiveness of the restraint system cannot be clearly demonstrated, the approximate procedure should be supplemented by a more detailed finite-element model.

The subsequent three-dimensional FEM investigation of the girder using LUSAS enabled a more direct assessment of the actual stiffness of the transverse restraints, local plate deformability, interaction among flanges, web and stiffeners, and the possible occurrence of local or distortional modes not represented by LTBeamN. The LUSAS analysis therefore constitutes the detailed finite-element modelling stage following the preliminary eigenvalue check using one-dimensional *beam/frame* finite elements and permits a more complete interpretation of the discrepancies among the EN 1993 closed-form formulation, the LTBeamN beam-element model and the three-dimensional numerical behaviour of the girder represented by two-dimensional shell elements.

9. FEA using LUSAS

9.1. Modelling notes on buckling analysis

9.1.1. Introduction to buckling analysis

The buckling analysis depends on the applied loads and on the order in which they are applied. In most simulations, it is advisable to consider gravity effects in a separate load case. Moreover, the buckling analysis depends on the initial geometry adopted for the model. A theoretically perfect geometry, free from imperfections, will produce results that differ substantially from those obtained for an initially deformed or imperfect geometry.

An eigenvalue buckling analysis requires the use of elements with geometrically nonlinear capabilities, so that additional stress–strain terms can be included in the stiffness matrix.

9.1.2. Theoretical background in LUSAS

In the present numerical model, the lateral-torsional buckling of the girder is investigated through a three-dimensional shell-element discretisation. The operational reference is consistent with the LUSAS example *Buckling Analysis of a Plate Girder*, in which the plates forming the steel girder, including the web, flanges and stiffeners, are modelled using quadratic quadrilateral surface elements identified as QSL8 *thick shell* elements [32]. From a theoretical standpoint, however, the LUSAS `Theory Manual` classifies the QSL8 element within the *Semiloof Thin Shell* family [31]. This apparent terminological difference arises because the QSL8 is formulated from a degenerated three-dimensional thick-shell element, upon which Kirchhoff kinematic constraints are subsequently imposed to obtain thin-shell performance.

As shown by the nodal configuration of the QSL8 element reported in the LUSAS *Theory Manual*, Fig. 7.7.3-3, p. 178 (see Fig. 18), the quadrilateral semiloof element retains translational displacements at the corner and midside nodes, whereas rotations are associated with the *loof* nodes.

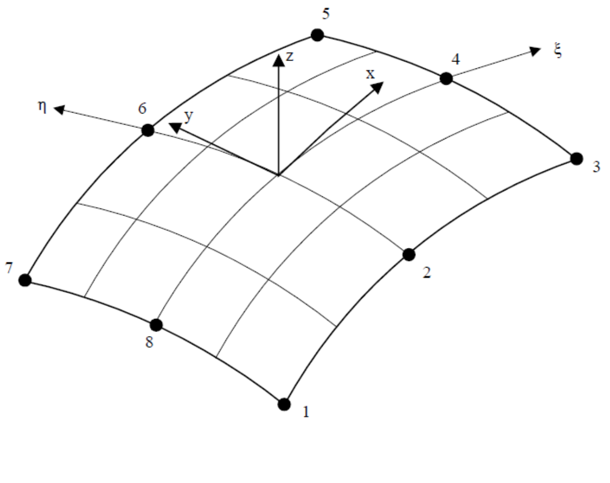

Figure 17. *Geometric layout of the QSL8 element used in LUSAS shell modelling: the corner and midside nodes define the element midsurface, while the natural coordinates ξ, η govern the isoparametric interpolation. Source: LUSAS, Theory Manual, Volume 2, Fig. 7.7.3-8, p. 181 [31]*

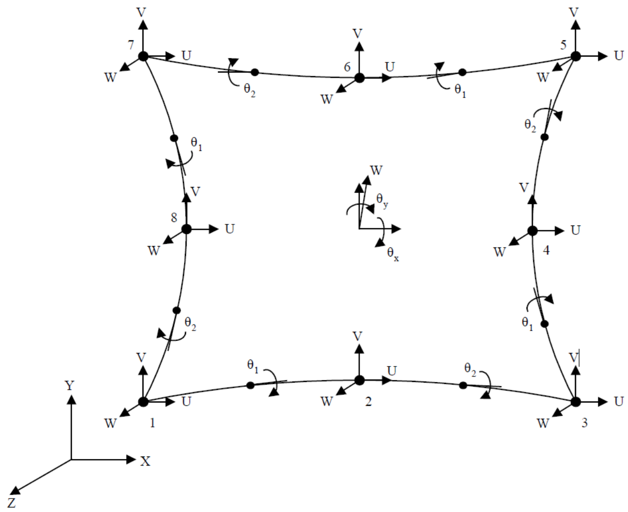

Figure 18. *Final nodal configuration of the QSL8 quadrilateral semiloof element, showing the translational degrees of freedom U, V, W and the rotations associated with the loof nodes. Source: LUSAS, Theory Manual, Volume 2, Fig. 7.7.3-3, p. 178 [31]*

In particular, the manual describes the QSL8 as a doubly curved isoparametric shell element (Fig. 17) in which displacements and rotations are initially assumed to be independent. The final nodal configuration retains translational displacements (along the three principal Cartesian directions):

$$U,\ V,\ W$$

at the corner and midside nodes, while rotations are associated with the so-called *loof nodes*. The transition from the degenerated “thick” shell formulation to “thin” shell behaviour is obtained by imposing the discrete vanishing of the transverse shear strains. In symbolic form, the following constraint is imposed for transverse shear tangential to the element edge (an internal kinematic constraint of the shell element):

$$\gamma_t = \theta_y - \frac{\partial w}{\partial x} = 0,$$

where γ_t is the transverse shear strain tangential to the element edge, w is the transverse displacement (out of the midsurface plane of the shell element), $\partial w/\partial x$ is the slope of the deformed midsurface in the local x direction, and θ_y is the rotation of the normal to the midsurface about the local y axis. The condition $\theta_y = \partial w/\partial x$ indicates that the rotation of the normal is constrained to coincide with the slope of the transverse deflection. In other words, along all the element edges, the normal to the midsurface remains normal to the deformed midsurface after deformation (the *Kirchhoff–Love* hypothesis for thin plates and shells: $\gamma_{xz} = \gamma_{yz} = 0$). In a "thick shell" element based on the Mindlin–Reissner formulation, the director initially normal to the midsurface may rotate independently of the geometric normal to the deformed midsurface. In kinematic terms, the rotation θ_y of this material direction may therefore differ from the slope $\partial w/\partial x$ of the deformed midsurface:

$$\gamma_t = \theta_y - \frac{\partial w}{\partial x} \neq 0.$$

The quantity γ_t represents the transverse shear strain: it measures the angular misalignment between the material direction through the thickness and the geometric normal to the deformed midsurface.

Further kinematic conditions imposed over the element area and along its edges are expressed by the following integral forms:

$$\int_A \gamma_{xz}\,\mathrm{d}A = 0, \qquad \int_A \gamma_{yz}\,\mathrm{d}A = 0, \qquad \int_S \gamma_n\,\mathrm{d}S = 0.$$

These constraints eliminate transverse shear modes that are incompatible with the Kirchhoff kinematic hypothesis and allow certain internal degrees of freedom to be condensed out, while retaining a formulation suitable for representing the bending and membrane response of stiffened thin plates.

In the linear range, the strain–displacement relationship adopted for the shell is expressed, in the local element system, by the membrane components:

$$\varepsilon_x = \frac{\partial u}{\partial x}, \qquad \varepsilon_y = \frac{\partial v}{\partial y}, \qquad \gamma_{xy} = \frac{\partial u}{\partial y} + \frac{\partial v}{\partial x},$$

and by the bending curvatures:

$$\psi_x \simeq -\frac{\partial^2 w}{\partial x^2}, \qquad \psi_y \simeq -\frac{\partial^2 w}{\partial y^2}, \qquad \psi_{xy} \simeq -2\frac{\partial^2 w}{\partial x\,\partial y}.$$

For an isotropic elastic material, the shell constitutive law may be written by separating the membrane contribution ($\mathbf{D}_m$) from the bending contribution ($\mathbf{D}_b$):

$$\mathbf{D} = \begin{bmatrix} \mathbf{D}_m & \mathbf{0} \\ \mathbf{0} & \mathbf{D}_b \end{bmatrix},$$

which, in the usual form of resultant stiffness per unit width, are given by:

$$\mathbf{D}_m = \frac{Et}{1-\nu^2}\begin{bmatrix} 1 & \nu & 0 \\ \nu & 1 & 0 \\ 0 & 0 & \dfrac{1-\nu}{2} \end{bmatrix}$$

$$\mathbf{D}_b = \frac{Et^3}{12(1-\nu^2)}\begin{bmatrix} 1 & \nu & 0 \\ \nu & 1 & 0 \\ 0 & 0 & \dfrac{1-\nu}{2} \end{bmatrix}$$

The element response is therefore governed both by the membrane stress resultants:

$$N_x,\ N_y,\ N_{xy},$$

and by the bending and twisting moments per unit width:

$$M_x,\ M_y,\ M_{xy},$$

evaluated in the local element system.

For buckling purposes, the essential point is that LUSAS declares the QSL8 suitable for both linear and nonlinear buckling analyses. In a linear eigenvalue buckling analysis, the critical load is not obtained from the initial elastic stiffness alone, but from the combination of the elastic stiffness and the geometric stiffness, or *stress stiffness*, generated by the reference stress state. In concise form, the eigenvalue problem may be represented as:

$$(\mathbf{K} + \mu_i\,\mathbf{K}_\sigma)\,\boldsymbol{\Phi}_i = \mathbf{0},$$

where $\mathbf{K}$ is the elastic stiffness matrix, $\mathbf{K}_\sigma$ is the geometric stiffness matrix dependent on the initial stress state, μ_i is the critical multiplier associated with the ith mode, and $\boldsymbol{\Phi}_i$ is the corresponding modal eigenvector. The critical load associated with the ith mode is therefore:

$$\mathbf{R}_{cr,i} = \mu_i\,\mathbf{R}_0,$$

where $\mathbf{R}_0$ is the vector of the loads applied in the reference state. It follows that the buckling result is intrinsically dependent on both the load distribution and the initial geometry of the model.

For geometrically nonlinear analysis, LUSAS permits a total Lagrangian formulation for the QSL8. In the total Lagrangian formulation, suitable for large displacements but small rotations and small strains, the membrane strains include quadratic displacement terms:

$$\varepsilon_x = \frac{\partial u}{\partial x} + \frac{1}{2}\left[\left(\frac{\partial u}{\partial x}\right)^2 + \left(\frac{\partial v}{\partial x}\right)^2 + \left(\frac{\partial w}{\partial x}\right)^2\right]$$

$$\varepsilon_y = \frac{\partial v}{\partial y} + \frac{1}{2}\left[\left(\frac{\partial u}{\partial y}\right)^2 + \left(\frac{\partial v}{\partial y}\right)^2 + \left(\frac{\partial w}{\partial y}\right)^2\right]$$

$$\gamma_{xy} = \frac{1}{2}\left[\frac{\partial u}{\partial y} + \frac{\partial v}{\partial x} + \left(\frac{\partial u}{\partial x}\frac{\partial u}{\partial y} + \frac{\partial v}{\partial x}\frac{\partial v}{\partial y} + \frac{\partial w}{\partial x}\frac{\partial w}{\partial y}\right)\right]$$

with the well-known *reciprocity condition for shear strains* $\gamma_{xy} = \gamma_{yx}$, resulting from the general expression of the *symmetric strain tensor*:[9]

$$\varepsilon_{ik} = \frac{1}{2}\left(\frac{\partial u_i}{\partial x_k} + \frac{\partial u_k}{\partial x_i} + \frac{\partial u_\ell}{\partial x_i}\frac{\partial u_\ell}{\partial x_k}\right)$$

Within this formulation, the outputs are expressed in terms of Piola–Kirchhoff stresses and Green–Lagrange strains, referred to the undeformed configuration. In the updated Lagrangian formulation, by contrast, the reference configuration is updated along the incremental path; the outputs are expressed in terms of true Cauchy stresses and strains that may be approximated as logarithmic strains. For the lateral-torsional buckling problem, this means that the eigenvalue analysis provides an elastic critical multiplier and a mode shape, whereas a more realistic assessment of resistance may require a geometrically nonlinear analysis with initial imperfections and, where appropriate, the inclusion of material nonlinearity.

Finally, it is important to note that the eigenmode obtained from a linear buckling analysis is normalised and does not directly represent a physical deformation state at full scale. It must be interpreted as an indicator of the buckled shape and the corresponding critical multiplier. The distinction between global modes, such as overall lateral-torsional buckling of the girder, and local modes, such as buckling of web panels, flanges or stiffeners, must therefore be made through engineering judgement, by examining the mode shapes and their consistency with the expected structural phenomenon.

9.1.3. Analyses performed

The numerical simulations carried out in this study are intended to assess the buckling behaviour of a steel girder using finite-element models developed in LUSAS. The objective is not limited to determining an elastic critical multiplier, but also includes evaluating the evolution of structural deformation in the presence of geometrically nonlinear effects and initial imperfections.

In the first stage, a linear eigenvalue buckling analysis is performed. This analysis determines the critical multipliers of the applied loads and the corresponding buckling mode shapes. The results provide an elastic estimate of the critical load and allow the most significant buckling modes, whether global or potentially local, to be identified. It should nevertheless be noted that this approach assumes linear elastic behaviour, does not account for the evolution of pre-buckling displacements and provides no quantitative information on post-buckling behaviour. The resulting mode shapes therefore have a qualitative and relative meaning, as they are normalised, and do not directly represent the actual displacements of the structure at the critical load.

In the second stage, the mode shapes obtained from the eigenvalue analysis are used as a reference for introducing an initial geometric perturbation into the model. This procedure allows a geometrically nonlinear analysis with imperfections, hereinafter referred to as *GNIA*, to be performed. In this case, the structural response is traced incrementally along the load path, accounting for second-order effects and the interaction between the deformed configuration, tangent stiffness and stress state. Unlike the eigenvalue analysis, the geometrically nonlinear analysis does not directly return a single critical multiplier, but provides the complete history of the structural response. The buckling load must therefore be interpreted from load–displacement curves, identifying any marked reductions in stiffness, limit points or descending branches of the response.

The comparison between the elastic multiplier obtained from the eigenvalue analysis and the geometrically nonlinear response makes it possible to assess the girder sensitivity to initial imperfections and second-order effects. In particular, the eigenvalue analysis serves as a preliminary tool for identifying the critical modes, whereas the geometrically nonlinear analysis provides the main reference for studying the evolution of buckling in the imperfect model.

For ultimate-limit assessment, a geometrically and materially nonlinear analysis with imperfections, hereinafter referred to as *GMNIA*, was also performed. In this approach, the geometrically nonlinear effects are combined with a nonlinear material constitutive law capable of representing the attainment of the yield stress and the possible development of plastic strains. This analysis makes it possible to determine whether the ultimate response is governed primarily by geometric instability or by the onset of yielding. The present study therefore compares elastic eigenvalue buckling with both the geometrically nonlinear response incorporating imperfections and the corresponding materially nonlinear response, thereby clarifying the progressive effects of geometric and material nonlinearity.

10. Girder precamber and assessment of the deformed configuration

10.1. Determination of the equivalent load for the characteristic SLS combination

The vertical deflection of the girder was first determined using the characteristic serviceability limit state combination. The characteristic line-load contribution associated with permanent and construction actions was taken as:

$$q_{E,k} = 9.59 + (32.50 + 10.00) = 52.09\,\mathrm{kN/m}.$$

The characteristic contribution associated with the load distributed over the adopted conventional width was evaluated as:

$$q_{\mathrm{ca},B,Q_{\mathrm{ca}},k} = 1.50 \cdot 3.00 = 4.50\,\mathrm{kN/m}.$$

The corresponding characteristic bending moments, denoted by $M_{E,k}$ and $M_{Q_{\mathrm{ca}},k}$, respectively, were calculated

[9] Einstein summation notation for repeated indices is implicit.

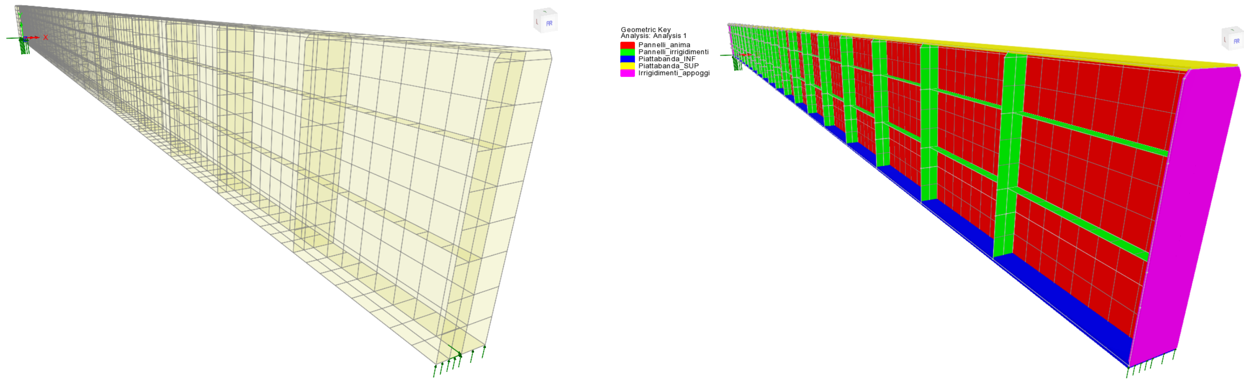

(a) *Girder mesh.* **(b)** *Girder cross-sections.*

Figure 19. *Three-dimensional axonometric representation of the single girder in LUSAS: (a) model and mesh elements; (b) display of the geometric cross-sections. Model (a), used for comparison with LTBeamN results, includes a web stiffened by vertical plates on both sides.*

separately from the two contributions. The total moment adopted to determine the initial deformed shape is therefore:

$$M_k = M_{E,k} + M_{Q_{\mathrm{ca}},k}.$$

To reproduce the same maximum moment in the FEM model by means of a single uniformly distributed action, the fictitious equivalent line load p^*_{SLE} was introduced. For a simply supported girder subjected to a uniform load:

$$M_{\mathrm{max,SLE}} = \frac{p^*_{\mathrm{SLE}} L^2}{8},$$

from which:

$$p^*_{\mathrm{SLE}} = \frac{8M_{\mathrm{max,SLE}}}{L^2} = 52.63\,\mathrm{kN/m}.$$

The equivalent line load was converted into a uniform pressure to be applied to the shell elements of the top flange. Assuming a width:

$$b_{\mathrm{sup}} = 0.55\,\mathrm{m},$$

which gives:

$$P^*_{\mathrm{SLE}} = \frac{p^*_{\mathrm{SLE}}}{b_{\mathrm{sup}}} = \frac{52.59}{0.55} = 95.69\,\mathrm{kN/m}^2.$$

The pressure P^*_{SLE} was then assigned to the shell surfaces of the top flange so as to reproduce the previously determined total bending moment.

10.2. Definition of the precamber through the initial deformed shape

The precamber was defined so as to compensate fully for the deformation calculated in *Analysis 1*. For this purpose, a second analysis, named *Analysis 2*, was created using the option:

```
Start with deformed mesh from Analysis 1,
```

with reference to the *load case* containing the equivalent load and adopting a scale factor equal to:

$$s = -1.0.$$

Let $\boldsymbol{x}_0$ denote the vector of nodal coordinates of the originally straight geometry and $\boldsymbol{u}^{(1)}$ the displacement field calculated in Analysis 1. The initial configuration of Analysis 2 is defined by

$$\boldsymbol{x}_0^{(2)} = \boldsymbol{x}_0 - \boldsymbol{u}^{(1)}.$$

Considering the vertical component alone gives

$$Y_{0,i}^{(2)} = Y_{0,i} - DY_i^{(1)},$$

where $DY_i^{(1)}$ is the vertical displacement of node i obtained in Analysis 1.

Since the displacements produced by the gravitational load are negative:

$$DY_i^{(1)} < 0,$$

the initial configuration of Analysis 2 has an upward displacement equal to:

$$\Delta Y_{\mathrm{prem},i} = -DY_i^{(1)} > 0.$$

The precamber introduced in this way is therefore not a separately prescribed geometric curve, but is obtained directly by reversing the deformation field calculated in the first analysis.

In general, the option used by LUSAS acts on the entire nodal vector:

$$\boldsymbol{u}^{(1)} = \begin{bmatrix} DX^{(1)} & DY^{(1)} & DZ^{(1)} \end{bmatrix}^{\mathsf{T}}.$$

Interpreting this modification as a purely vertical precamber therefore requires the components $DX^{(1)}$ and $DZ^{(1)}$ to be zero or negligible relative to the vertical component $DY^{(1)}$. In view of the load direction and the symmetry of the girder cross-section, the components $DX^{(1)}$ and $DZ^{(1)}$ of the nodal vector are considered negligible.

10.3. Interpretation of displacements in the analysis of the precambered girder

In Analysis 2, displacements are measured from the new initial precambered configuration rather than from the

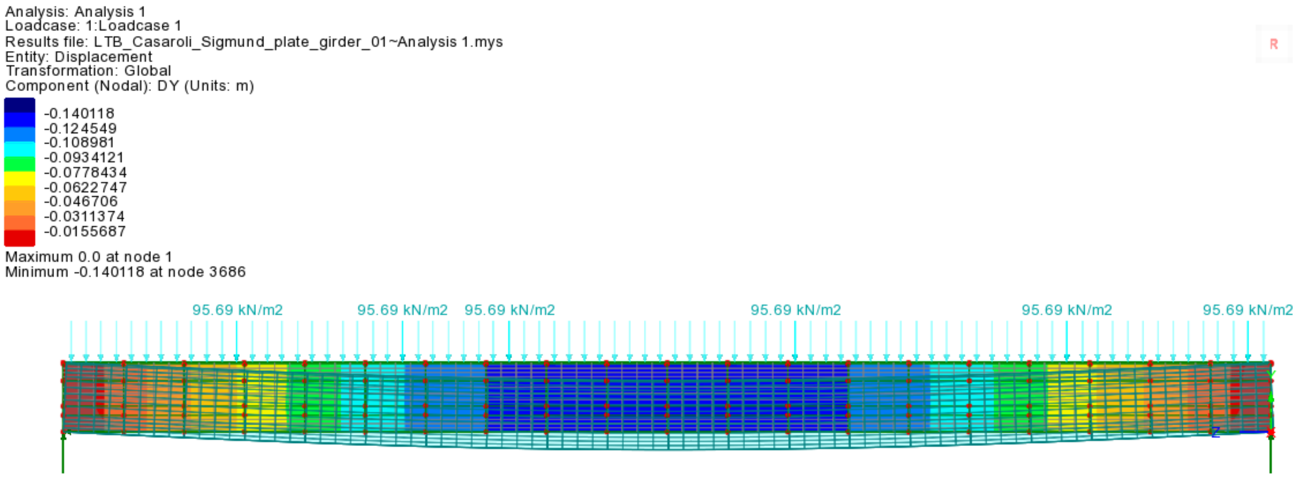

Figure 20. *Deformed configuration (with an amplified graphical scale) of the initially straight single girder, without precamber, obtained in Analysis 1 by applying the equivalent pressure P^*. The deformed shape is represented by the wireframe mesh.*

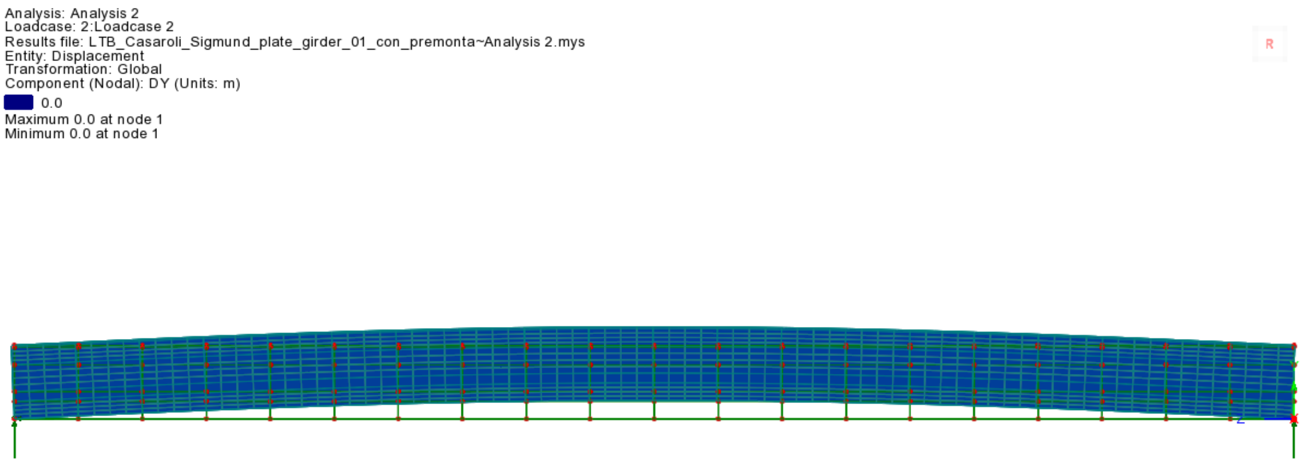

Figure 21. *Initial precambered configuration (with an amplified graphical scale) characterising the first steps of Analysis 2 before the external loads are applied. The geometry curves upwards, while the nodal result $DY^{(2)}$ is zero because the precamber constitutes the new initial configuration of the analysis.*

originally straight geometry. Therefore, in the absence of external loads:

$$DY_i^{(2)} = 0,$$

even though the girder appears geometrically curved upwards. The precamber is incorporated into the initial mesh coordinates and is not returned as a displacement result.

When the equivalent pressure P^* is reapplied in Analysis 2, LUSAS calculates a further displacement field $DY_i^{(2)}$, referred to the precambered configuration. The final vertical coordinate of node i is therefore:

$$Y_{\text{fin},i}^{(2)} = Y_{0,i} - DY_i^{(1)} + DY_i^{(2)}.$$

The final distance from the originally straight configuration is therefore:

$$\boxed{\Delta Y_{\text{rett},i} = Y_{\text{fin},i}^{(2)} - Y_{0,i} = -DY_i^{(1)} + DY_i^{(2)}}.$$

The displacement contour plot for Analysis 2 shows only the incremental contribution:

$$DY_i^{(2)} = Y_{\text{fin},i}^{(2)} - Y_{0,i}^{(2)},$$

which is negative when the load causes the girder to move downwards relative to the precambered configuration. The contour plot therefore does not include the positive precamber contribution $-DY_i^{(1)}$.

Where the behaviour is substantially linear and the same load used in Analysis 1 is applied in Analysis 2, it is reasonable to expect:

$$DY_i^{(2)} \simeq DY_i^{(1)}.$$

It follows that:

$$\Delta Y_{\text{rett},i} = -DY_i^{(1)} + DY_i^{(2)} \simeq 0,$$

that is, the downward deformation produced by the load tends to compensate for the initial precamber. For this reason, the final deformed mesh, displayed as a wireframe with a unit deformation factor, may appear almost straight: the contour plot reports negative values of $DY^{(2)}$ precisely because they are measured relative to the nodes displaced by the precamber.

The numerical assessment of the residual deformation relative to the straight girder must therefore be carried

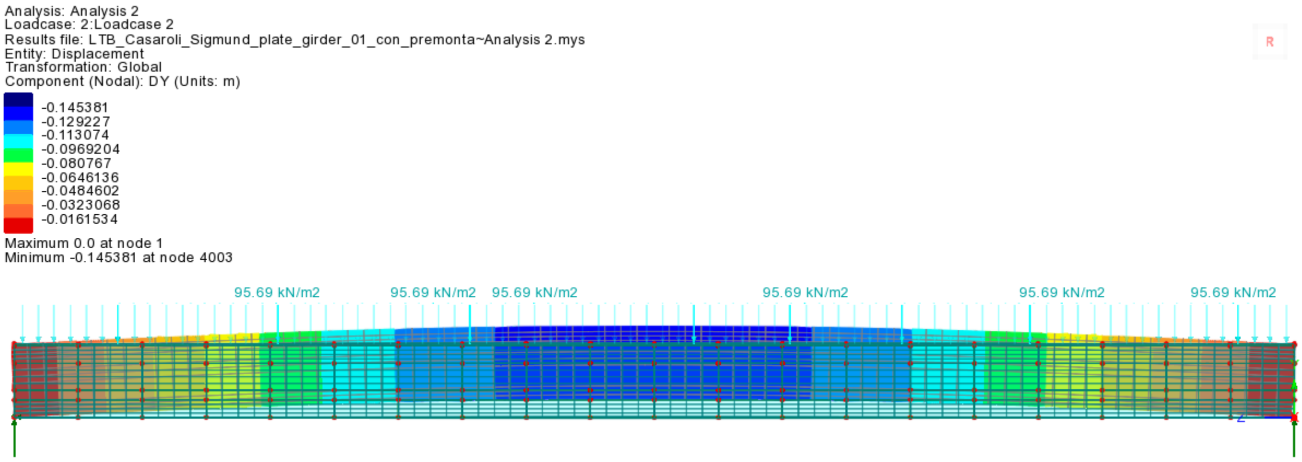

Figure 22. *Analysis 2 with application of the equivalent pressure P^*. The contour plot represents the $DY^{(2)}$ displacements (with an amplified graphical scale) developed relative to the initial precambered configuration (Fig. 21), while the deformed mesh displayed as a wireframe represents the final girder configuration in the global coordinate system. The wireframe mesh appears horizontal, indicating that the precamber "recovers" all vertical deformations caused by the loads applied during Stage I. The displacements shown in the legend are those experienced by the precambered girder in reaching a straight equilibrium configuration under all the applied loads.*

out node by node using:

$$\Delta Y_{\mathrm{rett},i} = -DY_i^{(1)} + DY_i^{(2)},$$

without directly comparing only the minimum values from the two analyses, since these may occur at different nodes.

11. Settings in the LUSAS environment

11.1. Stage-I design load

For comparison with the analytical procedure according to EN 1993-1-1, §2.1(1), and EN 1991-1-6, the Stage-I ULS design load was converted into an equivalent uniformly distributed load producing the same maximum moment M_{Ed} in the simply supported girder. The corresponding line load is:

$$q^* = \frac{8M_{Ed}}{L^2} = \frac{8 \cdot 22325.00\,\mathrm{kNm}}{(48.00\,\mathrm{m})^2} = 77.52\,\mathrm{kN/m}.$$

Since the load in the LUSAS model is applied as a uniform pressure to the upper surface of the top flange, the line-load value was divided by the width $b_c = 0.55\,\mathrm{m}$, giving:[10]

$$p^* = \frac{q^*}{b_c} = \frac{77.52\,\mathrm{kN/m}}{0.55\,\mathrm{m}} = 140.95\,\mathrm{kN/m^2}.$$

To maintain loading conditions consistent with the analytical calculation according to EN 1993, the self-weight of the steelwork was also included in the equivalent line load q^* and applied, together with the other Stage-I actions, to the upper surface of the top flange. No additional gravity action associated with the element mass was therefore activated in the numerical model, thereby avoiding duplication of self-weight.[11]

11.2. Boundary conditions

The model is defined in the global Cartesian coordinate system of LUSAS, in which the Y axis is vertical, the Z axis coincides with the longitudinal axis of the girder, and the X axis is normal to the web midsurface. The corresponding nodal translations are denoted by U_X, U_Y and U_Z, while the nodal rotations are denoted by R_X, R_Y and R_Z.

At the girder ends, kinematic conditions corresponding to a simply supported arrangement were assigned using *Support* attributes. At one end, the `Fixed Bearing` attribute was applied, defined by:

$$U_X = U_Y = U_Z = 0, \qquad R_X,\ R_Y,\ R_Z \text{ libere.}$$

At the opposite end, the `Rolling Bearing` attribute was applied, for which:

$$U_X = U_Y = 0, \qquad U_Z \text{ libera}, \qquad R_X,\ R_Y,\ R_Z \text{ libere.}$$

The first condition eliminates global rigid-body translations of the model, while the second provides vertical and lateral support while leaving the longitudinal translation of the girder along Z free.

The intermediate torsional restraints were modelled so as to reproduce, in global terms, a "fork" restraint condition: they prevent lateral displacement of the shear centre and torsional rotation of the cross-section, while

[10] For the erection stage, a uniformly distributed construction load of $q_k = 2.50\,\mathrm{kN/m^2}$ was adopted, representing the simultaneous presence of workers, tools and site materials. This value is a conservative design assumption consistent with the general criteria of EN 1991-1-6 (*Eurocode 1 – Actions on structures – Part 1-6: General actions – Actions during execution*), to which EN 1993-1-1 refers for the definition of actions to be considered during construction stages.

[11] The load was entered in LUSAS using the "Globa Distributed" dialogue (3D analysis category), with "Per unit area" selected in the Y direction, which was taken as the vertical axis. The model default units were kN and m. Input value: -140.95.

leaving warping free. For this purpose, 11 restraint sections, including the two end sections, were defined at the coordinates:

$$z_j = jL_b, \qquad j = 0, \ldots, 10, \qquad L_b = 4800\,\mathrm{mm}.$$

The girder, of length $L = 48000\,\mathrm{mm}$, is therefore divided into 10 equal lateral-torsional buckling segments.

At each section, an auxiliary geometric point was introduced at the shear centre S. These points do not belong to the midsurface of the shell elements, but are used as kinematic control points. By means of the support attribute named `LTB torsionale restraint - RX` in the model, the global translation normal to the web plane was restrained at S:

$$U_X(S) = 0.$$

The attribute name is an identifier assigned within the model; the translational degree of freedom affected by the restraint is U_X.

Note on the adopted boundary conditions

The particular arrangement of intermediate restraints was adopted specifically to make the numerical model kinematically comparable both with the analytical model used to determine the elastic critical moment M_{cr} according to EN 1993 and with the one-dimensional LTBeamN model. The restraints were therefore configured to prevent lateral translation and global torsional rotation of the cross-section at the selected sections, while leaving the longitudinal deformation associated with warping free. This arrangement is not intended to reproduce a particular real construction detail, but rather to represent, within the shell-element model, the ideal boundary conditions underlying the EN 1993 analytical formulations and the beam-element idealisation adopted in LTBeamN. The correspondence between the kinematic conditions of the three models therefore permits direct comparison of their critical multipliers and global mode shapes, allowing any differences to be attributed to the different levels of discretisation and structural representation rather than to non-equivalent boundary conditions.

Displacement Control kinematic constraints were then applied, whereby only the lateral component U_X of the selected nodes was associated with the corresponding control section. These constraints do not impose compatibility of the longitudinal translations U_Z and do not directly restrain the rotational degrees of freedom of the shell elements.

The fork restraint condition was completed using the *Displacement Control* named `DC_X_all_riTors`, assigned to the nodes along the centreline of the top flange at the same restraint sections. The global translation U_X was prevented for these nodes. The combination of the two lateral constraints, applied at the shear centre and at the top flange respectively, prevents both lateral translation of the cross-section and its torsional rotation about the longitudinal Z axis in global terms:

$$\begin{aligned} U_X(S) &= 0, \\ U_X(\text{piattabanda superiore}) &= 0, \end{aligned} \qquad \Longrightarrow \qquad \begin{aligned} v &= 0, \\ \theta_Z &= 0. \end{aligned}$$

As no rigid longitudinal compatibility was imposed between the nodes of the cross-section, the translations U_Z remain independent and the section can develop the differential longitudinal displacements associated with warping. The restraint system therefore reproduces a discrete fork-type torsional restraint without introducing an infinitely rigid transverse diaphragm and without directly restraining warping.

11.3. First-order linear buckling analysis

The global critical mode was first identified by means of a linear eigenvalue buckling analysis. This procedure assumes that, before buckling, the elastic stiffness matrix remains unchanged, the geometric stiffness matrix is proportional to the load level, and the pre-buckling displacements do not significantly alter the structural response. The reference stress state was obtained from a preliminary first-order linear static analysis governed by the equation:

$$\mathbf{K}\mathbf{a}^{(0)} = \mathbf{R},$$

where $\mathbf{K}$ is the elastic stiffness matrix of the structure, $\mathbf{a}^{(0)}$ is the displacement vector associated with the reference load, and $\mathbf{R}$ is the corresponding vector of equivalent nodal loads. The geometric stiffness matrix, or initial-stress matrix, $\mathbf{K}_\sigma^{(0)}$, is constructed from the stress state thus determined.

The linear buckling problem is therefore reduced to the generalised eigenvalue problem (30):

$$\left(\mathbf{K} + \mu_i \mathbf{K}_\sigma^{(0)}\right) \boldsymbol{\Phi}_i = \mathbf{0},$$

in which μ_i is the ith critical multiplier and $\boldsymbol{\Phi}_i$ the corresponding mode shape. The vector of critical loads associated with mode i is therefore:

$$\mathbf{R}_{\mathrm{cr},i} = \mu_i \mathbf{R}.$$

Similarly, denoting by $M_{\mathrm{ref}}(x)$ the bending-moment diagram produced by the reference load system, the corresponding elastic critical diagram is:

$$M_{\mathrm{cr},i}(x) = \mu_i M_{\mathrm{ref}}(x).$$

In the shell-element model, the eigenvalue ordering does not distinguish a priori between the different buckling phenomena: the first extracted modes may therefore represent local buckling of the web, flanges or stiffeners, or distortional modes of the cross-section. Consequently, the first eigenvalue of the system does not necessarily coincide with the first global lateral-torsional buckling mode of the girder. In the FEM model, solely for the purpose of identifying the global mode shape, these local phenomena were controlled through suitable

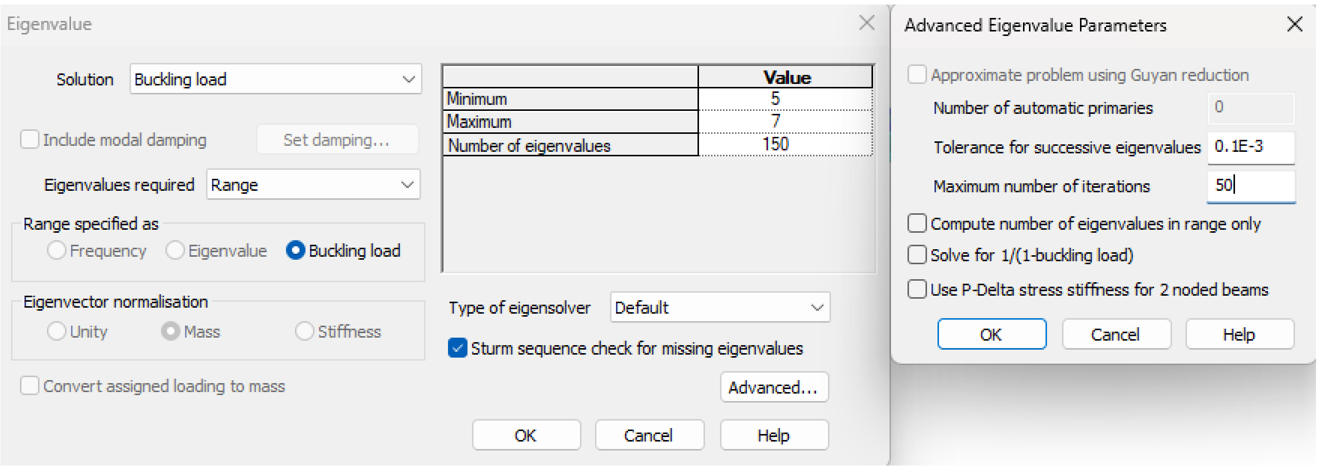

Figure 23. *LUSAS* Linear Buckling *solver settings. The* load factor *search interval was deliberately defined to exclude from extraction and interpretation the multipliers associated with local, distortional or highly localised buckling modes, thereby focusing the analysis on global buckling modes of the compressed top flange. The* Sturm sequence check *option was activated to verify that no eigenvalue was omitted by the extraction procedure within the assigned search interval. The check compares the number of eigenvalues identified by Sturm counting with those actually extracted by the solver, thereby indicating any missing modes.*

discretisation and by introducing the stiffeners and kinematic conditions specified at the restraint sections. The modes associated with the lower eigenvalues were then examined and classified according to their deformed shapes, excluding those characterised mainly by local plate buckling and lacking global participation of the compressed top flange.

The preliminary estimate provided by the approximate formulation allowed the search for the first relevant global mode to be restricted to the following interval (global buckling of the compressed top flange):

$$6 \lesssim \mu_i \lesssim 7.$$

Within this interval, the first deformed shape characterised by an overall lateral displacement of the compressed top flange, accompanied by torsional rotation of the cross-sections and by a longitudinal response consistent with a global lateral-torsional buckling mode, was identified. The corresponding elastic critical multiplier is approximately:

$$\boxed{\mu_{\mathrm{cr,LTB}}^{\mathrm{LUSAS,\,beam}} \simeq 6.740}.$$

It follows that the critical load system and bending-moment diagram associated with this mode may be expressed as:

$$\mathbf{R}_{\mathrm{cr,LTB}} \simeq 6.74\,\mathbf{R}, \qquad M_{\mathrm{cr,LTB}}(x) \simeq 6.74\,M_{\mathrm{ref}}(x).$$

The value $\mu_{\mathrm{cr,LTB}}^{\mathrm{LUSAS,\,beam}}$ is an elastic critical multiplier referred to the geometrically perfect model and linear material behaviour. It does not therefore represent a design resistance and does not include the effects of geometric imperfections, residual stresses, material yielding or partial safety factors.

The mode shapes $\mathbf{\Phi}_i$ are also defined only up to an arbitrary multiplying factor and are normalised by the solver solely for graphical representation. The displayed amplitude therefore has no direct physical meaning: for identification of the phenomenon, the significant features are the shape of the deformation, the relative participation of the various structural components and the corresponding eigenvalue.

The representations in Fig. 24 compare the global mode shape obtained from the three-dimensional shell-element model developed in LUSAS with that obtained using LTBeamN, which is based on a one-dimensional beam-element idealisation.

The deformed shapes of the compressed top flange are substantially consistent, with the same number of half-waves and similar positions of the modal nodes along the girder. This correspondence indicates that the two eigenvalues identify the same global lateral-torsional buckling mode. The LUSAS model nevertheless shows additional local and distortional components of the plates and stiffeners that cannot be represented by the one-dimensional model adopted in LTBeamN.

The amplitudes shown in the figures are not directly comparable because the eigenvectors are normalised and their graphical scale is arbitrary. The comparison must therefore be based on the mode shape, the position of the nodes and the value of the critical multiplier. LUSAS gives $\mu_{\mathrm{cr,LTB}}^{\mathrm{LUSAS,\,beam}} = 6.740$, whereas LTBeamN gives $\mu_{\mathrm{cr,LTB}}^{\mathrm{LTBeamN,\,beam}} = 6.541$, corresponding to a relative difference of approximately 3.04%. The good modal and numerical agreement confirms that the restraints introduced in the three-dimensional model adequately reproduce those assumed in the beam model. The slightly higher value obtained with LUSAS is compatible with the explicit representation of the geometry, stiffeners and distributed sectional stiffnesses.

Overall, the comparison provides an independent confirmation of the identification of the first global lateral-torsional buckling mode.

Absolute displacement output is not available in eigenvalue analyses. The displacement results (Fig. 24a) are nevertheless provided in normalised form. In buckling analyses, the eigenvectors, i.e. the mode shapes,

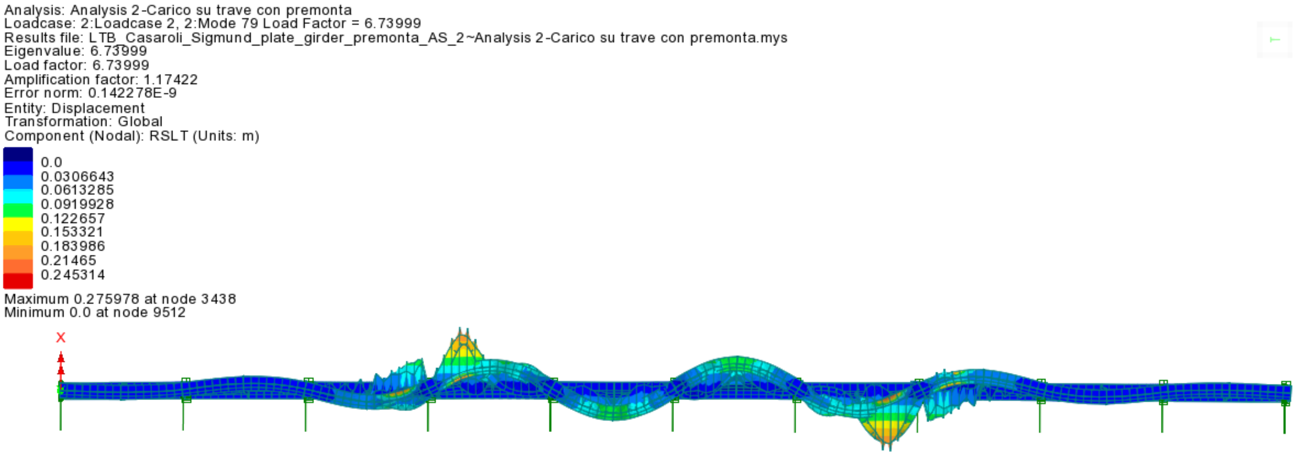

(a) *Overall view of the modal deformation of the compressed top flange according to LUSAS: plan view of the compressed top flange.*

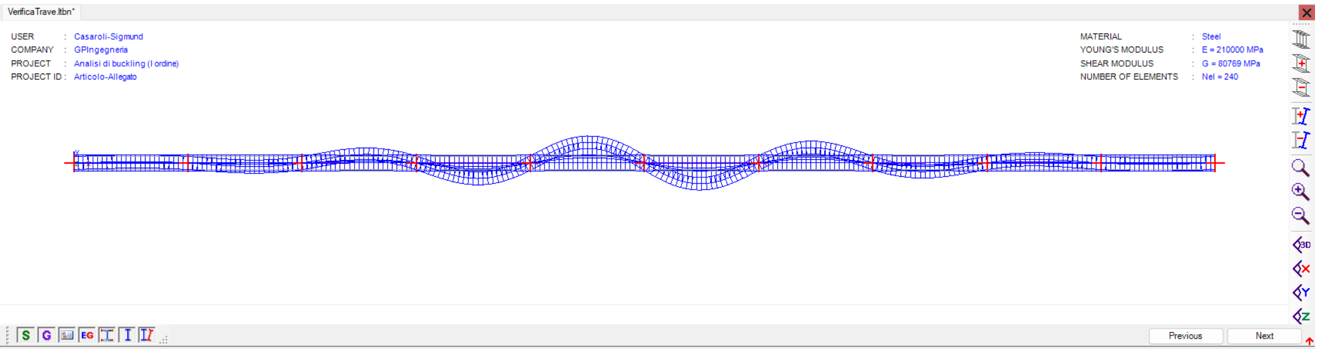

(b) *Representation of the lateral deformation of the compressed top flange according to LTBeamN: plan view of the compressed top flange.*

Figure 24. *First global mode shape (QSL8 shell elements) associated with lateral-torsional buckling of the girder, identified by the linear eigenvalue analysis for a critical multiplier* $\mu_{\mathrm{cr,LTB}}^{\mathrm{LUSAS,\,beam}} \simeq 6.740$. *Mode shape from the LTBeamN "beam" model with critical multiplier (linear analysis)* $\mu_{\mathrm{cr,LTB}}^{\mathrm{LTBeamN,\,beam}} = 6.541$.

are normalised to unity; it should be noted that mass normalisation is supported only in eigenvalue analyses for the determination of natural frequencies. Although the mode shapes correctly represent the relative deformation pattern at the onset of buckling, they do not quantitatively define the displacements or stresses in the structure at the critical load.

11.4. Preliminary comparisons between LUSAS, LTBeamN and EN 1993 results

For the same cross-section type, boundary conditions and loading conditions, application of the rigorous EN 1993 formulations gave the following elastic critical moment (first-order theory; see the preceding sections):

$$M_{cr}^{\mathrm{EC3}} = 133626\,\mathrm{kNm}$$

Therefore, under the EN 1993 formulations, for a maximum equivalent design moment of $M_{Ed} = 22325\,\mathrm{kNm}$, the critical multiplier is:

$$\mu_{\mathrm{cr,LTB}}^{\mathrm{EN\,1993,\,beam}} = \frac{M_{cr}^{\mathrm{EC3}}}{M_{Ed}} = \frac{133626}{22325} = 5.985$$

LTBeamN assesses lateral-torsional buckling by means of a one-dimensional beam-element model in which the global girder behaviour is described through equivalent sectional properties.

This idealisation does not explicitly represent the local and distortional deformations of the individual plates, which may instead emerge in a three-dimensional shell-element model. The elastic critical moment obtained using LTBeamN is:

$$M_{cr}^{\mathrm{LTBeamN}} = 146022\,\mathrm{kNm},$$

$$\mu_{\mathrm{cr,LTB}}^{\mathrm{LTBeamN,\,beam}} = \frac{M_{cr}^{\mathrm{LTBeamN}}}{M_{Ed}} = \frac{146022}{22325} = 6.541.$$

Calculation	Critical multiplier μ_{cr}	Difference from EN 1993
LUSAS	6.740	+12.61%
LTBeamN	6.541	+9.29%
EN 1993	5.985	–

Table 8. *Comparison of the elastic critical multipliers obtained using LUSAS, LTBeamN and the EN 1993 formulation. Percentage differences are calculated taking the EN 1993 value as the reference. LTBeamN analyses lateral-torsional buckling using a model consisting of one-dimensional beam elements.*

The ordering of the various critical multipliers (for global buckling of the compressed top flange):

$$\mu_{\mathrm{cr,LTB}}^{\mathrm{LUSAS,\,beam}} > \mu_{\mathrm{cr,LTB}}^{\mathrm{LTBeamN,\,beam}} > \mu_{\mathrm{cr,LTB}}^{\mathrm{EN\,1993,\,beam}}$$

is consistent, for the case examined, with the progressive degree of model idealisation: LUSAS explicitly represents the three-dimensional geometry of the girder and stiffeners using shell elements, whereas LTBeamN adopts a one-dimensional beam-element model; the EN 1993 formulation finally provides a more idealised analytical assessment and, in the case considered, a more conservative one.

The approximate procedure does not directly return an elastic critical multiplier comparable with the preceding values, but estimates an intentionally conservative design resistance (up to a maximum of 20% greater conservatism for cross-sections belonging to "less frequent" families); this conservative character is confirmed by the higher utilisation ratio compared with that obtained using the complete EN 1993 procedure.

12. Checks on elastic buckling analyses with discrete perfect lateral-torsional restraints

This section establishes the reference level for the subsequent analysis of the twin-girder system. First, the consistency of the elastic critical multipliers obtained for the single girder using LUSAS, LTBeamN and the EN 1993 formulation is verified; the elastic result is then converted into the corresponding design resistance using the code procedure. The manual calculation therefore does not constitute an independent or off-topic investigation with respect to the FEM study, but completes the validation of the single-girder model and defines the reference for the nonlinear analyses of the complete structural system.

The distinction between these two modelling levels is essential: the first concerns a single member between ideal lateral-torsional restraints, whereas the second concerns the two girders connected by diaphragms and allows global modes of the entire deck. The results are therefore related without superimposing their respective kinematic and resistance assumptions.

12.1. Identification of critical multipliers for global buckling

Identifying the critical multiplier associated with global lateral-torsional buckling can be particularly delicate in three-dimensional shell-element models. In such models, the first eigenvalues do not necessarily correspond to the global mode sought, because they may be preceded by local buckling of the web, flanges or stiffeners, as well as by distortional or mixed modes. Consequently, the first eigenvalue extracted by the solver must not automatically be assumed to represent global buckling of the girder; rather, a sufficiently large number of mode shapes must be examined and the mode characterised by consistent lateral displacement and torsional rotation of the compressed part of the cross-section must be identified, with particular reference to the top flange during the construction stage before composite action with the slab is established.

The comparison shows that, once kinematically equivalent modes have been identified, the results obtained using LUSAS, LTBeamN and the EN 1993 formulation exhibit satisfactory consistency. The remaining differences are attributable to the different levels of idealisation: the shell model explicitly represents geometry, stiffeners and local deformations; LTBeamN describes global behaviour using one-dimensional beam elements; and the EN 1993 formulation reduces the problem to equivalent sectional properties, moment coefficients and ideal boundary and warping conditions.

Note on restraint boundary conditions

In the specific case analysed, the results obtained using LTBeamN and LUSAS (see Table 8) are nearly coincident for the configuration with ideal discrete lateral restraints, in which translation of the girder in the direction normal to its longitudinal axis is prevented. This configuration differs from the system comprising two girders connected by transverse diaphragms, because the diaphragms mainly impose relative constraints between the two girders without necessarily preventing global lateral displacement of the entire deck. Consequently, the close agreement between the two models observed in the present study cannot automatically be extended to different structural configurations, in which the effectiveness of the lateral restraints depends on the interaction between the girders and on diaphragm stiffness.

The comparison of elastic critical multipliers validates the identification of the global mode, but does not yet provide an ultimate limit state verification. To complete the comparison, the elastic result must therefore be converted into a design resistance according to EN 1993, while retaining the same assumptions of a single girder and ideal restraints.

12.2. Manual EN 1993 verification of cross-section P1 and definition of the resistance reference

The following calculation applies the complete EN 1993 lateral-torsional buckling verification chain to the reference cross-section P1. It constitutes the resistance-level completion of the elastic checks developed in the preceding subsection: it is therefore not a self-contained example, but defines the reference against which the results subsequently obtained using LTBeamN, the approximate parametric procedure and the FEM analyses are compared.

The approximate procedure developed in the preceding sections must not be interpreted as a direct replacement for elastic buckling analysis or as an elementary procedure with no intermediate steps. Its application requires the determination of dimensionless geometric parameters, the reading of the various operational charts and, where the representative point does not coincide with one of the plotted curves, one or more linear interpolations. Its practical advantage therefore lies not in eliminating all numerical processing, but in avoiding the explicit determination of the elastic critical moment M_{cr} and the subsequent code-based conversion of this quantity into design resistance.

The difference between the two routes may be represented schematically as shown in Fig. 25. The initial

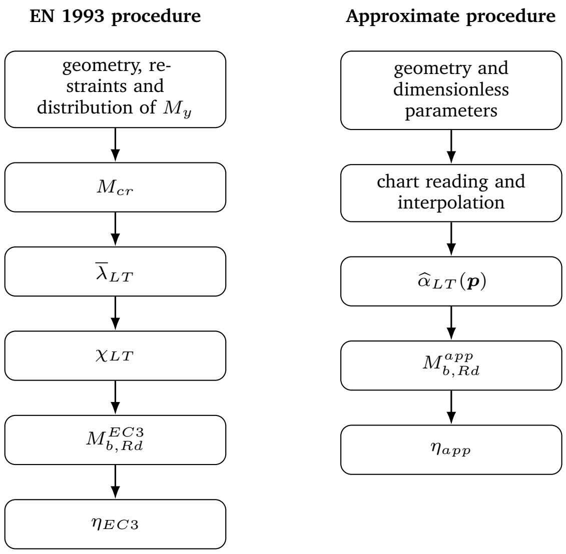

Figure 25. *Comparison between the EN 1993 verification route and the approximate procedure. The latter avoids explicit determination of M_{cr} and the subsequent $\overline{\lambda}_{LT}$–χ_{LT} chain.*

datum is the elastic critical multiplier obtained from a linear eigenvalue analysis:

$$\alpha_{cr,op} = \frac{F_{cr}}{F_{Ed}}, \tag{69}$$

where F_{Ed} denotes, in general terms, the level of the design actions used as the reference configuration and F_{cr} the corresponding elastic critical level. For a system in which the actions are increased proportionally, the same ratio may be expressed in terms of moment:

$$\alpha_{cr,op} = \frac{M_{cr}}{M_{Ed}}. \tag{70}$$

The second parameter of interest is the characteristic multiplier associated with attainment of the cross-section resistance, denoted by $\alpha_{ult,k}$. For a member subjected predominantly to bending, it may be written as:

$$\alpha_{ult,k} = \frac{M_{y,Rk}}{M_{Ed}}, \tag{71}$$

where:

$$M_{y,Rk} = W_y f_y. \tag{72}$$

For a Class 4 cross-section, such as the P1 cross-section considered in the present study, the effective section modulus must be used:

$$M_{y,Rk} = W_{y,\mathrm{eff}} f_y. \tag{73}$$

The preceding relationship is consistent with the EN 1993-1-1 approach to determining the resistance of Class 4 cross-sections and with the subsequent use of the effective resistance in the lateral-torsional buckling verification.

The ratio between the cross-section resistance multiplier and the elastic critical multiplier gives the operational slenderness:

$$\overline{\lambda}_{op} = \sqrt{\frac{\alpha_{ult,k}}{\alpha_{cr,op}}}. \tag{74}$$

Substitution of Eqs. (70) and (71) gives:

$$\overline{\lambda}_{op} = \sqrt{\frac{M_{y,Rk}}{M_{cr}}}, \tag{75}$$

which, for lateral-torsional buckling verification, coincides with the definition of the non-dimensional slenderness:

$$\overline{\lambda}_{LT} = \sqrt{\frac{W_y f_y}{M_{cr}}}, \tag{76}$$

using $W_{y,\mathrm{eff}}$ for Class 4 cross-sections. This is the approach specified in EN 1993-1-1, § 6.3.2.2, for the lateral-torsional buckling verification of members.

The reduction factor is then determined using the usual buckling-curve expression. For lateral-torsional buckling:

$$\Phi_{LT} = \frac{1}{2}\left[1 + \alpha_{LT}\left(\overline{\lambda}_{LT} - \overline{\lambda}_{LT,0}\right) + \overline{\lambda}_{LT}^2\right], \tag{77}$$

and:

$$\chi_{LT} = \min\left\{1; \frac{1}{\Phi_{LT} + \sqrt{\Phi_{LT}^2 - \overline{\lambda}_{LT}^2}}\right\}. \tag{78}$$

In the general form of EN 1993-1-1:

$$\overline{\lambda}_{LT,0} = 0.20, \tag{79}$$

whereas the imperfection factor α_{LT} must be selected from the relevant lateral-torsional buckling curve in accordance with Tables 6.3 and 6.4 of EN 1993-1-1. For welded sections, the value cannot be assumed generically, but depends on the cross-section geometry and, in particular, on the ratio of web depth to compressed-flange width.

The reduction factor χ associated with flexural buckling is then calculated:

$$\Phi = \frac{1}{2}\left[1 + \alpha\left(\overline{\lambda} - 0.20\right) + \overline{\lambda}^2\right], \tag{80}$$

$$\chi = \min\left\{1; \frac{1}{\Phi + \sqrt{\Phi^2 - \overline{\lambda}^2}}\right\}, \tag{81}$$

with the imperfection factor α obtained from Tables 6.1 and 6.2 of EN 1993-1-1, in accordance with

§ 6.3.1.2. The following operational expression is therefore adopted:

$$\chi_{op} = \min\left(\chi, \chi_{LT}\right). \tag{82}$$

This choice represents a conservative rule and must not be generalised independently of the structural problem. For cross-section P1, subject to lateral-torsional buckling verification in bending, the relevant factor is χ_{LT}; any flexural buckling verification must be carried out separately using its own slenderness and the corresponding curve.

The design resistance multiplier relative to the load level adopted in the analysis is finally:

$$\alpha_{Rd,op} = \frac{\chi_{op}\alpha_{ult,k}}{\gamma_{M1}}, \tag{83}$$

or, for lateral-torsional buckling alone:

$$\alpha_{b,Rd} = \frac{\chi_{LT}\alpha_{ult,k}}{\gamma_{M1}}. \tag{84}$$

The verification is satisfied when:

$$\alpha_{b,Rd} \geq 1. \tag{85}$$

The same condition may be expressed using the design resistance moment:

$$M_{b,Rd} = \chi_{LT}\frac{W_{y,\mathrm{eff}}f_y}{\gamma_{M1}}, \tag{86}$$

and the utilisation ratio:

$$\eta_{LT} = \frac{M_{Ed}}{M_{b,Rd}} = \frac{1}{\alpha_{b,Rd}} \leq 1. \tag{87}$$

For cross-section P1, the values already determined in the preceding sections are:

$$\begin{aligned} W_{y,\mathrm{eff}} &= 67955139\,\mathrm{mm}^3, \\ f_y &= 335\,\mathrm{MPa}, \\ M_{Ed} &= 22312.34\,\mathrm{kNm}, \\ \gamma_{M1} &= 1.10. \end{aligned}$$

It follows that:

$$\begin{aligned} M_{y,Rk} &= W_{y,\mathrm{eff}}f_y \\ &= 67955139 \cdot 335 \\ &= 22764.97\,\mathrm{kNm}, \end{aligned}$$

and:

$$\begin{aligned} \alpha_{ult,k} &= \frac{M_{y,Rk}}{M_{Ed}} \\ &= \frac{22764.97}{22312.34} \\ &= 1.0203. \end{aligned}$$

Adopting the critical multiplier already determined using the complete EN 1993 formulation:

$$\alpha_{cr}^{EC3} = 5.985,$$

which gives:

$$\begin{aligned} \overline{\lambda}_{LT}^{EC3} &= \sqrt{\frac{1.0203}{5.985}} \\ &= 0.413. \end{aligned}$$

For the buckling curve previously identified in the complete verification, characterised by:

$$\alpha_{LT} = 0.76,$$

the corresponding values are:

$$\begin{aligned} \Phi_{LT}^{EC3} &= \frac{1}{2}\left[1 + 0.76(0.413 - 0.20) + 0.413^2\right] \\ &= 0.666, \end{aligned}$$

$$\begin{aligned} \chi_{LT}^{EC3} &= \frac{1}{0.666 + \sqrt{0.666^2 - 0.413^2}} \\ &= 0.841. \end{aligned}$$

The design resistance multiplier is therefore:

$$\begin{aligned} \alpha_{b,Rd}^{EC3} &= \frac{0.841 \cdot 1.0203}{1.10} \\ &= 0.780 < 1, \end{aligned}$$

which is equivalent to:

$$\begin{aligned} \eta_{LT}^{EC3} &= \frac{1}{0.780} \\ &= 1.282 > 1. \end{aligned}$$

The manual calculation therefore shows that the single girder does not satisfy the verification in the assumed configuration, since:

$$\alpha_{b,Rd}^{EC3} = 0.780 < 1, \qquad \eta_{LT}^{EC3} = 1.282 > 1.$$

This result constitutes the resistance reference for the subsequent discussion. It must not be compared directly with the elastic critical multipliers alone obtained using LTBeamN or LUSAS, because these describe the elastic bifurcation problem. It must instead be compared with the corresponding design resistances, obtained by applying the same reduction curve and the same partial safety factor to the lateral-torsional slenderness. The above sequence ensures that the elastic multiplier obtained from the closed-form formulation or an eigenvalue analysis is first converted into slenderness and subsequently into design resistance.

Keeping the resistance model, effective cross-section properties, buckling curve and partial factor γ_{M1} unchanged, the critical multiplier obtained from the EN 1993 formulation is now replaced by that derived from the elastic LTBeamN analysis. The comparison therefore isolates the effect of the different evaluation of the elastic critical moment. Using the result obtained from LTBeamN under the same assumptions of a single girder and ideal torsional restraints:

$$\alpha_{cr}^{LTBeamN} = 6.541,$$

the following values are obtained analogously:

$$\overline{\lambda}_{LT}^{LTBeamN} = 0.395,$$
$$\chi_{LT}^{LTBeamN} = 0.854,$$
$$\alpha_{b,Rd}^{LTBeamN} = 0.792,$$
$$\eta_{LT}^{LTBeamN} = 1.262.$$

The small difference from the EN 1993 verification derives from the different value of the elastic critical moment, while the resistance model, buckling curve and effective cross-section properties remain unchanged.

The approximate parametric procedure is then applied to the same cross-section and the same design demand. Unlike the EN 1993–LTBeamN route, it does not explicitly determine M_{cr}, $\overline{\lambda}_{LT}$ and χ_{LT}, but directly returns a conservative estimate of $M_{b,Rd}$. The comparison must therefore be made between design resistances or between the corresponding utilisation ratios. The approximate procedure eliminates the complete sequence:

$$M_{cr} \longrightarrow \overline{\lambda}_{LT} \longrightarrow \chi_{LT} \longrightarrow M_{b,Rd},$$

and directly provides the estimate:

$$M_{b,Rd}^{app} = \frac{A_c^2}{\gamma_{\text{suppl}}\widehat{\alpha}_{LT}(\boldsymbol{p})L_b}, \tag{88}$$

where:

$$A_c = b_c t_c, \tag{89}$$

where $\widehat{\alpha}_{LT}(\boldsymbol{p})$ is obtained using the relationships and charts developed in the preceding sections. The verification may be expressed as:

$$M_{Ed} \leq M_{b,Rd}^{app}, \tag{90}$$

or by means of:

$$\eta_{app} = \frac{M_{Ed}}{M_{b,Rd}^{app}} = \frac{\gamma_{\text{suppl}}\widehat{\alpha}_{LT}(\boldsymbol{p})M_{Ed}L_b}{A_c^2} \leq 1. \tag{91}$$

The approximate procedure nevertheless retains a non-negligible degree of complexity, because the value of $\widehat{\alpha}_{LT}(\boldsymbol{p})$ requires correct identification of the applicable domain, reading of the charts and the corresponding interpolations. Its usefulness lies in making the calculation depend mainly on the geometric parameters of the compressed flange and on the unrestrained torsional length, without requiring a new determination of the torsional and warping properties, equivalent coefficients and elastic critical moment whenever the cross-section is modified. This is particularly useful for preliminary sizing and iterative comparison of alternative configurations, provided that the static scheme, geometric range and boundary conditions adopted in the calibration are respected.

Finally, this treatment must be kept distinct from the nonlinear analyses of the complete bridge-girder system. The EN 1993 verification, the LTBeamN calculation and the approximate procedure previously applied to cross-section P1 refer to a single girder between two ideal torsional restraints, with:

$$L_b = 4.80\,\mathrm{m}.$$

The three-dimensional model of the two girders connected by diaphragms instead permits lateral and torsional deformation of the entire system, including in-phase lateral sway of the two girders. Its first buckling multiplier, of the order of $1.5 \div 1.6$, is therefore associated with a global mode and with boundary conditions different from those adopted for the verification of the single member.

For this particular twin-girder deck, direct substitution of this multiplier into the chain of Eqs. (74)–(87) would formally produce a very low reduction factor and would not constitute a consistent verification of the single girder according to the model assumed by the approximate procedure. The global multiplier must be interpreted within the twin-girder model and investigated through geometrically nonlinear or geometrically and materially nonlinear analyses, with imperfections compatible with the identified global modes.

The two levels of analysis therefore provide complementary information: the approximate procedure and the EN 1993 verification assess the lateral-torsional resistance of the individual member under the assumed restraint conditions, whereas the GNIA and GMNIA analyses examine the stability and capacity of the actual three-dimensional system modelled. The approximate procedure retains its usefulness in the first context, particularly for preliminary sizing and rapid comparison of cross-sections, without being extended to global configurations outside its calibration range.

Link to the subsequent analyses. The result just obtained refers to the single girder and to the "perfect" lateral-torsional boundary conditions assumed in the member verification. The subsequent GNIA and GMNIA analyses of the twin-girder system with diaphragms represent a different structural problem and do not constitute a direct replacement of the critical multiplier in the present EN 1993 chain. The comparison between the two modelling levels is therefore made in terms of global behaviour and resistance margin, while keeping their respective kinematic assumptions distinct.

13. Buckling analysis of the twin-girder system connected by diaphragms

13.1. Introduction

The preceding section analysed the behaviour of a single girder provided with ideal lateral-torsional restraints, modelled by imposing zero lateral displacement at the restraint sections. This configuration provides a useful theoretical reference for validating the numerical model because it reproduces the kinematic conditions commonly assumed in classical lateral-torsional buckling formulations.

In practical bridge-deck design, however, the main girders are generally connected by transverse diaphragms, which do not constitute absolute lateral restraints in the strict sense. They ensure kinematic compatibility between the girders and transfer transverse actions, while still allowing lateral displacement of the entire structural system. Consequently, the unrestrained buckling length does not necessarily coincide with the spacing between consecutive diaphragms, but depends on the global behaviour of the twin-girder system and on the actual stiffness of the transverse connections.

In light of these considerations, the behaviour of a deck comprising two main girders connected by diaphragms is analysed below to assess the influence of connection stiffness on the mode shape, the elastic critical multiplier and the subsequent nonlinear structural response.

To avoid ambiguity with the multipliers previously referred to the single girder, the following convention is adopted hereafter: $\mu_{\mathrm{cr,LTB}}^{(\cdot,\,\mathrm{beam})}$ denotes the elastic critical multiplier of the single-girder model; $\mu_{\mathrm{cr},1}^{\mathrm{LUSAS,\,bibeam}}$ denotes the first elastic critical multiplier of the LUSAS twin-girder model; and $\mu_{\mathrm{u}}^{\mathrm{GNIA}}$ and $\mu_{\mathrm{u}}^{\mathrm{GMNIA}}$ denote the ultimate multipliers obtained from the respective nonlinear analyses. The subscript "cr" is therefore reserved for linear eigenvalue analyses, while the subscript "u" is used for the limit points of nonlinear equilibrium paths.

13.1.1. *Geometric characteristics of the steelwork components*

The steelwork in the model consists of the following components (see Fig. 26):

- **welded monosymmetric I-section main girders**, each comprising:
  - compressed top flange, formed from a plate:
  $$b_c \times t_c = 550\,\mathrm{mm} \times 35\,\mathrm{mm};$$
  - vertical web, formed from a plate of clear depth and thickness:
  $$h_w \times t_w = 2702\,\mathrm{mm} \times 12\,\mathrm{mm};$$
  - tension bottom flange, formed from a plate:
  $$b_t \times t_t = 650\,\mathrm{mm} \times 68\,\mathrm{mm};$$
  - overall cross-section depth:
  $$h = h_w + t_c + t_t = 2805\,\mathrm{mm}.$$
- **longitudinal web stiffeners**, formed from plates:
  $$b_{\mathrm{long}} \times t_{\mathrm{long}} = 150\,\mathrm{mm} \times 10\,\mathrm{mm},$$
  arranged symmetrically on both sides of the web at elevations:
  $$s_{\mathrm{long},1} = 700\,\mathrm{mm}, \qquad s_{\mathrm{long},2} = 1700\,\mathrm{mm},$$
  measured from the soffit of the top flange;
- **transverse web stiffeners**, formed from plates:
  $$b_{\mathrm{st}} \times t_{\mathrm{st}} = 250\,\mathrm{mm} \times 10\,\mathrm{mm},$$
  arranged at a longitudinal spacing of:
  $$p_{\mathrm{st}} = 2415\,\mathrm{mm};$$
- **transverse stiffeners at the supports**, consisting of vertical plates welded to the web and flanges, intended to spread the support reactions and stabilise the end panels;
- **upper diaphragm cross-members**, formed from paired angle sections:
  $$2L\,100 \times 50 \times 8;$$
- **secondary diaphragm members**, formed from paired angle sections:
  $$2L\,120 \times 80 \times 12;$$
- **diagonals of the transverse diaphragms**, formed from paired angle sections:
  $$2L\,150 \times 100 \times 12;$$
- **lower diaphragm cross-members**, formed from paired angle sections:
  $$2L\,200 \times 150 \times 15.$$

13.2. Definition of initial geometric imperfections

Assessment of the resistance of the twin-girder system by geometrically and materially nonlinear analysis with imperfections (GMNIA) requires prior definition of the shape and amplitude of the imperfect initial geometry. Within the European code framework, EN 1993-1-1 governs equivalent global member imperfections, while EN 1993-1-5 addresses imperfections of panels and stiffened elements modelled using two-dimensional elements. prEN 1993-1-14, devoted to design assisted by finite-element analysis, systematises the use of LBA, GNIA and GMNIA and requires the introduced imperfections to be consistent with the relevant buckling modes.

The different imperfection levels are summarised in Table 9.

The code provisions do not, however, provide a specific relationship for determining the amplitude of the global imperfection of a system comprising two main girders connected by transverse diaphragms. In particular, no explicit criterion is defined for deriving an equivalent unrestrained torsional length from the first mode shape of a twin-girder deck, nor is it specified whether the reference should be the diaphragm spacing, the total girder span or a different characteristic length inferred from the modal response of the system.

This gap arises from the nature of the restraint provided by the diaphragms. They limit the relative displacements and rotations of the two girders, but do not necessarily constitute absolute lateral restraints relative to a fixed external reference. Denoting the lateral displacements of the two girders by v_1 and v_2, the diaphragm action tends to impose a relationship of the form:

$$v_1 - v_2 \simeq 0,$$

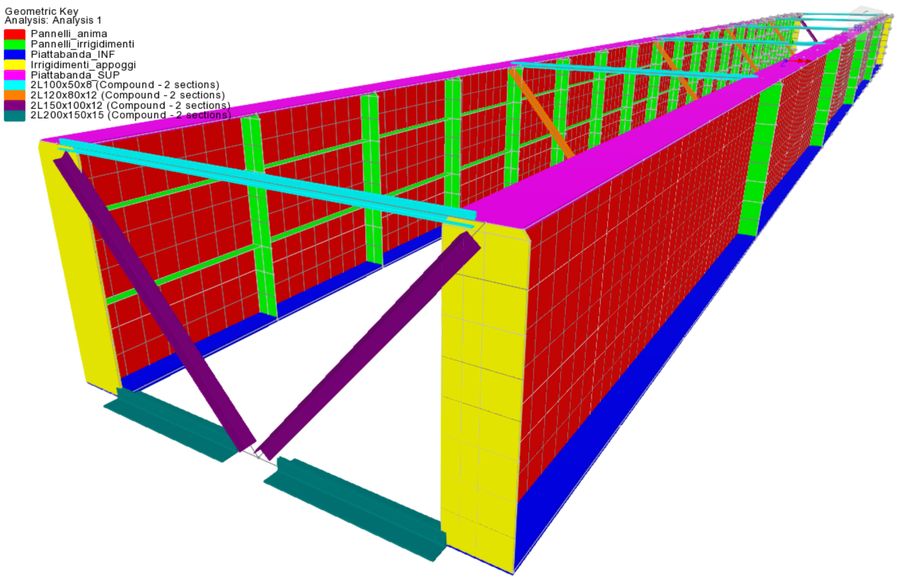

Figure 26. *Axonometric view of the FEM model (Stage-I twin-girder deck) – LUSAS. Supports over a span of* $L = 48.00\,\mathrm{m}$*; diaphragm spacing* $L_b = 9.60\,\mathrm{m}$.

Phenomenon	Reference	General criterion
Global member buckling	EN 1993-1-1	Equivalent imperfection correlated with the buckling curve and member length
Lateral-torsional buckling	EN 1993-1-1	Global shape compatible with the relevant lateral-torsional buckling mode
Local buckling of panels and subpanels	EN 1993-1-5	Local shape consistent with the panel critical mode and amplitude referred to its characteristic dimensions
Advanced numerical analysis	prEN 1993-1-14	Introduction of relevant imperfections in the GMNIA and search for the unfavourable configuration

Table 9. *Main geometric imperfections considered within the scope of Eurocode 3.*

without necessarily requiring:

$$v_1 = v_2 = 0.$$

The system may therefore exhibit in-phase lateral sway of the two girders, accompanied by diaphragm deformation and overall torsion of the deck. For this reason, the geometric spacing of the transverse connections cannot automatically be identified with the unrestrained buckling length of a single girder.

13.3. Settings for nonlinear analyses in LUSAS

The GMNIA was performed using an automatic incremental procedure (*Automatic Increment Control*), in which the software automatically adjusts the load-increment size according to convergence, reducing it near limit points and increasing it during regular response phases, thereby improving both robustness and computational efficiency.

The equilibrium path was traced using arc-length control with the *Relative Displacement Arc-Length Procedure* (Crisfield method), which uses relative displacements rather than the load factor alone as the control parameter. This procedure allows limit points to be crossed automatically and the post-critical response branch, characterised by stiffness loss and a possible descending load–displacement trend, to be followed.

Geometric nonlinearity was treated using a *Total Lagrangian* formulation, in which all kinematic and equilibrium quantities are referred to the initial configuration of the structure. This formulation is particularly suitable for the analysis of large displacements and rotations while retaining the same reference configuration throughout the incremental process. The *Co-rotational Formulation* was also adopted to evaluate the local kinematics of the elements, separating rigid-body motion from actual element deformation. This approach improves the representation of large rotations and allows more accurate evaluation of strains and stresses in geometrically nonlinear analyses.

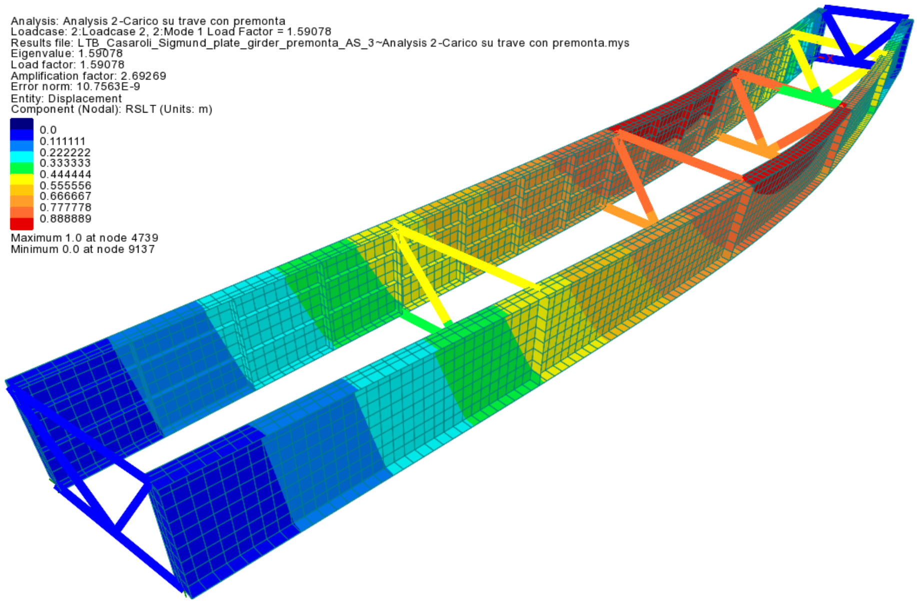

Figure 27. *First mode shape obtained from the linear buckling analysis. First critical multiplier* $\mu_{\mathrm{cr},1}^{\mathrm{LUSAS,\,2girder}} \approx 1.590$ *for Stage-I loads (fresh-concrete casting of the slab).* ***Note:*** *the presence of vertical stiffeners also on the outer face of the web does not alter the value of the first critical multiplier.*

13.4. Criteria for selecting the initial geometric imperfections

In GMNIA, an eigenmode obtained from a linear bifurcation analysis is frequently used as the imperfect initial geometry. The procedure may be expressed as:

$$\mathbf{x}_{\mathrm{imp}} = \mathbf{x}_0 + e_{LT}\widehat{\boldsymbol{\varphi}}_1,$$

where $\mathbf{x}_0$ is the nominal geometry, $\widehat{\boldsymbol{\varphi}}_1$ is the suitably normalised first eigenvector, and e_{LT} is the dimensional multiplier assigned to the mode shape. In the model examined, the first *linear buckling analysis* gave the elastic critical multiplier:

$$\mu_{\mathrm{cr},1}^{\mathrm{LUSAS,\,2girder}} \approx 1.590.$$

The associated mode shape involves both girders and their diaphragms globally, as shown in Fig. 27. The transverse diaphragms are arranged at a spacing of:

$$s_d = 9.60\,\mathrm{m}.$$

In the actual structure, each interval between two consecutive diaphragms is divided into two fields of length:

$$L_p = 4.80\,\mathrm{m},$$

by means of cross-bracing consisting of simple ties, arranged in both the top-flange plane and the bottom-flange plane.

These braces were not included in the FEM model used to determine the critical and ultimate multipliers. The numerical analyses were therefore carried out considering the two main girders and the transverse diaphragms, while neglecting the stabilising contribution of the cross-bracing ties. The geometry of the braced fields was referred to solely to define a plausible amplitude for the equivalent geometric imperfection introduced in the nonlinear analyses, without altering the boundary conditions of the numerical model.

Since the ties cannot be idealised as perfectly rigid lateral-torsional restraints, the geometric length of the individual field was conventionally increased by 25%, taking:

$$L_{b,\mathrm{eff}} = 1.25\,L_p = 1.25 \times 4.80\,\mathrm{m} = 6.00\,\mathrm{m}.$$

The quantity $L_{b,\mathrm{eff}}$ therefore represents a conventional effective length adopted solely to define the imperfection amplitude. It coincides neither with the geometric diaphragm spacing nor with the distance between ideal torsional restraints. The factor 1.25 is a conservative modelling choice and not a value prescribed by the code.

It therefore follows that:

$$e_{LT} = \frac{L_{b,\mathrm{eff}}}{300} = \frac{6000\,\mathrm{mm}}{300} = 20\,\mathrm{mm}.$$

✓ Code note on initial geometric imperfections

EN 1993-1-1, Clause 5.3.2 and Table 5.1, defines equivalent member geometric imperfections through the ratio e_0/L, assigned according to the relevant buckling curve. Selection of the curve does not depend solely on whether the cross-section is welded, but must be made using the specific tables in Chapter 6, considering the cross-section type, buckling axis and flange thicknesses.

For welded I-sections, the flexural buckling curve about the minor axis is generally curve “c” or

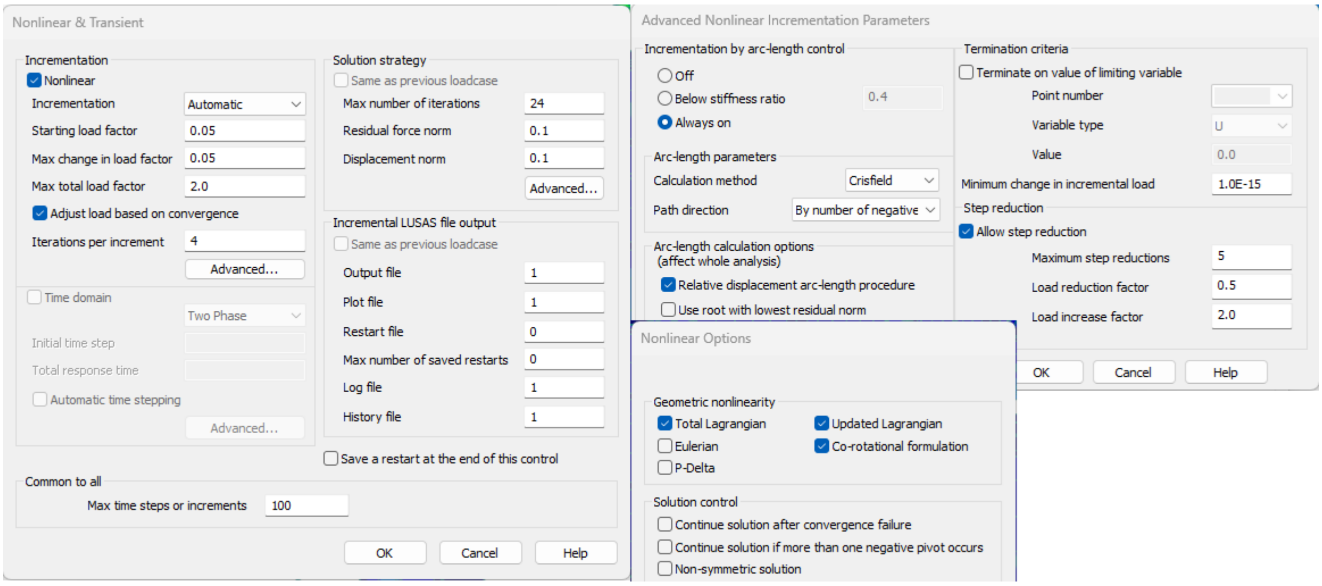

Figure 28. *LUSAS settings adopted for the nonlinear analyses [19].*

continued..

"d", according to Table 6.2 of EN 1993-1-1. For lateral-torsional buckling, Table 6.4 instead assigns curve "c" to welded sections for $h/b \leq 2$ and curve "d" for $h/b > 2$. For cross-section P1, since $h/b_c > 2$, the lateral-torsional buckling verification according to EN 1993 was carried out using curve "d", with $\alpha_{LT} = 0.76$.
The values in Table 5.1 nevertheless concern equivalent imperfections of individual members and do not constitute a specific requirement for GMNIA of twin-girder decks connected by diaphragms. prEN 1993-1-14, devoted to design assisted by finite-element analysis, permits the use of either a sinusoidal shape or a mode shape obtained from a linear buckling analysis as the initial imperfection shape. For lateral-torsional buckling, Clause 5.4.4, Formula (5.16) and Table 5.5 define the equivalent imperfection amplitude using the imperfection factor for flexural buckling about the minor axis and the reference coefficient β_{LT}. The length may be referred to the distance between intermediate restraints only where these can be regarded as sufficiently rigid.
In the present case, the FEM model used to calculate the multipliers does not include the cross-bracing ties present in the actual structure and therefore cannot be treated as a member with perfect lateral-torsional restraints every $4.80\,\mathrm{m}$. The length of the individual braced field was used solely as a geometric reference for defining the initial amplitude. Its 25% increase, through the assumption $L_{b,\mathrm{eff}} = 6.00\,\mathrm{m}$, is an operational criterion adopted by the Authors and not a code provision.

continued..

L'assunzione:

$$e_{LT} = \frac{L_{b,\mathrm{eff}}}{300}$$

must therefore be described as an operational criterion for defining a plausible equivalent geometric imperfection amplitude, rather than as a direct application of buckling curve "a" or an explicit provision of EN 1993-1-1. The value thus determined was used solely to scale the mode shape introduced in the nonlinear analyses, while all critical and ultimate multipliers were calculated using the FEM model without cross-bracing.

✓ *Comparison between the LTBeamN model with ideal restraints and the twin-girder FEM model*

As a further check of the adopted mechanical interpretation, a linear buckling analysis was performed on the single girder using LTBeamN, keeping the member geometry, cross-section properties, load distribution, end conditions and total span of $48.0\,\mathrm{m}$ unchanged. Ideal torsional restraints were introduced in the model at a spacing of:

$$s_d = 9.60\,\mathrm{m},$$

coinciding with the geometric spacing between the transverse diaphragms in the FEM model.
The first critical multiplier obtained using LTBeamN was:

$$\mu_{\mathrm{cr}}^{\mathrm{LTBeamN},\, s_d=9.60\,\mathrm{m}} = 1.872,$$

whereas the LUSAS FEM model, consisting of the continued..

two main girders connected by finite-stiffness transverse diaphragms and without the cross-bracing present in the actual structure, gave:

$$\mu_{\mathrm{cr},1}^{\mathrm{LUSAS,\,2girder}} = 1.590.$$

The reduction in the value obtained using LUSAS relative to the LTBeamN model with ideal restraints is therefore:

$$\Delta\mu_{\mathrm{cr}} = \frac{\mu_{\mathrm{cr}}^{\mathrm{LTBeamN},\,s_d=9.60\,\mathrm{m}} - \mu_{\mathrm{cr},1}^{\mathrm{LUSAS,\,2girder}}}{\mu_{\mathrm{cr}}^{\mathrm{LTBeamN},\,s_d=9.60\,\mathrm{m}}} \times 100$$
$$= \frac{1.872 - 1.590}{1.872} \times 100 = 15.1\%.$$

The two values are of the same order of magnitude, but refer to different mechanical idealisations. In the LTBeamN model, the intermediate restraints ideally prevent torsional rotation of the single girder at the sections where they are applied. In the LUSAS model, by contrast, the diaphragms have finite stiffness and permit deformations and rotations compatible with the global behaviour of the twin-girder system. The critical mode may therefore involve both girders and the transverse connections in phase, without necessarily exhibiting perfect kinematic nodes at the diaphragms.
The lower value returned by LUSAS is therefore consistent with the lower stabilising effectiveness of deformable diaphragms compared with the ideal torsional restraints introduced in LTBeamN. Since the geometry, cross-section properties, load distribution and end conditions were kept consistent, the observed difference may be attributed primarily to the different representation of the lateral-torsional restraint and to the ability of the twin-girder FEM model to develop a global system mode.
The comparison confirms that the diaphragm spacing of $9.60\,\mathrm{m}$ is a significant geometric scale for the buckling phenomenon, but does not justify treating the actual diaphragms as perfectly rigid torsional restraints. It is used as a check on the mechanical consistency of the models and not as a direct procedure for determining the equivalent geometric imperfection amplitude.
Elastic critical multipliers characterise the load level associated with loss of elastic stability of the perfect system, whereas e_{LT} defines the amplitude of the initial geometric perturbation introduced in the nonlinear analyses: the two quantities are conceptually distinct.

The following value is therefore adopted for the non-linear simulations:

$$\boxed{e_{LT} = 20\,\mathrm{mm}.}$$

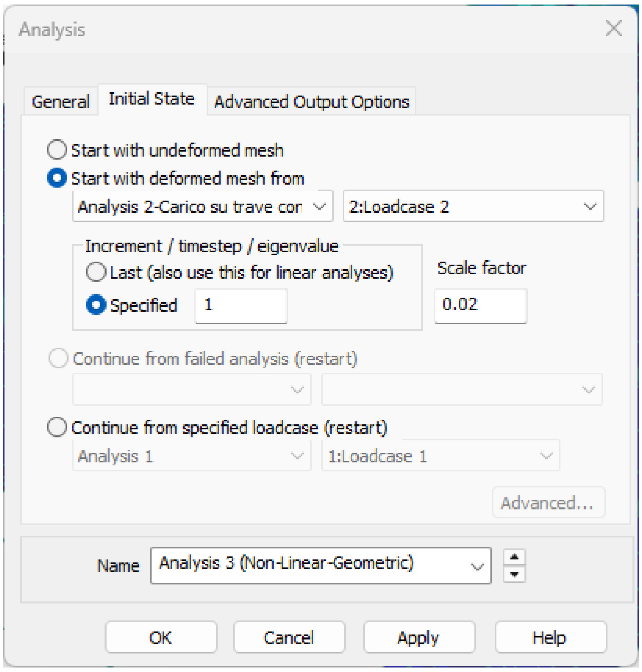

Figure 29. *LUSAS settings for defining imperfections of $e_{LT} = 20\,\mathrm{mm}$ on the first mode shape from the linear buckling analysis.*

Using the full span:

$$L = 48.0\,\mathrm{m},$$

would, for the same ratio, lead to:

$$e_{LT} = \frac{48000\,\mathrm{mm}}{300} = 160\,\mathrm{mm},$$

a value representative of a global out-of-straightness of the entire system, but not consistent with the geometric scale of the braced fields present in the actual structure. Conversely, direct adoption of $L_p = 4.80\,\mathrm{m}$ would be equivalent to assigning the cross-ties the effectiveness of perfectly rigid lateral-torsional restraints. The adoption of $L_{b,\mathrm{eff}} = 6.00\,\mathrm{m}$ therefore constitutes an intermediate and conservative choice, used solely to define the initial imperfection amplitude, without introducing the stabilising contribution of the cross-bracing into the FEM model.

13.5. Geometrically nonlinear analysis with imperfections (GNIA)

The geometrically nonlinear analysis with imperfections (GNIA, *Geometrically Nonlinear Analysis with Imperfections*) was carried out to assess the structural response while accounting for second-order effects and the evolution of the deformed configuration during load application. Unlike linear buckling analysis (LBA), this procedure does not directly return a critical multiplier, but allows the complete equilibrium path of the structure to be followed up to the onset of instability, making it possible to identify the progressive reduction in global stiffness and any development of post-critical behaviour.

In the present study, the analysis was performed using the same three-dimensional model adopted for the preceding linear buckling analysis. The initial geometric configuration was obtained by introducing an equivalent imperfection based on the first buckling mode shape, suitably scaled to the amplitude adopted in the study. This procedure activates the dominant buckling mode from the earliest stages of loading, avoids the use of arbitrary perturbations and improves the numerical robustness of the solution. The load was applied incrementally using automatic convergence control, thereby allowing the evolution of the structural response to be traced even near loss of stability. A geometrically nonlinear *Total Lagrangian* formulation was adopted for the shell elements forming the main girders, while a *Co-rotational* formulation was used for the beam elements modelling the diaphragms (Fig. 28).

The critical load was identified by analysing load–displacement curves obtained at significant points of the structure, with particular attention to the lateral displacements of the compressed flanges in the region of maximum bending demand. The onset of instability was identified through the progressive reduction in tangent stiffness and the consequent departure of the response from linearity, and the results were finally compared with those from the linear buckling analysis.

13.5.1. GNIA results

The subsequent geometrically nonlinear analysis, carried out with the same imperfect shape, gave an ultimate multiplier of approximately $\mu_{\mathrm{u}}^{\mathrm{GNIA}} = 1.495$, corresponding to the following reduction relative to the linear multiplier:

$$\frac{1.590 - 1.495}{1.590} \simeq 6\%.$$

Note. Where vertical stiffeners are also present on the outer face of the web, the corresponding “Load Factor” reaches approximately 1.53. This comparison does not, by itself, constitute a general validation of the adopted amplitude, but shows that the imperfect configuration considered gives a geometrically nonlinear response consistent with the mechanism identified by the bifurcation analysis.

Final verification of the criterion is therefore entrusted to the subsequent GMNIA analyses, in which both geometric nonlinearity and material plasticity are introduced. The reliability of the choice is assessed by a sensitivity analysis with respect to the amplitude e_{LT} and by comparison between:

$$\mu_{\mathrm{cr},1}^{\mathrm{LUSAS,\,2girder}}, \qquad \mu_{\mathrm{u}}^{\mathrm{GNIA}}, \qquad \mu_{\mathrm{u}}^{\mathrm{GMNIA}}.$$

In this way, the value $e_{LT} = 20$ mm is not treated as a code-prescribed datum, but as a physically motivated parameter that is explicitly stated and subjected to numerical verification.

The graph in Fig. 31 shows the variation of the lateral displacement of the midspan control section with the load multiplier obtained from the geometrically nonlinear analysis with imperfections (GNIA). The analysis was carried out by imposing a maximum *Load Factor* of 2.0; however, the incremental procedure stops automatically at the value

$$\mu_{\mathrm{u}}^{\mathrm{GNIA}} = 1.495,$$

without reaching the prescribed maximum load. The curve shows an initially almost linear response, followed by a progressive reduction in tangent stiffness, manifested by increasing lateral displacements for modest load increments. Near the maximum value reached, the response tends towards a plateau, indicating attainment of the limit equilibrium configuration and the consequent inability to continue along the loading path.

The load multiplier obtained from the GNIA is therefore approximately $\mu_{\mathrm{u}}^{\mathrm{GNIA}} = 1.495$, providing a more realistic estimate of resistance than the corresponding multiplier obtained from the linear buckling analysis, $\mu_{\mathrm{cr},1}^{\mathrm{LUSAS,\,2girder}} \approx 1.590$, because it accounts for second-order effects and the evolution of the deformed configuration during loading. Figure 32 shows the variation of the von Mises equivalent stresses in the top flange of the main girder, evaluated at the midspan section in the most highly stressed region. The graph shows an almost linear increase in stress for low values of the load multiplier, as expected for the elastic response of the structure.

As the *Load Factor* increases, the rate of stress increase progressively decreases, while the lateral displacements continue to grow markedly. This behaviour is attributable to second-order effects, which cause a progressive reduction in the global stiffness of the structure and redistribution of the stress state as lateral-torsional buckling develops. Near the maximum value reached by the analysis, $\mu_{\mathrm{u}}^{\mathrm{GNIA}} = 1.495$, the equivalent stresses tend towards an almost constant value, while the displacements continue to increase. This behaviour confirms that the response limit is governed by loss of global structural stability rather than by attainment of the material resistance. At the ULS combination for the first construction stage (trends shown in Figs. 31 and 32), corresponding to a unit *Load Factor*, the von Mises equivalent stress in the most highly stressed region of the top flange is approximately $310\,\mathrm{MPa}$. This value is below the nominal yield strength of S355 steel; the final comparison must nevertheless be made with the characteristic value f_y relevant to the actual plate thickness and with the corresponding design strength $f_{yd} = f_y/\gamma_{M0} = 355\,\mathrm{MPa}$. The geometrically nonlinear analysis reaches the maximum value $\mu_{\mathrm{u}}^{\mathrm{GNIA}} = 1.495 > 1.00$, showing that, in the model considered, loss of equilibrium due to geometric effects occurs at a load level above the design level for the casting stage. The verification against geometric instability may therefore be considered satisfied for the configuration analysed. The maximum value reached by the GNIA cannot, however, be taken as the ultimate capacity of the structure because, for multiplier values greater than unity, the equivalent stresses reach and subsequently exceed the yield strength while the material is kept indefinitely elastic. Assessment of the ultimate capacity therefore requires a geometrically and materially

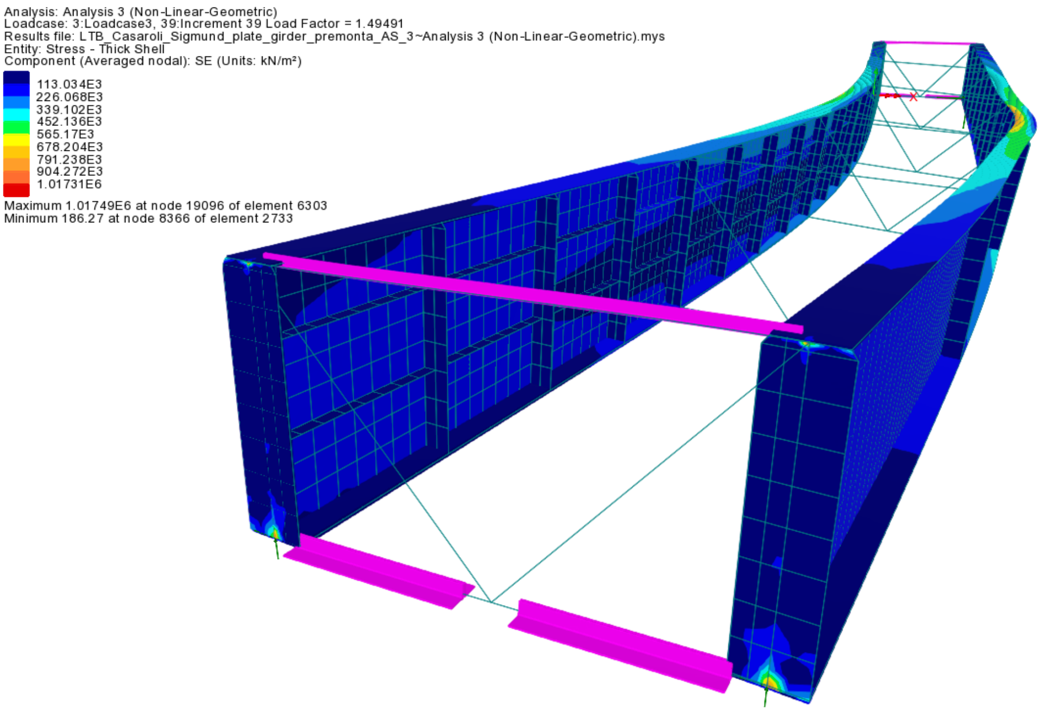

Figure 30. *Results of the geometrically nonlinear analysis with initial imperfection (GNIA), for $e_{LT} = 20\,\mathrm{mm}$ applied according to the first mode shape of the linear buckling analysis; $\mu_u^{\mathrm{GNIA}} = 1.495$. The steel material model was defined by a linear $\sigma - \varepsilon$ relationship.*

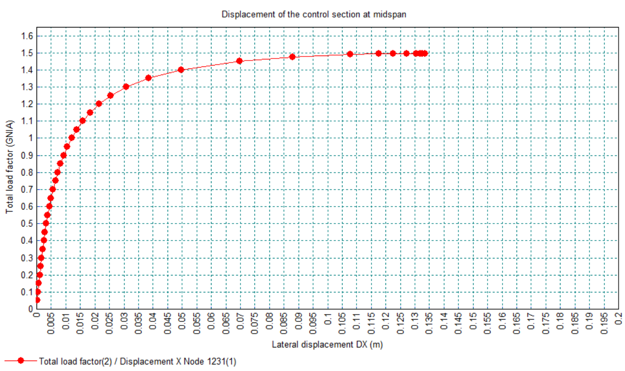

Figure 31. *Variation of the lateral displacement ΔY of the top flange at the control section with load multiplier in the GNIA. The steel is assumed perfectly elastic (material linearity).*

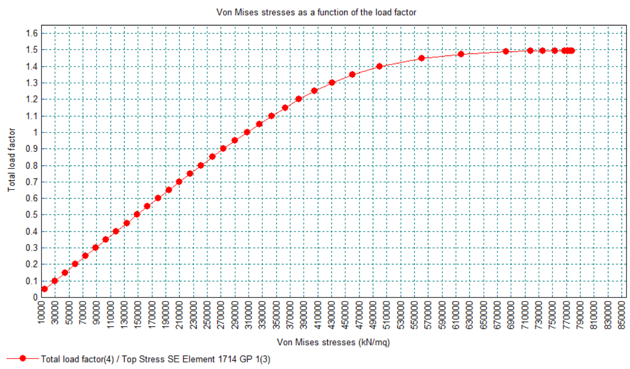

Figure 32. *Variation of the von Mises equivalent stresses in the top flange of the main girder, evaluated at the most highly stressed midspan section, with load multiplier in the GNIA.*

nonlinear analysis with initial imperfections (GMNIA).

13.6. Geometrically and materially nonlinear analysis

13.6.1. Preliminary remarks

To assess the resistance of the structure beyond the elastic range, a geometrically and materially nonlinear analysis (GMNIA) was subsequently carried out, in which second-order effects were combined with modelling of the elasto-plastic behaviour of steel. This approach allows the evolution of geometric deformation and member yielding to be described simultaneously, providing an estimate of structural resistance up to the ultimate state. For the main girders, a bilinear elasto-plastic constitutive model for S355 steel was adopted, characterised by the initial elastic modulus $E = 210000\,\mathrm{MPa}$, yield stress $f_y = 355\,\mathrm{MPa}$ and a negligible post-elastic tangent modulus ($E_t \simeq 0$), as illustrated in Fig. 33. The corresponding yield strain is:

$$\varepsilon_y = \frac{f_y}{E} \simeq 0.169\%.$$

13.6.2. Adopted plasticity model

Plastic behaviour was described using an isotropic plasticity model based on the von Mises yield criterion, commonly adopted for ductile structural steels. The combination of the von Mises criterion and the bilinear constitutive law allows the progressive spread of plastic strains through the members to be followed as the load increases, while retaining a numerically stable formulation in iterative GMNIA analyses (Fig. 34).

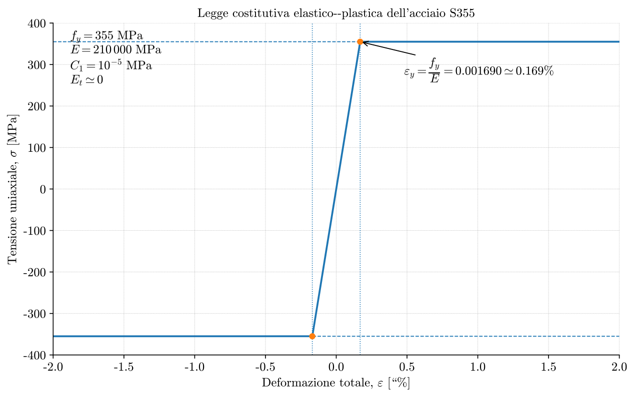

Figure 33. *Bilinear elasto-plastic constitutive law adopted for S355 steel in the GMNIA analyses.*

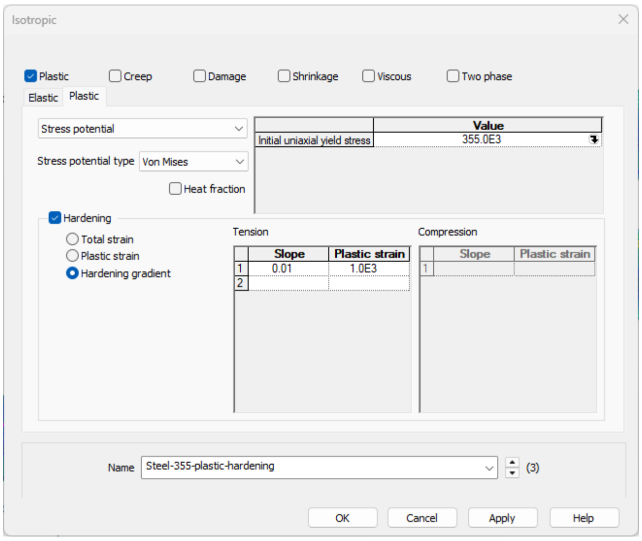

Figure 34. *LUSAS settings for the nonlinear properties of the plate steel. In addition to initial uniaxial yielding, a small hardening gradient is included to improve numerical stability and convergence.*

Steel hardening and stability of the numerical solution

A steel elasto-plastic constitutive law with modest post-elastic hardening was adopted in the GMNIA analyses (Figs. 33 and 34). This choice allows a limited increase in equivalent stress beyond the yield stress f_y to be represented and, at the same time, improves the regularity of the numerical solution during progressive yielding.
In an elastic–perfectly plastic model, the tangent modulus on the post-elastic branch is zero:

$$E_t = \frac{\mathrm{d}\sigma}{\mathrm{d}\varepsilon} = 0.$$

The resulting loss of tangent stiffness in an increasing portion of the structure may cause severe deterioration in the conditioning of the global tangent stiffness matrix:

$$\mathbf{K}_t\,\Delta\mathbf{u} = \Delta\mathbf{R}.$$

Near a limit point, or during development of an instability mechanism accompanied by yield-

continued...

ing, the matrix $\mathbf{K}_t$ may therefore become poorly conditioned or close to singular, making convergence of the equilibrium iterations more difficult.
Introducing a small post-elastic tangent modulus,

$$E_t > 0, \qquad E_t \ll E,$$

retains a modest incremental stiffness after yielding and promotes continuity of the equilibrium path, especially in the region near the maximum load and along the subsequent post-critical branch. Hardening does not eliminate structural instability, but reduces the numerical difficulties associated with the abrupt loss of material stiffness and facilitates the use of iterative procedures and *arc-length control*.[a]
In the presence of hardening, it is therefore normal for the von Mises equivalent stress shown in the result plots to exceed the initial yield stress locally:

$$\sigma_{\mathrm{vM}} > f_y.$$

These values do not necessarily represent an anomaly because the yield surface evolves according to the assigned constitutive law. Their interpretation must nevertheless be accompanied by examination of the equivalent plastic strains and the extent of the yielded zones, distinguishing a physically meaningful response from local peaks caused by stress concentrations, boundary conditions, nodal extrapolation or mesh dependence.

[a]Under arc-length control, LUSAS treats both the displacement increment and the load-multiplier increment as unknowns and introduces an additional constraint equation to limit progression along the equilibrium path. In the Crisfield formulation, this constraint is expressed by imposing a prescribed norm on the displacement increment; in the *relative displacement arc-length* procedure, control is related to the relative increment of a suitably selected displacement variable (see the settings in Fig. 28). According to the LUSAS theory manual, this strategy may be interpreted as a generalised form of displacement control and allows the equilibrium path to be followed near limit points and along post-critical branches in which the load factor does not increase monotonically. Selection of the correct path direction nevertheless remains sensitive to bifurcations, insufficient imperfections, numerical mechanisms or inadequate modelling; an incorrect root choice may appear as irregular load–displacement curves or closed paths. LUSAS also notes that any combination with *line search* procedures is implemented through an approximate iterative procedure intended to satisfy both the arc-length equation and the line-search equation.

13.6.3. *Interpretation of the geometrically and materially nonlinear analysis results*

The curves shown in Figs. 36 and 37 describe, respectively, the evolution of the lateral displacement of a control point on the top flange, at the section most affected by lateral sway, and the variation of the von Mises equivalent stress in the top flange immediately adjacent to the web in the same critical region.

Because the GMNIA was performed on the geometrically imperfect model, the response does not exhibit the sharp bifurcation characteristic of a linear buckling analysis of the perfect system. Instead, increasing load produces a progressive growth in lateral displacement and a continuous reduction in tangent stiffness until a limit point on the equilibrium path is reached.

The load-multiplier–lateral-displacement curve reaches an approximate maximum value of:

$$\mu_{\mathrm{u}}^{\mathrm{GMNIA}} \simeq 1.11.$$

At this value, the lateral displacement of the control point is of the order of:

$$u_{x,u} \simeq 0.06 \text{ m} = 60 \text{ mm}.$$

Beyond the limit point, the curve exhibits a descending branch: the lateral displacement continues to increase to values close to:

$$u_x \simeq 0.17 \text{ m},$$

while the load multiplier decreases to approximately:

$$\mu_{\mathrm{post}}^{\mathrm{GMNIA}} \simeq 1.05.$$

This behaviour indicates an unstable post-critical response, characterised by loss of lateral-torsional stiffness and decreasing load-carrying capacity as deformation increases. The maximum of the curve must therefore be interpreted as the resistance limit of the adopted GMNIA model, while points on the descending branch represent equilibrium configurations with substantially larger displacements and lower load-carrying capacity.

The von Mises equivalent stresses vary almost proportionally with the load multiplier during the initial and intermediate stages of the analysis. Near the maximum load, the stress at the monitored point reaches values of the order of:

$$\sigma_{\mathrm{vM}} \simeq (3.3 \div 3.6) \times 10^5 \text{ kN/m}^2 = 330 \div 360 \text{ MPa}.$$

This interval includes the yield stress adopted for S355 steel:

$$f_y = 355 \text{ MPa}.$$

The local attainment of stresses close to f_y at the limit point shows that the loss of load-carrying capacity cannot be attributed solely to elastic buckling. It results from the interaction between:

- amplification of displacements and rotations due to geometric nonlinearity;
- progressive reduction in the lateral-torsional stiffness of the system;
- onset of yielding in the most highly stressed regions of the top flange and adjacent web.

On the branch following the maximum, the equivalent stress remains close to the yield level, while the lateral displacement increases considerably and the load multiplier decreases. This trend is consistent with the development of local plastic strains and stress redistribution accompanied by the progression of global lateral sway. The substantial stabilisation of the local stress does not therefore imply stabilisation of the structural response; on the contrary, the system continues to deform with greatly reduced stiffness and decreasing load-carrying capacity.

The maximum value obtained from the GMNIA may be compared with the first elastic critical multiplier of the perfect LUSAS model:

$$\mu_{\mathrm{cr},1}^{\mathrm{LUSAS,\,2girder}} = 1.590.$$

The ratio of the nonlinear ultimate multiplier to the elastic critical multiplier is:

$$\frac{\mu_{\mathrm{u}}^{\mathrm{GMNIA}}}{\mu_{\mathrm{cr},1}^{\mathrm{LUSAS,\,2girder}}} \simeq \frac{1.11}{1.590} \simeq 0.70.$$

The capacity identified by the GMNIA is therefore approximately

$$\left(1 - \frac{1.11}{1.590}\right) \times 100 \simeq 30\%$$

lower than the critical value obtained from the linear buckling analysis of the geometrically perfect model.

Comparison with the value obtained using LTBeamN, assuming ideal torsional restraints at a spacing of $9.60\,\mathrm{m}$,

$$\mu_{\mathrm{cr}}^{\mathrm{LTBeamN},\,s_d=9.60\,\mathrm{m}} = 1.872,$$

instead gives:

$$\frac{\mu_{\mathrm{u}}^{\mathrm{GMNIA}}}{\mu_{\mathrm{cr}}^{\mathrm{LTBeamN},\,s_d=9.60\,\mathrm{m}}} \simeq \frac{1.11}{1.872} \simeq 0.59.$$

The GMNIA ultimate capacity is therefore approximately 41% lower than the critical multiplier of the single girder with ideal torsional restraints. This difference is consistent with the greater idealisation of the LTBeamN model, in which the intermediate restraints perfectly prevent torsional rotation, whereas the LUSAS model permits diaphragm deformation and development of a global twin-girder system mode.

The three values:

$$\mu_{\mathrm{cr}}^{\mathrm{LTBeamN},\,s_d=9.60\,\mathrm{m}} = 1.872, \qquad \mu_{\mathrm{cr},1}^{\mathrm{LUSAS,\,2girder}} = 1.590,$$

$$\mu_{\mathrm{u}}^{\mathrm{GMNIA}} \simeq 1.110,$$

must therefore not be interpreted as alternative results from the same analysis, but as successive levels of representation of the structural behaviour. The first refers to the single girder with ideal torsional restraints; the second describes elastic buckling of the perfect twin-girder system with deformable diaphragms; the third jointly includes the initial geometric imperfection, second-order effects and material yielding.

Overall, the results lead to the following conclusions:

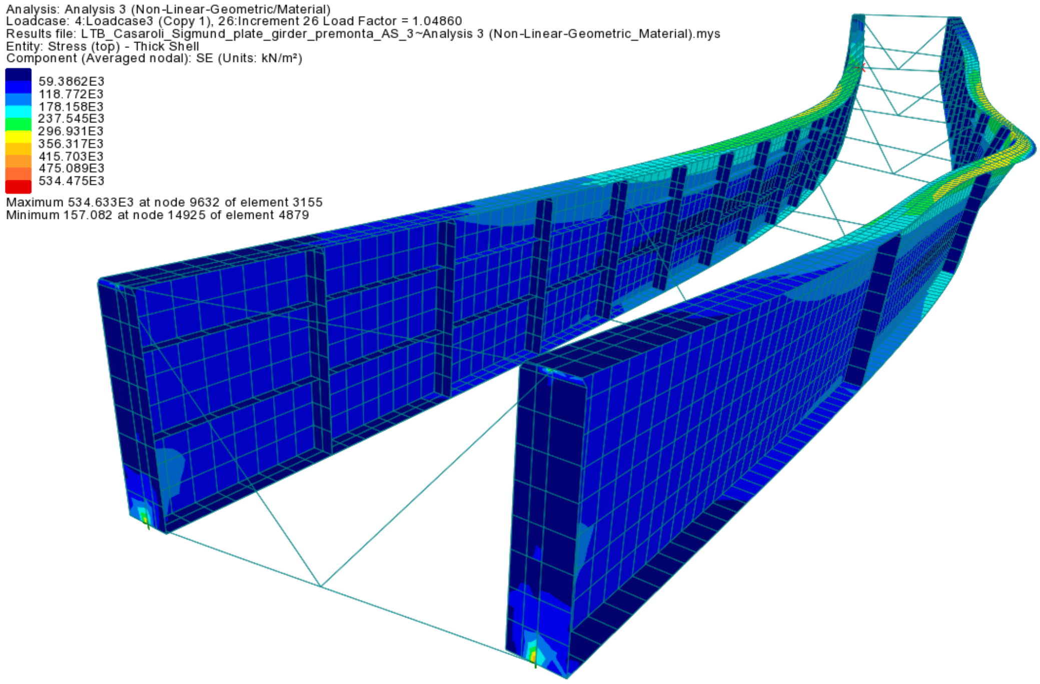

Figure 35. *Deformed shape of the two girders at the post-peak load multiplier* $\mu_{\rm post}^{\rm GMNIA} = 1.049$ *under geometric and material nonlinearity. The legend shows limited local peaks in equivalent stress, attributable to the extrapolation from integration points and nodal averaging (Averaged nodal) adopted by the LUSAS post-processor. As indicated in the software theory documentation [29], [28], in the presence of high stress gradients these values may be locally amplified without representing the global stress state of the structure.*

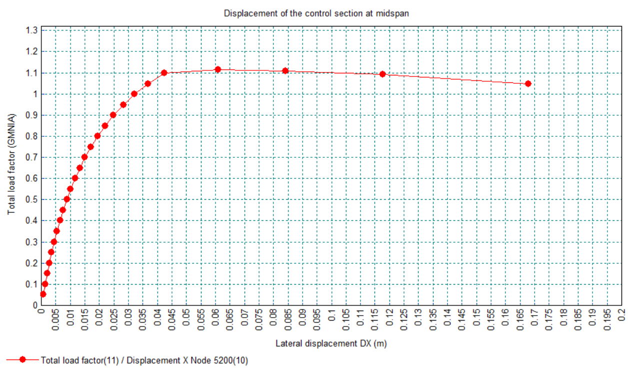

Figure 36. *Results from the geometrically and materially nonlinear analysis: displacement diagram for the central point of the top flange at the section of maximum lateral sway (*post-buckling behaviour on the *descending branch).*

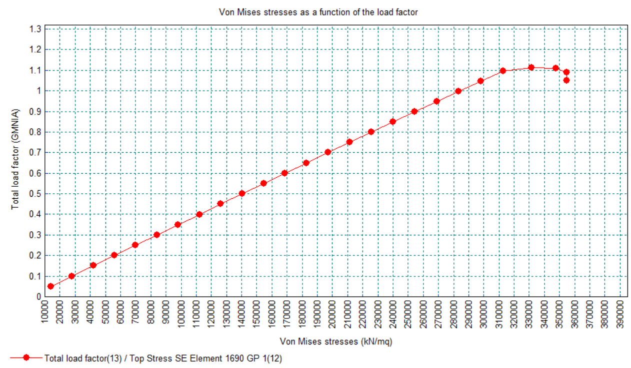

Figure 37. *Results from the geometrically and materially nonlinear analysis: variation of stresses in the flange plates and the welded portion of the web with load factor.*

- collapse is preceded by marked amplification of the lateral displacement of the compressed flange;
- the limit point is reached at a load multiplier close to $\mu_{\rm u}^{\rm GMNIA} \simeq 1.11$;
- local yielding occurs in the region of maximum lateral sway near the maximum load;
- the descending branch indicates an unstable post-critical response and decreasing load-carrying capacity;
- the ultimate resistance is governed by the interaction between global lateral-torsional buckling, geometric nonlinearity and local yielding;
- although the linear buckling analysis correctly identifies the shape and scale of the instability phenomenon, it overestimates the load level actually attainable by the imperfect and materially nonlinear system.

With reference to the ULS combination adopted as the reference load vector, corresponding to $\mu = 1.00$, the global GMNIA verification is formally satisfied because:

$$\mu_{\rm u}^{\rm GMNIA} \simeq 1.11 > 1.00.$$

The corresponding utilisation ratio may be expressed as:

$$\eta_{\rm GMNIA} = \frac{1}{\mu_{\rm u}^{\rm GMNIA}} \simeq \frac{1}{1.11} = 0.901 < 1.00.$$

The model capacity therefore exceeds the design load level by approximately 11%. The modelled twin-girder system may therefore be regarded as satisfying the verification, but with a limited resistance margin: the condition is close to the limit, although it does not coincide with it. This conclusion assumes that the unit load vector fully represents the design ULS combination and that the material properties used in the GMNIA are consistent with the adopted design values. Omitting the cross-ties removes their stabilising contribution from the model and is conservative in this specific respect; it does not, however, replace the additional local and connection verifications.

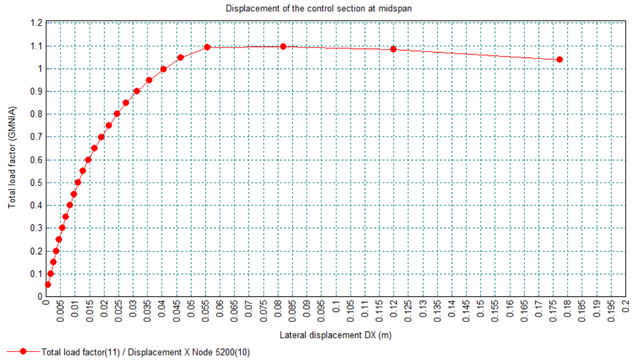

Figure 38. *GMNIA results for imperfections $e_{LT} = 25\,\mathrm{mm}$: displacement analysis of the central portion of the top flange at the section of maximum lateral sway.*

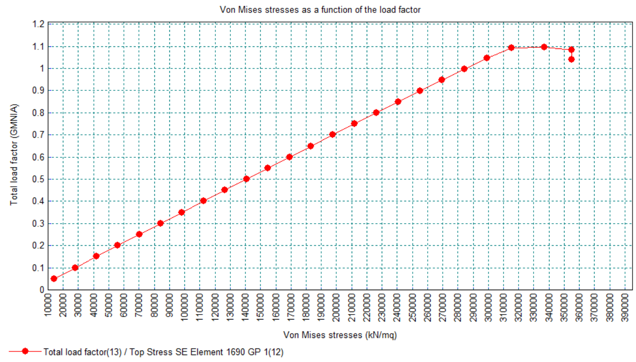

Figure 39. *GMNIA results for imperfections $e_{LT} = 25\,\mathrm{mm}$: von Mises stress analysis of the web plates and the central portion of the top flange at the section of maximum lateral sway.*

The stress curve refers to a specific integration point and must therefore be regarded as a local indicator of the onset of yielding, not as a measure of the overall extent of the plastic zones. Quantitative assessment of the spread of yielding requires examination of the equivalent stress and plastic strain contours over the entire compressed flange, web and connection regions adjacent to the diaphragms.

13.7. Selected comparisons for different prescribed imperfection amplitudes

The results of the geometrically and materially nonlinear analyses with initial imperfections (GMNIA), performed by varying the prescribed lateral-torsional imperfection amplitude, are reported below. In addition to the reference value $e_{LT} = 20\,\mathrm{mm}$, the following amplitudes were considered:

$$e_{LT} = 25\,\mathrm{mm}, \qquad e_{LT} = 30\,\mathrm{mm}, \qquad e_{LT} = 35\,\mathrm{mm}.$$

Repeating the analysis for different values of e_{LT} is not intended arbitrarily to identify a more adverse configuration, but to assess the sensitivity of the numerical response to one of the parameters having the greatest influence in stability analyses. In a GMNIA, the initial imperfection breaks the symmetry of the theoretically perfect configuration, activates the unstable kinematics from the outset and affects both the development of second-order effects and the progressive spread of yielding. Its shape, direction and amplitude may therefore influence the apparent initial stiffness, the slope of the load–displacement curve, the value of the ultimate multiplier and the extent of the post-critical branch.
The need to examine several amplitudes also arises from the very meaning assigned to imperfections in structural calculations. The actual geometry of a welded girder does not coincide with the nominal geometry of the ideal model, but inevitably includes deviations caused by fabrication and erection tolerances, welding-induced distortions, local variations in flange and web straightness, possible connection eccentricities and imperfect positioning of transverse members. These geometric defects are accompanied by structural imperfections, among which the residual stresses generated by welding thermal cycles, non-uniform cooling, straightening operations and the fabrication process more generally are particularly important.

EN 1993-1-1 requires equivalent imperfections representative of the effects of geometric and structural imperfections, explicitly including residual stresses and initial variations in straightness, to be considered in global analysis. For members susceptible to lateral-torsional buckling, Clause 5.3.4 of the same standard further requires the adopted imperfection to be consistent with the deformation associated with the buckling phenomenon under consideration. For structures formed from plate elements, Annex C of EN 1993-1-5, devoted to finite-element analyses, specifies that the imperfections introduced into the model must include both geometric and structural components; where the latter are not represented separately by an appropriate residual-stress field, equivalent geometric imperfections may be used to represent their combined effects [7, 8].

The imperfection used in the present study must therefore be interpreted as an *equivalent geometric imperfection*, not as an exact reproduction of a single measurable defect in the steelwork. Since an initial residual-stress field derived from the welding process was not introduced separately into the model, the amplitude assigned to the initial deformed shape also implicitly represents, in simplified form, the adverse effects that such stresses may have on stability and on the onset of yielding. The parametric variation of e_{LT} therefore makes it possible to verify whether the calculated capacity depends strongly on a single assumption or whether the result remains sufficiently stable over a plausible imperfection range.

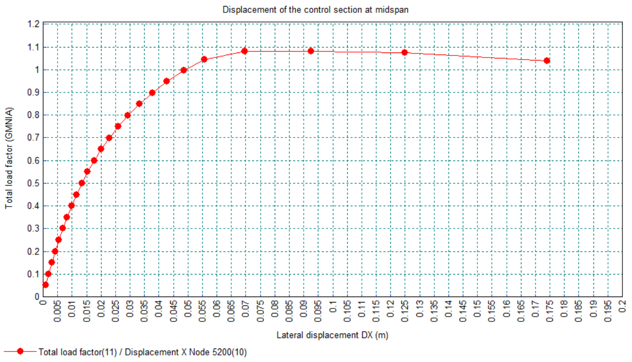

Figure 40. *GMNIA results for imperfections* $e_{LT} = 30\,\mathrm{mm}$*: displacement analysis of the central portion of the top flange at the section of maximum lateral sway.*

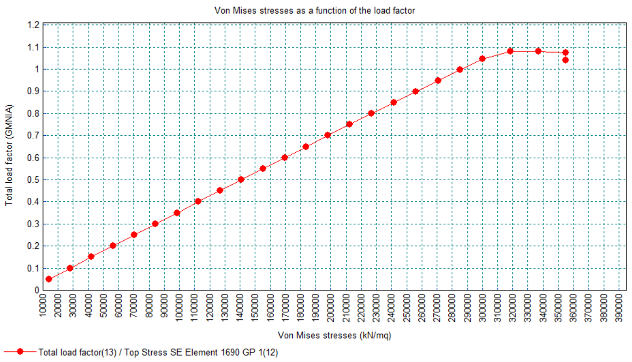

Figure 41. *GMNIA results for imperfections* $e_{LT} = 30\,\mathrm{mm}$*: von Mises stress analysis of the web plates and the central portion of the top flange at the section of maximum lateral sway.*

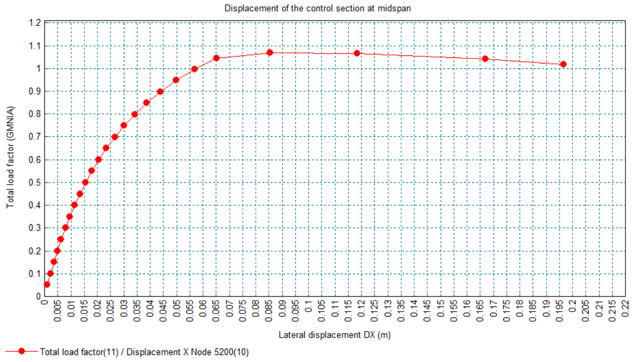

Figure 42. *GMNIA results for imperfections* $e_{LT} = 35\,\mathrm{mm}$*: displacement analysis of the central portion of the top flange at the section of maximum lateral sway.*

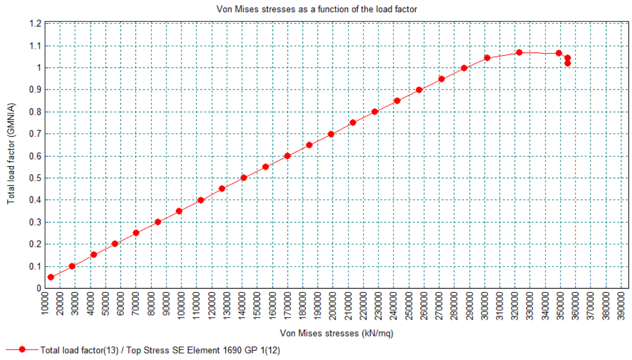

Figure 43. *GMNIA results for imperfections* $e_{LT} = 35\,\mathrm{mm}$*: von Mises stress analysis of the web plates and the central portion of the top flange at the section of maximum lateral sway.*

This approach is also consistent with the principles of design assisted by finite-element analysis. EN 1993-1-5 requires the imperfection direction to be selected so as to produce the lowest resistance and, where relevant, possible interactions between global and local imperfections to be considered. More recent formulations devoted to design by advanced numerical analysis also distinguish between geometric defects introduced with their physical amplitude and equivalent geometric imperfections, which are generally larger and incorporate the effects of residual stresses and other structural imperfections. Consequently, adopting a single value of e_{LT}, although formally defined, does not completely remove the uncertainty associated with the actual initial configuration; a parametric verification therefore provides a useful robustness check.

From a mechanical standpoint, increasing the initial imperfection amplitude progressively brings forward the onset of second-order effects. For the same load multiplier, the more highly deformed initial configuration develops greater lateral sway and, consequently, a more rapid increase in secondary actions associated with structural deformation. This effect does not necessarily imply an equally marked reduction in ultimate capacity, because the latter depends on the interaction between global deformability, stress distribution, development of plastic strains and the redistribution capacity of the system.

The results show that the four load–displacement curves retain a substantially similar shape. In all cases, an initial phase of progressively increasing lateral displacement, attainment of a limit point and a subsequent mildly descending branch can be identified. Thus, over the imperfection range analysed, there is no clear evidence of a change in the resistance mechanism; instead, a quantitative variation in the response is observed, characterised by increasing displacements and a moderate reduction in the ultimate multiplier.

The maximum values inferred from the curves are approximately:

$$\mu_\mathrm{u} \simeq \begin{cases} 1.11, & e_{LT} = 20\,\mathrm{mm}, \\ 1.10, & e_{LT} = 25\,\mathrm{mm}, \\ 1.08, & e_{LT} = 30\,\mathrm{mm}, \\ 1.07, & e_{LT} = 35\,\mathrm{mm}. \end{cases}$$

Increasing the imperfection from $20\,\mathrm{mm}$ to $35\,\mathrm{mm}$, i.e. by 75%, therefore reduces the ultimate multiplier by approximately $3 \div 4\%$. Sensitivity of the ultimate capacity to imperfection amplitude is thus present but relatively limited. In particular, comparison between $e_{LT} = 20\,\mathrm{mm}$ and $e_{LT} = 25\,\mathrm{mm}$ confirms that the two results are close but not identical: the second model exhibits a greater displacement at the design load level and a slightly lower maximum multiplier.

A more evident difference is observed when comparing lateral displacements at the design load level:

$$\mu = 1.00.$$

Approximate values obtained by interpolation of the numerical curves are:

$$D_X(\mu = 1.00) \simeq \begin{cases} 32\,\text{mm}, & e_{LT} = 20\,\text{mm}, \\ 40\,\text{mm}, & e_{LT} = 25\,\text{mm}, \\ 49\,\text{mm}, & e_{LT} = 30\,\text{mm}, \\ 56\,\text{mm}, & e_{LT} = 35\,\text{mm}. \end{cases}$$

Relative to the reference model, the increase in lateral displacement at the design load level is therefore approximately 25% for $e_{LT} = 25\,\text{mm}$, 53% for $e_{LT} = 30\,\text{mm}$ and 75% for $e_{LT} = 35\,\text{mm}$. The variation is nearly proportional to the increase in the prescribed imperfection, showing that the deformation response is substantially more dependent on e_{LT} than the ultimate capacity.

The comparison must refer to the total displacement returned for the imperfect configuration. Since the different analyses start from initial geometries characterised by different amplitudes, part of the lateral distance reached by the structure is directly attributable to the prescribed imperfection, while the remainder results from load-induced amplification. Therefore, in addition to the absolute value of D_X, it may be useful to consider the displacement increment relative to the initial configuration:

$$\Delta D_X = D_X - D_{X,0}.$$

This comparison makes it possible, at least in global terms, to distinguish the effect of the greater initial deformation from the actual nonlinear amplification developed during load application. The substantial regularity of the curves nevertheless indicates that increasing e_{LT} does not merely translate the configuration geometrically, but progressively modifies the system response through second-order effects.

A different trend is observed for the von Mises equivalent stresses considered in the same control region. At $\mu = 1.00$, the curves give approximate values of:

$$\sigma_{\text{vM}}(\mu = 1.00) \simeq \begin{cases} 280\,\text{MPa}, & e_{LT} = 20\,\text{mm}, \\ 281\,\text{MPa}, & e_{LT} = 25\,\text{mm}, \\ 282\,\text{MPa}, & e_{LT} = 30\,\text{mm}, \\ 284\,\text{MPa}, & e_{LT} = 35\,\text{mm}. \end{cases}$$

The overall increase between the extreme values is therefore of the order of $4\,\text{MPa}$, corresponding to approximately 1.5%. Within the accuracy permitted by reading the graphs, the stress state in the monitored region at the design level may therefore be regarded as only weakly sensitive to imperfection amplitude. The increase in e_{LT} is manifested mainly through the global kinematic response and only secondarily through increased stress at the selected control point.

As summarised in Table 10 and Fig. 44, increasing e_{LT} therefore produces two effects of differing intensity.

Table 10. *Approximate comparison of GMNIA results for varying lateral-torsional imperfection amplitude.*

e_{LT} mm	μ_u –	$D_X(\mu = 1.00)$ mm	$\sigma_{vM}(\mu = 1.00)$ MPa
20	$\simeq 1.11$	$\simeq 32$	$\simeq 280$
25	$\simeq 1.10$	$\simeq 40$	$\simeq 281$
30	$\simeq 1.08$	$\simeq 49$	$\simeq 282$
35	$\simeq 1.07$	$\simeq 56$	$\simeq 284$

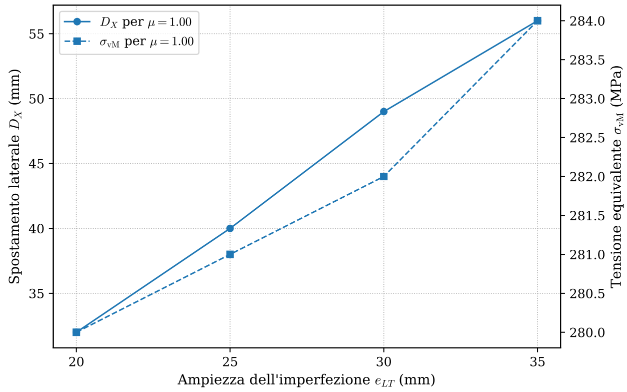

Figure 44. *Sensitivity of the GMNIA response to lateral-torsional imperfection amplitude: lateral displacement and von Mises equivalent stress at the load multiplier $\mu = 1.00$. The values were obtained by graphical interpolation of the numerical curves.*

The first, clearly recognisable, is the increase in lateral sway at the design level; the second is a progressive but modest reduction in the ultimate multiplier. By contrast, the equivalent stresses evaluated in the control region remain almost constant up to $\mu = 1.00$, indicating that, before the limit point is reached, the greater imperfection is accommodated mainly through a change in the deformed configuration.

The small variation in stress must not be interpreted as an absence of imperfection effects. The reported stresses refer to a specific integration point and a particular structural component; they do not necessarily describe the complete stress distribution or the extent of the yielded zones. A complete assessment therefore also requires comparison of the stress contours, equivalent plastic strains and distribution of second-order effects along the girders and diaphragms.

The limited reduction in μ_u, together with the persistence of similar load–displacement curves, suggests that, within the range $20 \div 35\,\text{mm}$, the ultimate capacity of the system is not highly sensitive to imperfection amplitude. The service or design-level response is nevertheless more sensitive in deformation terms. Consequently, the choice of e_{LT} may have a relatively modest effect on the resistance assessment, but a more significant effect on predicted displacements and interpretation of the pre-critical evolution.

The results also confirm that the value $e_{LT} = 20\,\text{mm}$, adopted in the principal verification, does not identify an isolated or numerically anomalous solution. Analyses with larger imperfections produce a regular and mechanically consistent family of responses, characterised by a gradual reduction in capacity and progressive increase in displacements. The reference value may therefore be regarded as stable with respect to moderate variations in the prescribed amplitude, while recognising that a model without an explicit residual-stress field cannot uniquely identify the equivalent imperfection most representative of the actual steelwork.

Finally, the parametric analyses are not intended to identify an “exact” value of the actual imperfection, which could be defined only from geometric surveys and specific information on the fabrication process. Instead, they delimit a response range, assess the robustness of the result adopted in the principal verification and separately identify the sensitivity of the ultimate capacity, deformation response and stress state. Within the analysed range, the quantity most affected by e_{LT} is the lateral displacement, whereas the ultimate multiplier and stresses at the design level vary much less.

The results obtained for the successive larger imperfection values also confirm the adequacy of the initial estimate of the characteristic length, taken as approximately $L_{b,\text{eff}} = 5.5\,\text{m}$ and therefore conservatively converted into the amplitude $e_{LT} = 20\,\text{mm}$. The larger imperfections considered in the study produce only a limited reduction in ultimate capacity and do not alter the identified resistance mechanism, showing that the initial choice does not lead to a significant overestimate of the structural response.

14. Conclusions

This work completes the programme begun in the first part of the research, which was devoted to defining a simplified procedure for estimating the lateral-torsional buckling resistance of steel bridge girders. The procedure was developed through statistical inference based on comparison with a large set of results obtained using the code formulation, with the objective of providing a direct tool for preliminary sizing and stability checks. It must not be interpreted as a substitute for the complete verification required by EN 1993, but as a complementary method useful for rapidly estimating resistance and providing an independent reference against which the results of subsequent numerical analyses may be compared.

The application developed in the final part of the study has shown that the lateral-torsional buckling problem of a twin-girder deck cannot be reduced to a single modelling level. The simplified procedure, the EN 1993 verification, the one-dimensional LTBeamN model and the three-dimensional finite-element model describe different mechanical idealisations and provide complementary information. Differences between their respective results must therefore not be regarded, in themselves, as contradictory, but as consequences of the different assumptions concerning restraint stiffness, transverse deck deformability, the possibility of developing global twin-girder system modes, and the presence of geometric and material nonlinearities.

The comparison between LTBeamN and LUSAS was particularly significant. With ideal torsional restraints at a spacing of $9.60\,\text{m}$ in LTBeamN, while keeping the geometry, cross-section, load distribution and end conditions unchanged, the first critical multiplier was:

$$\mu_{\text{cr}}^{\text{LTBeamN}} = 1.872.$$

In the LUSAS twin-girder model, in which the diaphragms have finite stiffness and the cross-bracing was not represented, the corresponding value was:

$$\mu_{\text{cr}}^{\text{LUSAS}} = 1.590.$$

The reduction in critical multiplier relative to the ideal-restraint model is therefore approximately 15%. This result confirms that diaphragm spacing is a significant geometric scale for the buckling phenomenon, while also showing that actual diaphragms cannot automatically be treated as perfectly rigid torsional restraints. The critical mode of the three-dimensional system involves both girders and the transverse connections, allowing global deformations that cannot be reproduced by the idealised single-girder model.

The nonlinear analyses further highlighted the decisive role of geometric imperfections, second-order effects and local yielding. The GMNIA gave an ultimate multiplier of approximately:

$$\mu_{\text{u}}^{\text{GMNIA}} \simeq 1.11.$$

The modelled system therefore satisfies the verification for the adopted design combination because:

$$\mu_{\text{u}}^{\text{GMNIA}} > 1.00.$$

Expressed as a utilisation ratio, the verification gives:

$$\eta_{\text{GMNIA}} = \frac{1}{\mu_{\text{u}}^{\text{GMNIA}}} \simeq 0.90.$$

The resistance therefore exceeds the design load level, but with a limited margin. The system may be regarded as verified close to the resistance limit, because the maximum point on the load–displacement curve is associated with marked amplification of lateral sway and attainment of equivalent stresses close to yielding in the most highly stressed region of the top flange and adjacent web. The subsequent appearance of a descending branch confirms that the loss of capacity is governed by the interaction between global lateral-torsional buckling, geometric nonlinearity and local yielding. This result must nevertheless be interpreted in light of the fact that the FEM model did not include the cross-bracing arranged in the top- and bottom-flange planes. In the actual configuration, this bracing divides each $9.60\,\text{m}$ interval between consecutive diaphragms into two fields of length $4.80\,\text{m}$. Its omission reduces the lateral and torsional stiffness of the modelled system and permits larger global deformations than would presumably be compatible with the complete structural configuration.

Adopting cross-bracing diagonals in the top- and bottom-flange planes may therefore increase the effectiveness of the restraint system, limit lateral-torsional

Analysis method	Load multiplier
Linear eigenvalue buckling analysis (LBA)	1.590
Geometrically nonlinear analysis with imperfections (GNIA)	1.495
Geometrically and materially nonlinear analysis (GMNIA)	$\simeq 1.110$

Table 11. *Summary of results obtained using the different levels of numerical analysis.*

deformation and increase the ultimate capacity of the deck. Under this assumption, the value:

$$\mu_{\mathrm{u}}^{\mathrm{GMNIA}} \simeq 1.11$$

obtained from the model without diagonals may reasonably be interpreted as a conservative lower-bound estimate of the capacity of the actual braced configuration. This conclusion must not, however, be understood as an automatic quantification of the resistance increase produced by the bracing. Its actual stabilising effectiveness depends on the axial stiffness of the diagonals, connection deformability, construction clearances, the ability to transfer actions at the nodes and any tension-only behaviour of the crossed members. Quantitative assessment would therefore require explicit modelling of the bracing and its connections.

A general result of particular importance concerns the difficulty of identifying, using a single finite-element software package, the most plausible equilibrium configuration representative of actual behaviour. Buckling problems involving three-dimensional structures may exhibit local, distortional and global modes with closely spaced eigenvalues. The first mode returned numerically is not necessarily the most relevant for design, nor can the eigenvalue be interpreted separately from the corresponding deformation kinematics. Selection of the significant mode therefore requires examination of the mode shape, half-wave distribution, boundary conditions, connection deformability and actual structural arrangement.

Model complexity alone does not guarantee greater reliability of the result. As the number of elements, degrees of freedom and introduced nonlinearities increases, so too does the number of possible equilibrium configurations and sources of uncertainty. The conclusions may depend on discretisation, assigned restraint properties, the shape and amplitude of the initial imperfections, the material constitutive law, the incremental strategy and the numerical convergence criteria. For this reason, FEM analysis must always be accompanied by independent checks and mechanical interpretation of the results.

The practical significance of the work therefore lies in organising a verification process comprising successive and mutually comparable levels. The simplified procedure permits direct preliminary assessment; the EN 1993 formulation provides the code reference for the individual member; LTBeamN allows the elastic behaviour of the girder under specified restraint conditions to be checked; and LUSAS allows the three-dimensional system, diaphragm deformability and the combined effects of geometric and material nonlinearities to be analysed.

The combined use of these tools reduces the risk of attributing general validity to the result of a single model and makes the physical meaning of the observed differences clearer. From this perspective, the procedure proposed in the first part of the article also serves as an independent check on the numerical model: not only as a simplified calculation method, but also as a useful reference for identifying anomalous results, excessively rigid assumptions or poorly representative modal configurations. The final comparison between the different analysis levels must account for the different mechanical meaning of the resulting multipliers. Linear eigenvalue buckling analysis identifies the factor at which the ideal system loses elastic stability and the corresponding mode shape; however, it does not consider initial imperfections, progressive modification of the structural configuration or material yielding. The associated critical multiplier therefore generally provides an upper estimate of the capacity of the actual system.

By contrast, the geometrically nonlinear analysis of the imperfect configuration allows the complete evolution of displacements and second-order effects to be followed. It does not directly return a critical eigenvalue, but allows attainment of the limit condition to be recognised by examining the equilibrium path, the load–displacement curve and amplification of lateral-torsional deformation. Since the material remains linear elastic in this analysis, the stresses may formally exceed the yield strength without corresponding plastic redistribution.

GMNIA represents the most complete level of analysis among those considered, because it combines initial imperfections, geometric nonlinearity and material nonlinearity. Separate comparison of the different formulations nevertheless remains essential, because it identifies which phenomenon has the greatest influence on the structural response. In the case examined, moving from eigenvalue analysis to GNIA reduces the multiplier from 1.590 to 1.495, i.e. by approximately 6%; whereas introducing material nonlinearity leads to an ultimate value of approximately 1.11, with a further reduction of nearly 26%. Although the effects cannot be rigorously separated because of their interaction, these results indicate that, for the configuration analysed, local yielding has a more pronounced influence than geometric effects alone. The summary in Table 11 therefore shows that eigenvalue analysis is indispensable for identifying the buckling mode and providing an initial reference for elastic capacity, but cannot be used alone as a measure of ultimate resistance. GNIA assesses the influence of imperfections and second-order effects, while GMNIA also describes the progressive loss of stiffness associated with yielding and follows the equilibrium path up to the limit point and along the subsequent post-critical branch. In accordance with the approach adopted in the LUSAS technical documentation, carrying out the three analyses separately therefore does not duplicate the calculation, but provides a diagnostic tool for understanding the source of the capacity reduction and checking the mechanical consistency of the numerical solution.

✓ *Observations*

The GMNIA analyses indicate that, for the modelled configuration and the adopted construction-load combination, the two steel girders formally satisfy the Ultimate Limit State verification, since an ultimate multiplier greater than unity is obtained in every case ($\mu_u > 1.00$). This conclusion refers exclusively to the numerical model developed and to the assumptions adopted for loads, restraints, material properties and equivalent geometric imperfections introduced in the analysis. The verification therefore concerns the global stability and resistance of the twin-girder system during the construction stage considered and does not replace any required local verifications of individual construction details, such as connections, diaphragms, stiffeners, bearings, welds or local phenomena not explicitly represented in the finite-element model.

It should also be emphasised that the numerical model does not include the cross-bracing arranged in the top- and bottom-flange planes. Its presence in the actual configuration may reasonably be expected to increase the lateral and torsional stiffness of the deck and, consequently, its overall resistance to lateral-torsional buckling. The results may therefore be interpreted as conservative relative to the behaviour of the complete structure, although the benefit provided by the bracing cannot be quantified directly without modelling it explicitly.

In conclusion, lateral-torsional buckling of steel bridge decks must be treated as a problem in which resistance depends not solely on the properties of the individual cross-section, but on the interaction between global geometry, bracing systems, diaphragm stiffness, imperfections, yielding and actual boundary conditions. No single model can represent the entire phenomenon without uncertainty. The reliability of the assessment therefore derives from critical comparison of independent methods, consistency of the adopted assumptions and the designerś ability to relate the numerical result to the actual mechanical behaviour of the structure.

15. Traceability of the REV3 statistical campaign

The statistical campaign is reproducible using the Python scripts, intermediate data and audit records included in the supplementary package. The final version is identified as:
`REV3_FIXED_THIRDS_A09_gammaM1_1.10_M3_DOMAIN`.
The population comprises 9888 accepted cross-sections, 61 values of L_b and three static identifiers equivalent for the purposes of the coefficient rule, giving a total of 1809504 statistical records and 603168 independent physical combinations.

The final training/test split is grouped using the field `split_group_id`, defined at `geometry_id` level; no geometry therefore appears in both subsets. The compact model is verified row by row, while the dimensionless design charts are checked by propagation over the complete population of physical combinations. No underestimations relative to the exact formulation, no cases with $\rho < 1.000$, and no exceedances of the pointwise limits 1.150 in the frequent domain and 1.2075 in the boundary domain were found. Coefficients, predictions, summaries, monotonicity checks and file checksums are retained in the release package.

The supplementary material also includes the mechanical and EC3 populations, the shared core of the compact formula, the operational evaluator, vector PDF plots, PNG copies and the numerical CSV sources of the figures. The graphical representations are generated directly from the final results and contain no manual corrections or undocumented *smoothing*.

Acknowledgements

The authors gratefully acknowledge the entire team at *GPI Ingegneria s.r.l.*, Viale Tiziano 3, 00196 Rome, Italy, https://www.gpingegneria.com/, and in particular Eng. Claudio Zifferero, BIM Manager, for his interest in the initiative, his constructive discussions on digital modelling, and his support for the research and technical investigations undertaken within their shared professional environment. The authors also extend their sincere thanks to Mr Ugo Frigerio, the company's IT Manager, for his valuable assistance in setting up, managing and ensuring the operational continuity of the computing resources required for the numerical analyses and associated data management.

The authors also thank Eng. Carlo Margheriti, Partner and CEO of *Alhambra s.r.l.*, and Eng. Angelo Salcuni of *Alhambra s.r.l.*, Viale Bramante 41, 05100 Terni, Italy, https://www.alhambraingegneria.it/, for their specialist technical advice on the use of LUSAS, their willingness to discuss modelling strategies and the interpretation of results, and the generous provision of the licences used to develop the numerical analyses presented in this study. Their contribution enabled the practical aspects of the software to be investigated with greater confidence and the numerical checks to be performed using tools appropriate to the aims of the research.

The authors gratefully acknowledge Suzanne Martin (Academic Account Manager at LUSAS) and Finite Element Analysis Ltd. (FEA) for providing the LUSAS Academic licence used in this research.

The finite-element simulations in this study were performed using LUSAS Academic (Version 23.0, Finite Element Analysis Ltd., Kingston upon Thames, UK).

Conflict of interest

The authors declare that they have no financial, commercial, professional or personal conflicts of interest that could influence the content or conclusions of this study.

Links to shared software and supporting material

The authors are pleased to make available several tools developed in support of the theoretical framework adopted in this study for the assessment of lateral–torsional buckling during the construction stage in accordance with EN 1993. These comprise a spreadsheet for the verification of welded monosymmetric sections, with or without longitudinal stiffeners arranged symmetrically about the web, and a spreadsheet for the verification of rolled sections selected from a database of commercially available profiles, with the option of including longitudinal stiffeners. The spreadsheets automatically determine the section properties and classification, including the effective properties of Class 4 sections, the elastic critical moment M_{cr}, the non-dimensional slenderness $\overline{\lambda}_{LT}$, the reduction factor χ_{LT} and the design buckling resistance $M_{b,Rd}$, accounting for restraint conditions, the bending-moment diagram, warping, the height of load application and monosymmetry.

In both Excel workbooks, the torsional and warping properties are determined using the formulae adopted for welded monosymmetric sections, consistent with the mechanical model used for verification in accordance with EN 1993. This includes the automatic calculation of the Saint-Venant torsion constant I_t, the position of the shear centre and the monosymmetry parameter z_j, which are employed in evaluating the elastic critical moment and assessing lateral–torsional buckling.

The standalone application:

```
LTB_simplified_design_app.exe
```

is also provided. It performs the complete verification in accordance with EN 1993 for cross-sections of Classes 1, 2, 3 and 4. For Class 4 sections, with or without longitudinal stiffeners, it determines the effective section properties in accordance with EN 1993-1-5. By contrast, the statistical parametric procedure provides results only for configurations falling within its calibration domain, which comprises welded steel–concrete composite bridge decks with two or three main girders. Other geometries are addressed exclusively through the general EN 1993 verification module.

Note. No registration is required to download the material from the following link:

http://www.sigmundcarlo.net/public/shared_CAB.zip

References

[1] Access Steel. SN003b-EN-EU: NCCI: Elastic critical moment for lateral torsional buckling. Technical Report SN003b-EN-EU, Access Steel, 2005. Non-Contradictory Complementary Information for EN 1993.

[2] ANAS S.p.A. Pedemontana di Palermo – Relazione di progetto dell'opera, Dibattito pubblico. https://dibattitopubblico.stradeanas.it/wp-content/uploads/2024/02/Pedemontana_di_Palermo_Relazione_DP.pdf, 2024. Relazione tecnica online.

[3] Friedrich Bleich. *Buckling Strength of Metal Structures*. McGraw-Hill, New York, 1952.

[4] California Department of Transportation. *Bridge Design Practices, Chapter 62: Steel Plate Girders*. California Department of Transportation, 2022.

[5] CEN. EN 1990: Eurocode – Basis of structural design, 2002. European standard.

[6] CEN. EN 1991-1-6: Eurocode 1 – Actions on structures – Part 1-6: General actions – Actions during execution, 2005. European standard.

[7] CEN. EN 1993-1-1: Eurocode 3: Design of steel structures – Part 1-1: General rules and rules for buildings. Technical report, European Committee for Standardization, Brussels, 2005. Including subsequent amendments and corrigenda where applicable.

[8] CEN. EN 1993-1-5: Eurocode 3: Design of steel structures – Part 1-5: Plated structural elements. Technical report, European Committee for Standardization, Brussels, 2006. Including subsequent amendments and corrigenda where applicable.

[9] CEN. EN 1993-2: Eurocode 3: Design of steel structures – Part 2: Steel bridges. Technical report, European Committee for Standardization, Brussels, 2006. Including subsequent amendments and corrigenda where applicable.

[10] CEN. EN 1993-1-1:2022, Eurocode 3: Design of steel structures – Part 1-1: General rules and rules for buildings, 2022. Second generation Eurocode 3; verify national adoption before design use.

[11] CEN. EN 1993-2:2026, Eurocode 3 – Design of steel structures – Part 2: Steel bridges, 2026. European standard.

[12] Wai-Fah Chen and Eric M. Lui. *Structural Stability: Theory and Implementation*. Elsevier, New York, 1987.

[13] CNR-UNI. *CNR-UNI 10011: Costruzioni di acciaio. Istruzioni per il calcolo, l'esecuzione, il collaudo e la manutenzione*. Consiglio Nazionale delle Ricerche – Ente Nazionale Italiano di Unificazione, Roma, 1988. Giugno 1988, par. 7.3.2.2.1, stabilità laterale delle travi inflesse.

[14] COMBRI Project. Competitive Steel and Composite Bridges by Improved Steel Plated Structures – Design Manual. Design manual, COMBRI Project.

[15] Consiglio Superiore dei Lavori Pubblici. Circolare 21 gennaio 2019, n. 7 C.S.LL.PP.: Istruzioni per l'applicazione dell'Aggiornamento delle Norme tecniche per le costruzioni di cui al D.M. 17 gennaio 2018, 2019. Gazzetta Ufficiale della Repubblica Italiana, Serie Generale, n. 35 del 11 febbraio 2019.

[16] Fabrizio De Miranda. *Ponti a struttura d'acciaio*, volume VII of *Collana tecnico-scientifica per la progettazione di strutture in acciaio*. Italsider, Genova, 1971. Riferimento utilizzato per i criteri di proporzionamento preliminare delle travi composte acciaio-calcestruzzo.

[17] László Dunai, Balázs Kövesdi, Leroy Gardner, Mohammad Al-Emrani, Miquel Casafont, Hervé Degée, Michal Jandera, Ulrike Kuhlmann, Andreas Taras, and Francis Walport. Design assisted by finite element analysis – Introduction to prEN 1993-1-14 and Technical Report. *ce/papers*, 6(3–4):2677–2682, 2023.

[18] European Convention for Constructional Steelwork. *Manual on Stability of Steel Structures*. European Convention for Constructional Steelwork, Brussels, 2 edition, 1976.

[19] Finite Element Analysis Ltd. Buckling analyses. LUSAS Customer Support Note CSN/LUSAS/1019, Finite Element Analysis Ltd., Kingston upon Thames, Surrey, United Kingdom, 2025. Guideline document on linear eigenvalue buckling, geometrically nonlinear analysis and geometrically and materially nonlinear analysis.

[20] Fondazione Promozione Acciaio. Ponte sulla Dora Riparia – Collegno (TO). https://www.promozioneacciaio.it/UserFiles/File/pdf/pubblicazioni/Ponte%20sulla%20Dora%20Riparia%20-%20Collegno.pdf. Scheda tecnica online.

[21] Fondazione Promozione Acciaio. Soluzioni di impalcato per ponti in acciaio. https://www.promozioneacciaio.it/UserFiles/File/pdf/pubblicazioni/Impalcati%20ponti%20in%20acciaio_WEB.pdf. Documento tecnico online.

[22] Fondazione Promozione Acciaio. Viadotti in acciaio – lavori di ammodernamento e sistemazione della SS 117 Centrale Sicula. https://www.promozioneacciaio.it/UserFiles/File/pdf/pubblicazioni/Viadotti%20in%20acciaio%20-

%20lavori%20di%20ammodernamento%20e%20sistemazione%20della%20SS%20117%20Centrale%20Sicula.pdf. Scheda tecnica online.

[23] Fondazione Promozione Acciaio. Viadotto del Ranco – Quadrilatero Marche-Umbria. https://www.promozioneacciaio.it/UserFiles/File/pdf/pubblicazioni/WEB_Viadotto%20del%20Ranco%20-%20Quadrilatero%20Umbria-Marche.pdf. Scheda tecnica online.

[24] Theodore V. Galambos and Andrea E. Surovek. *Structural Stability of Steel: Concepts and Applications for Structural Engineers*. John Wiley and Sons, Hoboken, New Jersey, 1 edition, 2008.

[25] Şt. I. Guţiu, Gabriela Pau, I. Chindriş, and C. Moga. A Comparative Analysis of the Lateral-Torsional Buckling Resistance of the Hot-Rolled and Welded Sections. *Journal of Applied Engineering Sciences*, 16(29):27–32, 2026. Available online: 31 May 2026.

[26] D. C. Iles. Determining the buckling resistance of steel and composite bridge structures. SCI Publication ED008, The Steel Construction Institute, Ascot, 2012.

[27] P. A. Kirby and D. A. Nethercot. *Design for Structural Stability*. Granada Publishing, London, 1979.

[28] LUSAS. *LUSAS FAQ: Why are Some Stress Results Greater than the Yield Stress?*, 2025. Accessed July 2026.

[29] LUSAS. *LUSAS Theoretical Note: Finite Element Equilibrium*, 2025. Accessed July 2026.

[30] LUSAS. *Theory Manual, Volume 1*. LUSAS, Kingston upon Thames, Surrey, United Kingdom, version 23.0, issue 1 edition, 2025.

[31] LUSAS. *Theory Manual, Volume 2*. LUSAS, Forge House, 66 High Street, Kingston upon Thames, Surrey, KT1 1HN, United Kingdom, LUSAS Version 23.0, Issue 1 edition, 2025. Theory Manual, Volume 2.

[32] LUSAS. *Buckling Analysis of a Plate Girder*. LUSAS, For LUSAS version 23.0 edition, n.d. Worked example. Software product: Any Plus version. Product option: None.

[33] William McGuire, Richard H. Gallagher, and Ronald D. Ziemian. *Matrix Structural Analysis*. John Wiley and Sons, New York, 2 edition, 2000.

[34] Ministero delle Infrastrutture e dei Trasporti. D.M. 17 gennaio 2018: Aggiornamento delle Norme tecniche per le costruzioni, 2018. Gazzetta Ufficiale della Repubblica Italiana, Serie Generale, n. 42 del 20 febbraio 2018.

[35] Charles G. Salmon, John E. Johnson, and Faris A. Malhas. *Steel Structures: Design and Behavior*. Pearson Prentice Hall, Upper Saddle River, New Jersey, 5 edition, 2009.

[36] Carlo Sigmund. *Progettazione e calcolo di elementi e connessioni in acciaio. Secondo Eurocodici strutturali CEN/TC 250 in accordo con le NTC 2018 e relativa Circolare*. Dario Flaccovio Editore, Palermo, 2020.

[37] George J. Simitses and Dewey H. Hodges. *Fundamentals of Structural Stability*. Butterworth-Heinemann, Burlington, Massachusetts, 2006.

[38] H. H. Snijder, R. P. van der Aa, H. Hofmeyer, and B. W. E. M. van Hove. Lateral torsional buckling design imperfections for use in non-linear FEA. *Steel Construction*, 11(1):49–56, 2018.

[39] Richard Stroetmann and Sergei Fominow. Equivalent geometric imperfections for the LTB-design of members with I-sections. *Steel Construction*, 15(4):213–228, 2022.

[40] Stephen P. Timoshenko and James M. Gere. *Theory of Elastic Stability*. McGraw-Hill, New York, 2 edition, 1961.

[41] Nicholas S. Trahair. *Flexural-Torsional Buckling of Structures*. E. and F. N. Spon, London, 1993.

[42] Nicholas S. Trahair, Mark A. Bradford, David A. Nethercot, and Leroy Gardner. *The Behaviour and Design of Steel Structures to EC3*. Taylor and Francis, London, 4 edition, 2008.

[43] UNI. UNI EN 1993-1-1:2022, Eurocodice 3 – Progettazione delle strutture di acciaio – Parte 1-1: Regole generali e regole per gli edifici, 2022. Norma tecnica.

[44] UNI. UNI EN 1991-2:2024, Eurocodice 1 – Azioni sulle strutture – Parte 2: Carichi da traffico sui ponti e su altre opere di ingegneria civile, 2024. Norma tecnica.

[45] UNI. UNI EN 1993-1-5:2024, Eurocodice 3 – Progetto di strutture di acciaio – Parte 1-5: Elementi strutturali a lastra, 2024. Norma tecnica.

[46] UNI. UNI EN 1993-1-8:2024, Eurocodice 3 – Progettazione delle strutture di acciaio – Parte 1-8: Progettazione dei collegamenti, 2024. Norma tecnica.

[47] UNI. UNI EN 1990-1:2026, Eurocodice – Basi della progettazione strutturale e geotecnica – Parte 1: Nuove strutture, 2026. Norma tecnica.

[48] UNI. UNI EN 1991-1-6:2026, Eurocodice 1 – Azioni sulle strutture – Parte 1-6: Azioni durante l'esecuzione, 2026. Norma tecnica.

[49] UNI. UNI EN 1994-1-1:2026, Eurocodice 4 – Progettazione delle strutture composte acciaio-calcestruzzo – Parte 1-1: Regole generali e regole per gli edifici, 2026. Norma tecnica.

[50] UNI. UNI EN 1994-2:2026, Eurocodice 4 – Progettazione delle strutture composte acciaio-calcestruzzo – Parte 2: Regole generali e regole per i ponti, 2026. Norma tecnica.

[51] Vasilii Z. Vlasov. *Thin-Walled Elastic Beams*. Israel Program for Scientific Translations, Jerusalem, 1961. English translation from the Russian original.

[52] Ronald D. Ziemian, editor. *Guide to Stability Design Criteria for Metal Structures*. John Wiley and Sons, Hoboken, New Jersey, 6 edition, 2010.